

The role of three-nucleon potentials within the shell model: past and present

L. Coraggio,^{1,2} G. De Gregorio,^{1,2} T. Fukui,³
A. Gargano,² Y. Z. Ma,⁴ Z. H. Cheng,⁵ F. R. Xu,⁵

¹Dipartimento di Matematica e Fisica, Università degli Studi della Campania
“Luigi Vanvitelli”, viale Abramo Lincoln 5-I-81100 Caserta, Italy

²Istituto Nazionale di Fisica Nucleare, Complesso Universitario di Monte
S. Angelo, Via Cintia, I-80126 Napoli, Italy

³Faculty of Arts and Science, Kyushu University, Fukuoka 819-0395, Japan

⁴Guangdong Provincial Key Laboratory of Nuclear Science,
Institute of Quantum Matter, South China Normal University,
Guangzhou 510006, China

⁵School of Physics and State Key Laboratory of Nuclear Physics and Technology,
Peking University, Beijing 100871, China

September 6, 2023

Abstract

We survey the impact of nuclear three-body forces on structure properties of nuclei within the shell model. It has long been acknowledged, since the seminal works of Zuker and coworkers, that three-body forces play a fundamental role in making the monopole component of shell-model Hamiltonians, derived from realistic nucleon-nucleon potentials, able to reproduce the observed evolution of the shell structure. In the vast majority of calculations, however, their effects have been taken into account by shell-model practitioners by introducing *ad hoc* modifications of the monopole matrix elements. During last twenty years, a new theoretical approach, framed within the chiral perturbation theory, has progressed in developing nuclear potentials, where two- and many-body components are naturally and consistently built in. This new class of nuclear forces allows to carry out nuclear structure studies that are improving our ability to understand nuclear phenomena in a microscopic approach. We provide in this work an update on the status of the nuclear shell model based on realistic Hamiltonians that are derived from two- and three-nucleon chiral potentials, focusing on the role of the three-body component to provide the observed shell evolution and closure properties, as well as the location of driplines. To this end, we present the results of shell-model calculations and their comparison with recent experimental measurements, which enlighten the relevance of the inclusion of three-nucleon forces to master our knowledge of the physics of atomic nuclei.

Contents

1	Introduction	2
2	Three-body forces	6
2.1	<i>Backgrounds</i>	6
2.2	<i>Chiral effective field theory for three-nucleon forces</i>	8
3	Shell model	9
3.1	<i>Generalities</i>	9
3.2	<i>The derivation of realistic effective interactions and operators</i>	13
3.2.1	<i>The perturbative expansion of effective shell-model Hamiltonian</i>	15
3.2.2	<i>The perturbative expansion of effective shell-model decay operators</i>	21
3.3	<i>Gamow shell model with three-body forces</i>	23
4	Applications and comparison with experiment	25
4.1	<i>Benchmark calculations in the 0p-shell region</i>	25
4.2	<i>Approaching the weakly bound systems</i>	32
4.2.1	<i>The limit of oxygen isotopes</i>	32
4.2.2	<i>3NF and continuum in neutron-rich oxygen isotopes</i>	33
4.2.3	<i>3NF and continuum in proton-rich Borromean ^{17}Ne</i>	34
4.2.4	<i>The calcium isotopes dripline</i>	36
4.3	<i>Shell evolution and the role of three-body forces</i>	39
4.3.1	<i>Overview: the fp shell region</i>	39
4.3.2	<i>Monopole interaction and effective single-particle energies</i>	41
4.3.3	<i>Spin-tensor decomposition of the shell-model interaction</i>	47
5	Summary and conclusions	51
A	Three-body matrix elements for shell-model calculations	53
A.1	Three-body states	53
A.2	Antisymmetrization	54
A.3	Structures of three-body matrix elements	56
A.3.1	<i>JT-coupled three-body matrix elements</i>	56
A.3.2	<i>Chiral three-body potentials and nonlocal regularization</i>	57
A.3.3	Contact term	59
A.3.4	One-pion exchange plus contact term	60
A.3.5	Two-pion exchange term	60

1 Introduction

The awareness of a defined role of many-body forces in the study of nuclear systems traces back to the early stages of meson theory [1]. As a matter of fact, there is no guarantee that the picture of the meson degrees of freedom to be frozen as soon as they have created the interaction between two nucleons – and then being responsible only for two-nucleon forces (2NFs) – may work in any nuclear environment, in any energy regime, and, more significantly, within any desired degree of accuracy [2, 3].

The theoretical progress in the construction of high-quality nucleon-nucleon (NN) potentials able to reproduce large sets of two-nucleon data [4, 5], as well as the advancement of high-precision nuclear

structure approaches [6, 7], has established that the sole use of two-body nuclear forces does not provide a fully satisfactory reproduction of the low-energy spectroscopy of light nuclear systems [8].

However, two main issues have slowed the development of nuclear structure calculations employing three-nucleon forces (3NFs). First, the little knowledge of a mechanism providing many-body forces consistently with the nature of the NN interaction, as, for example, the pion-nucleon (πN) scattering amplitude which is a fundamental quantity to construct 3NF contributions in meson theory [3]. Second, the difficulty to manage three-nucleon (3N) potentials within a many-body system, whose solution requires formalisms that are computationally extremely demanding.

As regards the first issue, a major breakthrough in the last two decades has been the derivation of nuclear potentials in terms of the chiral perturbation theory (ChPT) to build realistic NN and 3N forces starting from a chiral Lagrangian. This idea goes back to the seminal work of Weinberg [9–11], where the concept of an effective field theory (EFT) has been introduced to study the S -matrix for processes involving arbitrary numbers of low-momentum pions and nucleons. Within such an approach, the long-range component of the potential is ruled by the symmetries of low-energy quantum chromodynamics (QCD) – as the spontaneously broken chiral symmetry – and the short-range dynamics is absorbed into a complete basis of contact terms that are proportional to low-energy constants (LECs). The LECs may be fitted to NN and 3N data, but in a future they could be determined by extrapolating them from lattice QCD (LQCD) results for light nuclear systems at the physical π mass [12, 13].

The main advantage of ChPT, as regards the need of consistency between NN and 3N potentials, is that it generates nuclear two- and many-body forces on an equal footing [14–17]. In fact, most interaction vertices that appear in the three- and four-nucleon forces also occur in the two-nucleon ones. Since the LECs associated to these vertices are shared with the chiral NN potential, then consistency requires that for the same vertices the same parameter values are used in the many-body components of the nuclear Hamiltonian.

This new generation of two- and three-nucleon forces has been successfully employed to study both spectroscopic properties and scattering processes of light systems within the framework of the *ab initio* no-core shell model (NCSM) method [6, 18–20].

However, the computational difficulty to manage a full treatment of three-body correlations increases rapidly with the mass of the nuclei under investigation making calculations unfeasible. A successful approach to overcome such a hindrance is to resort to the so-called normal-ordered decomposition of the three-body component of the nuclear Hamiltonian [21]. This is a convenient procedure in nuclear many-body methods which starts from an unperturbed reference state. The basic idea is to use the Wick’s theorem [22] and re-arrange, with respect to the reference state, the three-body component of the nuclear Hamiltonian into a sum of zero-, one-, two-, and three-body terms [23]. Then, a truncation is performed neglecting the residual three-body term, which arises from the normal-ordering decomposition, and retaining only the zero-, one-, and two-body contributions. This approximation is obviously advantageous to simplify the theoretical expressions characterizing different nuclear many-body methods, and to drastically reduce the computational complexity. The validity of the normal-ordering approximation has been tested in light- and medium-mass nuclei [24–26], and it is currently a building block of *ab initio* nuclear structure calculations where chiral NN and 3N potentials are employed [21, 27–33].

The question of the significance of including the effects of 3NFs in the derivation of the effective shell-model (SM) Hamiltonians H_{effS} becomes crucial when they are obtained by way of the many-body theory starting from realistic nuclear potentials [34–38]. In fact, for phenomenological H_{effS} , where the single-particle (SP) energies and the two-body matrix elements (TBMEs) of the residual interaction are fitted or adjusted so as to reproduce a certain set of spectroscopic observables [39, 40], it is reasonable to conclude that 3N forces are implicitly taken into account.

The first studies about the role of 3NFs in nuclear SM calculations have been carried out by Zuker and coworkers (see Ref. [41], where a complete list of reference can be found), who have extensively investigated the characteristics of the TBMEs of the residual SM interaction derived within the many-

body perturbation theory (MBPT) from realistic 2NFs by Kuo and Brown [42,43]. They have shown that these H_{eff} s need to be modified in their monopole component to reproduce the experimental evolution of shell closures as a function of the number of valence nucleons [44–46]. The inferred conclusion is that this deficiency traces back to the lack of a 3NF component in the nuclear realistic Hamiltonian, which affects negatively the H_{eff} monopole component, as discussed in Ref. [47] that was inspired by the NCSM results of Ref. [48] indicating the need of 3NF in describing p -shell nuclei and in particular the ground state of ^{10}B .

This is not a negligible drawback for a SM calculation, since the ability to describe the evolution of the nuclear spectroscopic properties along isotopic and isotonic chains, and consequently the formation of magic numbers, is the feature that has placed the SM in a central role within the structure of atomic nuclei, and represents also its main success [49–51]. Moreover, the H_{eff} monopole component affects also the evolution of the calculated binding energies as a function of the number of valence nucleons along isotopic and isotonic chains, and then the ability of SM calculations to reproduce or predict correctly the edge of the nuclear chart. This is the reason why it is fundamental that H_{eff} s should be able to reproduce the observed shell evolution and closures.

The first SM study where the effects of 3NFs have been explicitly included in the derivation of H_{eff} has been carried out by Otsuka and coworkers in order to reproduce the oxygen-isotope dripline [52]. In this work, the authors aimed to study what are the underlying conditions to reproduce the limit of oxygen isotopes as bound systems, which is experimentally very close to the stability line [53,54]. To this end, they derived an effective Hamiltonian for the sd -shell model space within the MBPT framework [36], starting from a realistic NN potential as well as from an $NN+3N$ potential. The two-body component of the nuclear Hamiltonian was chosen to be a potential constructed by way of the ChPT at next-to-next-to-next-to-leading order ($N^3\text{LO}$) [55], whose high-momentum components were renormalized by way of the $V_{\text{low-}k}$ procedure [56], while the three-body contribution was given by the Fujita-Miyazawa Δ -exchange force [57] or the chiral 3NF term at $N^2\text{LO}$. In order to manage the 3N component in SM calculations, its contribution was evaluated by way of the previously mentioned normal-ordering approximation, and such a contribution was shown to be crucial to obtain ^{24}O as the last bound oxygen isotope.

Starting from the work of Ref. [52] extensive studies have then carried out on the role of 3NFs in SM calculations to reproduce the spectroscopy and the binding energies of nuclei belonging to the sd -shell region [58–62], as well as to investigate and predict the nuclear structure of heavy calcium isotopes [25,59,61,63]. For all these works, the H_{eff} s have been derived starting from two- and three-body potentials built up within the chiral perturbative expansion and softened by way of the $V_{\text{low-}k}$ technique [56] or the similarity renormalization-group (SRG) approach [64,65].

Chiral NN and 3N forces have been also the starting point of non-perturbative approaches to the derivation of H_{eff} , such as the SM coupled cluster (SMCC) [66–68] and the valence-space in-medium SRG (VS-IMSRG) [69,70], and a comprehensive review about tackling the problem of deriving H_{eff} within *ab initio* methods can be found in Ref. [37] where an extension of the normal-ordering approximation using a multi-reference state is also outlined. In particular, calculations within the VS-IMSRG approach have validated the need of 3NFs to reproduce the experimental behavior of ground-state (g.s.) energies of oxygen and calcium isotopes [37], and have been employed to provide theoretical insight in many experimental works [71–81].

In 2018, the authors of the present work have started a research plan aimed to employ chiral two- and three-body potentials both in standard SM calculations as well as in Gamow SM (GSM) [82–84], the latter being focused on the description of weakly-bound nuclei by coupling bound to resonant states (Gamow states). The main goal of such an investigation is to single out the role of 3NF among the main components of the residual SM interaction, starting from nuclear potentials based on ChPT and linked to the QCD, namely the fundamental theory of strong interactions [85].

In the first work of our project, we have studied the spectroscopy of p -shell nuclei [86] by employing

an H_{eff} derived from an NN potential obtained within the ChPT at $N^3\text{LO}$ [55], and including also one- and two-body components of a normal-ordered 3N chiral potential at $N^2\text{LO}$. The matrix elements of the 3NF have been constructed using consistently the same LECs belonging to the components of the 2NF, the only two extra LECs c_D, c_E – which are attached to the 3N 1- π exchange and contact terms, respectively – have been chosen to be the same as fixed in Ref. [87]. With this choice of the NN and 3N forces we have intended to benchmark our SM results with those of *ab initio* NCSM for the same class of nuclei [87,88] in order to verify the quality of the approximations which characterize our calculations.

The results reported in that paper evidenced a substantial agreement between the SM and NCSM calculations, and a positive assessment for the MBPT to provide reliable H_{eff} s starting from NN and 3N forces. Furthermore, it is worth emphasizing that in Ref. [86] we have shown that the 3NF is essential to make explicit the spin-orbit splitting of the $0p$ orbitals.

The success of this work has been the starting point for further SM studies, and the focus has been shifted to nuclei belonging to fp shell, which provide the best paradigm to investigate the role of 3NFs to reproduce the observed shell evolution of isotopic chains belonging to this region. In Ref. [89], it has been shown that 3NFs are crucial to obtain the shell closure at $N = 28$, and to provide SP-energy splittings which are consistent with the interpretation of ^{56}Ni as a doubly magic nucleus. This feature has been the cornerstone to obtain the evolution of the excitation energies of the yrast $J = 2^+$ states of calcium, titanium, chromium, iron, and nickel isotopes in agreement with the experimental one [89].

The paper on fp nuclei has triggered two following studies on the location of the neutron dripline for calcium [90] and titanium [91] isotopic chains, both aimed to assess the relevance of accounting for induced many-body forces, which originate from the 2NF in nuclei with more than two valence nucleons (see Section 2.1). For a thorough SM investigation of Ca and Ti isotopes, which are experimentally found to be stable beyond $N = 40$, these two works adopt a model space larger than the standard fp shell including the neutron $0g_{9/2}$ orbital. Such an enlargement of the number of configurations of the nuclear wave functions, which pushes the performance of the available SM codes to their computational limits, has been proven to be important to improve the agreement between theory and experiment.

As mentioned previously, the role of 3NFs has been investigated in the framework of the GSM [82–84] for weakly-bound nuclei. In Ref. [92], the three-body component of the nuclear Hamiltonian and continuum states have been shown to be fundamental to reproduce the dripline position and the unbound properties of oxygen isotopes beyond the dripline. The GSM, with the inclusion of 3NFs, reproduces the experimental resonance widths of the ^{24}O excited states, and predicts the particle-emission widths for other resonant states in $^{24,25,26}\text{O}$.

The GSM with chiral NN and 3N forces has been employed also to study the structure of the halo nucleus ^{17}Ne , and it has been observed that the repulsive behavior of the 3NF is decisive to raise the energy of ^{16}F over the threshold of the proton emission, leading to the Borromean nature of ^{17}Ne [93].

In a recent work, the focus has been spotted on the mirror-symmetry breaking of sd -shell mass region, and it has been found that, for $Z(N) = 8$ isotopes (isotones), 2NFs only cannot provide the correct binding energies, nucleon separation energies and excitation spectra [94].

Let us now outline the structure of the present work. In the following section, we sketch out the essentials of our understanding of nuclear many-body forces and the framework of deriving nuclear potentials in terms of chiral EFT. In Section 3 we present the nuclear SM, which is the many-body method where our calculations are grounded on, and the theoretical aspects related to the derivation of effective SM operators starting from realistic nuclear forces. In Section 4, we review a large variety of the latest nuclear structure calculations that have been performed in terms of SM employing realistic two- and three-body potentials. Results for nuclei ranging from light and weakly-bound systems up to intermediate-mass nuclei belonging to the fp shell are presented, with the aim to investigate the role of 3NFs in explaining phenomena such as the location of neutron dripline of isotopic chains, the Borromean structure of halo nuclei, as well as the shell evolution as a function of the number of valence nucleons. The last section is devoted to summarizing our considerations about the current status of

SM with three-body potentials, and to looking over the future evolution of this kind of approach to the study of nuclear structure problems. In the appendix A, we present a few of the theoretical details of the methods which are needed to employ 3NFs in SM calculations.

2 Three-body forces

2.1 Backgrounds

As mentioned in the Introduction, the first example of three-body force was the electromagnetic force introduced by Primakoff and Holstein in their seminal paper in Ref. [1], where they introduced a three-body term in a non-relativistic Schrödinger equation to account for the creation of relativistic particle-antiparticle pairs. In the very same paper, the authors employed the meson theory of the nuclear force among nucleons, analogously to the electromagnetic one among charged particles, to introduce the contribution of a three-nucleon potential.

Actually, a theoretical framework that assumes the meson exchange as the source of the two-nucleon potential but, at the same time, freezes the meson degrees of freedom out of many-body systems is not a consistent picture [3]. This means that meson exchange should be also considered the source of three-, four-, ..., many-nucleon forces, whose relevance with respect to the two-nucleon one is somehow model-dependent.

There are a few indications that the inclusion of a 3NF, alongside a 2NF, may improve the quality of theoretical calculations in reproducing the observables of three-nucleon systems. The role of 3NFs may be considered circumstantial, in other words, there is evidence that some specific theoretical results cannot be improved, when compared with data, by considering only a two-body component for the nuclear potential [2].

More precisely, the introduction of a 3NF may lower the discrepancy between the experimental and theoretical binding energies (BEs), charge radii, and charge form factors of ^3H and ^3He in terms of non-relativistic nuclear models. Calculations of three-nucleon systems in terms of a realistic 2NF only suffer a bad correlation between BE and charge radius. In fact, 2NFs that reproduce the experimental dimension of the nucleus underestimate the BE and, viceversa, if the theory reproduces the correct BE then the radius is too small. Another observable whose reproduction evidences the need of resorting to three-body forces is the charge form factor of the three-nucleon system ^3He [95]. As a matter of fact, the ^3He charge density, which can be obtained from the experimental charge form factor as a function of the momentum transfer, exhibits a “hole” in the inner part of the nuclear volume at variance with a flat profile that is obtained with calculations performed with 2NF only (see Fig. 3 in Ref. [2]).

The inclusion of 3NFs, as well as of two-body electromagnetic meson-exchange currents [96, 97], to calculate ^3H , ^3He charge form factors has been proved to be crucial in order to reproduce data [98]. Both of them - 3NF and meson-exchange currents - originate from the same source of many-body nuclear forces: nucleons are not point-like particles, and their quark structure needs to be accounted effectively in terms of meson exchange and extra degrees of freedom.

These concepts of extra degrees freedom and meson exchange among nucleons introduce us to the basic question: what is the definition of a 3NF in terms of microscopic degrees of freedom?

A sound definition of nuclear many-body forces is the one which can be found in Refs. [2, 3], namely we should express them as irreducible functions of coordinates or momenta of N nucleons by way of irreducible Feynman diagrams which cannot be generated by iterating NN interactions. The contributions that are represented by diagrams constructed merely as products of 2NF vertices are then named induced many-body forces, and they are taken into account by the diagonalization of the nuclear Hamiltonian of the many-body method employed to calculate energies and wave functions.

To exemplify, in Fig. 1 we have reported a diagram which, in a nuclear model based on a NN

potential including one-pion exchange component, corresponds to an induced 3NF that is distinct from a genuine 3NF.

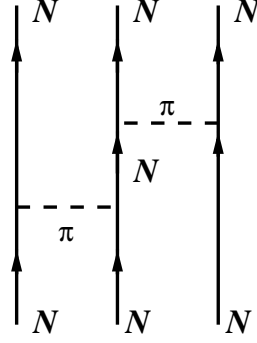


Figure 1: Induced 3NF constructed iterating two one-pion exchange 2NF.

The distinction between many-body forces and correlations is based on the choice of the internal degrees of freedom of a nucleus. For example, if the adopted nuclear model freezes out the Δ -isobar degree of freedom, then many-body diagrams that include the Δ as an intermediate state between two-body vertices are to be considered as a component of a real many-body force.

The most commonly considered 3NF in meson-exchange nuclear models is the so-called 2π -exchange three-nucleon force (2π -3NF), which is reported as diagram *a* in Fig. 2.

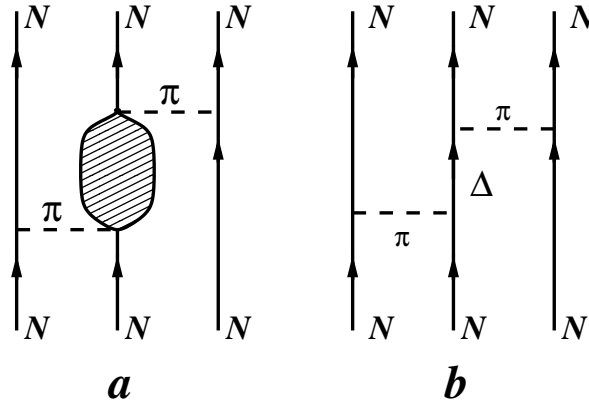


Figure 2: Diagram *a*: 2π -exchange three-nucleon force. Diagram *b*: Fujita-Miyazawa force. See text for details.

The first one is to approach the problem by using the current algebra and partially-conserved axial-current (PCAC) constraints to extrapolate the off-mass-shell parametrization of the π -N scattering amplitude from on-mass-shell properties [99]. This way has generated the well-known Tucson-Melbourne 3N potential [100, 101], which has been employed for the calculations of infinite nuclear matter [100].

The other way to develop 3NFs is to resort to field theory by carrying out a diagrammatic expansion. A relevant component of such a model is the celebrated Fujita-Miyazawa force [57], where a component of the off-shell amplitude is the scattering into an intermediate Δ -isobar state, that is reported as diagram *b* in Fig. 2. This pioneering potential has been the first attempt to frame nuclear 3NFs in terms of meson exchange, and has been considered for calculations of the nuclear equation of state of infinite nuclear matter (EOS) [102, 103] as well as for nuclear structure studies for finite nuclei [52]. It is worth mentioning that a good description of the nuclear matter saturation properties can be also provided by a relativistic meson exchange potential, as discussed in Ref. [104].

The above mentioned approaches suffer both the lack of a proper hierarchy in the perturbative expansion of the nuclear Hamiltonian and tight connection between the derivation of the NN and $3N$ forces. This drawback has been overcome in the last twenty years with the advent of a new theoretical approach to the derivation of nuclear forces, based on the ChPT, where the starting point is a chiral Lagrangian which traces back to the work of Weinberg [9–11], calling in the concept of EFT for S matrix in processes with an arbitrary numbers of low-momentum pions and nucleons.

In the following section, the approach to many-nucleon forces in the framework of ChPT will be sketched out in its essentials.

2.2 Chiral effective field theory for three-nucleon forces

As mentioned in Section 1, the derivation of high-precision nuclear potentials based on ChPT represents a major breakthrough in the last two decades [16, 17, 55, 105, 106]. Nowadays, this class of theoretical potentials is widely employed to link the fundamental theory of strong interactions, QCD, to nuclear many-body systems.

The derivation of nuclear forces starting from a chiral Lagrangian is framed within the EFT, by employing an arbitrary number of low-momentum pions and nucleons. The long-range forces are then ruled by the symmetries of low-energy QCD and, particularly, by the spontaneously broken chiral symmetry. The short-range dynamics is absorbed into a complete basis of contact terms that are proportional to LECs, which are determined in order to reproduce few-body-system data.

In our perspective – that focuses on the role of 3NFs in the study of the structure of finite nuclei – the main advantage of ChPT is that it generates nuclear two- and many-body forces on an equal footing [14–16]. Moreover, most interaction vertices that appear in the 3NF and in the four-nucleon force (4NF) also occur in the 2NF. This means that the parameters carried by these vertices, as well as the LECs of the 2NF contact terms, are determined by the construction of the chiral 2NF, and consistency then requires that the same parameter values should be inserted at the same vertices in the many-body-force contributions.

When the chiral perturbation expansion is performed, the first non-vanishing 3NF occurs at $N^2\text{LO}$ [16, 17]. At this order, there are three 3NF topologies: two-pion exchange (2PE), one-pion exchange plus a NN -contact interaction (1PE), and pure 3N-contact interaction. The three topologies are reported in Fig. 3.

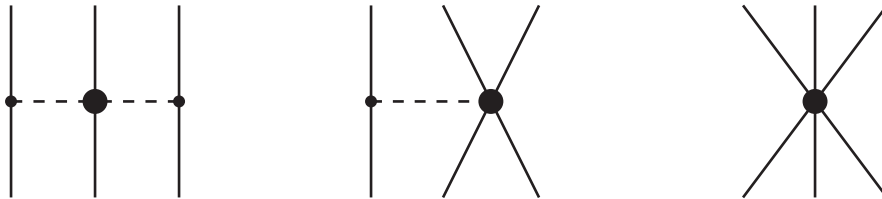


Figure 3: The three-nucleon potential at $N^2\text{LO}$. From left to right: 2PE, 1PE, and contact diagrams.

The 2PE 3N-potential is given by

$$v_{3N}^{(2\pi)} = \left(\frac{g_A}{2f_\pi}\right)^2 \frac{1}{2} \sum_{i \neq j \neq k} \frac{(\boldsymbol{\sigma}_i \cdot \mathbf{q}_i)(\boldsymbol{\sigma}_j \cdot \mathbf{q}_j)}{(q_i^2 + m_\pi^2)(q_j^2 + m_\pi^2)} F_{ijk}^{ab} \tau_i^a \tau_j^b. \quad (1)$$

Here, $\boldsymbol{\sigma}_i(\boldsymbol{\tau}_i)$ is the Pauli spin (isospin) matrix of nucleon i , and the transferred momentum is $\mathbf{q}_i \equiv \mathbf{p}'_i - \mathbf{p}_i$, with \mathbf{p}_i and \mathbf{p}'_i being the initial and final momenta, respectively. The other quantities entering the

expression are the axial coupling constant g_A , the pion mass m_π , and the pion-decay constant $f_\pi = 92.4$ MeV, by using natural units, namely $c = \hbar = 1$. In the above expression we have used the definition

$$F_{ijk}^{ab} = \delta^{ab} \left[-\frac{4c_1 m_\pi^2}{f_\pi^2} + \frac{2c_3}{f_\pi^2} \mathbf{q}_i \cdot \mathbf{q}_j \right] + \frac{c_4}{f_\pi^2} \sum_c \epsilon^{abc} \tau_k^c \boldsymbol{\sigma}_k \cdot (\mathbf{q}_i \times \mathbf{q}_j). \quad (2)$$

It is worth noticing that the 2PE contribution to the structure of the 3NF does not contain any new parameters with respect to those appearing in the expression of the N²LO 2NF, because the LECs c_1 , c_3 , and c_4 have to be determined when fitting the 2NF to the data of the two-nucleon system.

The 1PE contribution is

$$v_{3N}^{(1\pi)} = -\frac{c_D}{f_\pi^2 \Lambda_\chi} \frac{g_A}{8f_\pi^2} \sum_{i \neq j \neq k} \frac{(\boldsymbol{\sigma}_i \cdot \mathbf{q}_j)(\boldsymbol{\sigma}_j \cdot \mathbf{q}_i)}{q_j^2 + m_\pi^2} \boldsymbol{\tau}_i \cdot \boldsymbol{\tau}_j, \quad (3)$$

with $\Lambda_\chi = 700$ MeV.

The 3N contact potential reads

$$v_{3N}^{(\text{ct})} = \frac{c_E}{f_\pi^4 \Lambda_\chi} \frac{1}{2} \sum_{j \neq k} \boldsymbol{\tau}_j \cdot \boldsymbol{\tau}_k. \quad (4)$$

The last two 3NF terms involve the two new LECs c_D and c_E , which do not appear in the two-body problem. There are many ways to constrain these two parameters. For example, the triton binding energy and the nd doublet scattering length $^2a_{nd}$ or the ^4He binding energy can be used. However, because it is well-known that there is a correlation between these observables, an optimal over-all fit of the properties of light nuclei is needed, as it has been done in Ref. [87]. Another approach to fix c_D and c_E is to consider the consistency of interactions and currents in chiral EFT [107, 108], since c_D that appears in $v_{3N}^{(1\pi)}$ is also involved in the two-nucleon contact term in the NN axial current operator derived up to N²LO. Therefore, c_D may be constrained using the accurate experimental value of one observable from weak processes involving two- or few-nucleon systems. This procedure has been followed in Ref. [109], where the triton β -decay half-life, in particular its Gamow-Teller (GT) component, was used. The same choice was already adopted in a variety of previous studies to constrain the two-body axial current operator [110].

Because of the great success of ChPT nuclear forces in nuclear structure calculations, the N²LO three-body potential is the one that has been mostly employed in SM calculations with realistic 3NFs. The N²LO 3N potential is defined in momentum space and, in order to employ this potential in the derivation of the effective SM interaction, its matrix elements must be calculated in the harmonic-oscillator (HO) basis following a procedure that has been first reported in Ref. [87], for a potential characterized by a local regulator in momentum space.

As concerns 3NFs beyond N²LO, their contributions remain unclear. At N³LO, the two-pion exchange 3NFs produce rather weak effects for the nucleon-deuteron system [111], while the short-range 3NFs may be significant [112]. The short-range 3NFs at N⁴LO, where thirteen LECs newly appear, may give sizeable contributions [113, 114].

In Appendix A, one can find the details on the calculation of the N²LO 3NF matrix elements in the HO basis, but employing a nonlocal regulator function.

3 Shell model

3.1 Generalities

The nuclear SM represents one of the most powerful tools for understanding the structure of atomic nuclei, in which the complexity of the nuclear many-body problem is reduced by considering only a limited

number of microscopic degrees of freedom while the missing ones are taken into account by employing effective operators.

This model is based on the assumption that each nucleon moves in a mean field created by the remaining $A - 1$ nucleons. The mean field gives rise to a shell structure, composed of single-particle states (*orbitals*) grouped in shells, which are well separated in energy from each other. To a first approximation, the nucleus can be considered as an inert core, made up of shells filled with neutrons and protons paired to total angular momentum $J = 0$, with the remaining nucleons (*valence nucleons*) located in orbitals on top of the inert core. Within the SM, which is also called the “interacting shell model” to underline the difference with the simple independent-particle description, the valence nucleons interact in a truncated space (*valence space*) spanned in general by a single proton and/or neutron shell above the inert core. Then, all the orbitals above the valence space are regarded as empty and constitute the external space. It is worth pointing out that in modern SM calculations larger valence spaces are considered, including proton and neutron cross-shell excitations, to describe some features of exotic neutron-rich nuclei.

The SM is nowadays a well-established approach to investigate nuclei in different mass regions, as testified by the large number of successful calculations carried out during the 70 years since its introduction. The real beginning of the SM dates back to the end of 1940s and is connected to the publication of the papers by Mayer [49] and Haxel *et al.* [50], even if the existence of shell structure was already evidenced during the previous two decades. It was, in fact, realized that nuclei with specific numbers of protons and/or neutrons (*magic numbers*) are more stable than others, which can be interpreted as a manifestation of an independent particle behavior. However, it was crucial for explaining the experimental regularities associated with the magic numbers the addition of a strong attractive spin-orbit term to the central mean field, as proposed in Refs. [49, 50].

It became immediately clear that the description of nuclei only in terms of a simple mean-field potential was a very crude approximation, and the inclusion of the interaction between valence nucleons was indispensable to break up the degeneracies when considering systems with two or more particles outside doubly-closed nuclei. Therefore, soon after the publication of the Mayer and Haxel’s papers, a variety of two-body interactions was developed – essentially for single-orbital configurations – using central forces with different radial dependencies and including spin and isospin terms. A review of these first SM calculations can be found in Ref. [115].

The construction of interactions to be used in SM has always been a central issue within this approach, and still it is. The use of phenomenological interactions, which contain a certain number of parameters adjusted to reproduce the experimental data, has been largely adopted in SM calculations, but at the same time significant efforts have been focused on the derivation of microscopic interactions starting from realistic nuclear forces, namely from the bare nuclear potentials determined from scattering experiments.

Before discussing this point in more detail, we would like to introduce the effective SM Hamiltonian, that in the coupled representation can be written as

$$H_{\text{eff}} = \sum_a \epsilon_a N_a - \frac{1}{4} \sum_{abcdJ} \langle ab; J | V_{\text{eff}} | cd; J \rangle (-1)^J [a_a^\dagger a_b^\dagger]^J \cdot [\tilde{a}_c \tilde{a}_d]^J, \quad (5)$$

where the symbol (\cdot) indicates the scalar product as usual, while the latin indices run over the orbitals of the neutron and proton valence spaces and stand for (nlj) , with n being the radial quantum number, l and j , respectively, the orbital and total angular momentum. We have used the $a_{am_a}^\dagger$ and $\tilde{a}_{am_a} = (-1)^{j_a+m_a} a_{a-m_a}$ operators which, respectively, creates and annihilates one particle in a state of the underlying mean field, with m_a associated to the z component of j_a . The one-body component of H_{eff} is written in terms of the SP energies and the number operator $N_a = (-1)^{j_a} a_a^\dagger \cdot \tilde{a}_a$. The TBMEs are antisymmetrized but unnormalized.

The eigenvalue problem of the Hamiltonian (5) can be solved by employing as basis states appropriate combinations of the Slater determinants

$$[\underbrace{a_{am_a}^\dagger a_{bm_b}^\dagger a_{cm_c}^\dagger \dots}_{\mathfrak{N}}] |C\rangle, \quad (6)$$

where the set of SP orbitals ($a, b, c \dots$) corresponds to a given configuration and \mathfrak{N} is the number of valence nucleons. The unperturbed doubly-closed core, $|C\rangle$, can be explicitly written as

$$|C\rangle = \prod_{am_a \in \text{filled shells}} a_{am_a}^\dagger |0\rangle. \quad (7)$$

In present days, there are several open source codes for performing SM calculations, such as NuShellX [116], BIGSTICK [117], ANTOINE or NATHAN [41], KSHELL [118], MFDN [119] and others (see [120] for more details).

Some of them are developed for massive parallel computation and, therefore, can run on high-performance computing clusters. These type of codes are able to handle up to ~ 100 billion dimensions, making it possible to approach nuclei with many valence nucleons in large valence spaces.

One component of H_{eff} relevant for the following discussion is given by the monopole interaction, which, using explicitly the indices τ, τ' for proton or neutron, takes the form

$$H_{\text{mon}} = \sum_{a\tau} \epsilon_{a\tau} N_{a\tau} + \frac{1}{2} \sum_{ab\tau\tau'} \frac{\bar{V}_{ab}^{\tau\tau'} N_{a\tau} (N_{b\tau'} - \delta_{ab} \delta_{\tau\tau'})}{\sum_J \hat{J}^2} \quad (8)$$

where the angular momentum J runs on all allowed values and the notation $\hat{J} = \sqrt{2J+1}$ is used. The matrix elements $\bar{V}_{ab}^{\tau\tau'}$ are defined as

$$\bar{V}_{ab}^{\tau\tau'} = \frac{\sum_J \hat{J} \langle a\tau b\tau'; J | V_{\text{eff}} | a\tau b\tau'; J \rangle}{\sum_J \hat{J}}, \quad (9)$$

and represent the angular-momentum averaged TBMEs, or centroids of the interaction.

The monopole interaction corresponds to the spherical mean field as extracted from the SM Hamiltonian in open-shell nuclei [41] and therefore governs the evolution of the SP energies along isotopic and isotonic chains. Starting from the monopole interaction, effective single particle energies (ESPEs) are defined

$$\text{ESPE}(a\tau) = \epsilon_{a\tau} + \sum_{b\tau'} \bar{V}_{ab}^{\tau\tau'} n_b^{\tau'}, \quad (10)$$

which, as compared to the SP energies of the SM Hamiltonian (Eq. (5)), incorporate the mean effects from other nucleons outer the inert core (see, for instance, Ref. [121]). Here the g.s. occupation number of the proton/neutron b orbital is denoted by $n_b^{\tau'}$.

Once energies E_α and wave functions $|\psi_\alpha\rangle$ of the system under consideration are determined by solving the eigenvalue problem for the Hamiltonian of Eq. (5), it is possible to compute the matrix elements of operators which are related to physical quantities, like electromagnetic transitions and decay strengths, or appear in form factors needed to evaluate reaction cross sections. The matrix elements for one-body operators can be written as

$$\langle \psi_f | \Theta_{\text{eff}}^\lambda | \psi_i \rangle = \sum_{ab} \frac{\langle \psi_f | [a_a^\dagger \tilde{a}_b]^\lambda | \psi_i \rangle}{\hat{\lambda}} \langle a | \Theta_{\text{eff}}^\lambda | b \rangle = \sum_{ab} \text{OBTD}(fiab\lambda) \langle a | \Theta_{\text{eff}}^\lambda | b \rangle, \quad (11)$$

where the one-body transition densities (OBTDs) represent in a compact form the nuclear structure information on the initial and final states involved in the process. Note that we have added the label

“eff” to Θ^λ to point out that a different operator with respect to the bare one should be used with SM wave functions, since, as for the Hamiltonian, renormalizations due to the adopted truncated space are needed.

As mentioned above, the choice of the Hamiltonian is one of the most crucial issues in the SM approach, which attracted the attention of the nuclear community from the very beginning. At first, interest was essentially addressed to the development of phenomenological schematic interactions, which are parametrized functions of nucleon coordinates with very simple or more complicated structures, depending on the included exchange operators. Between them, we mention the δ and pairing forces, which, even if very simple, account for the short-range nature of the residual interaction and its tendency to correlate nucleons in zero-coupled pairs ($J^\pi = 0^+$).

Contemporaneously, there were efforts to derive the SM Hamiltonian from a realistic interaction between nucleons. It was soon evident that the peculiar properties of the bare potential, containing a strong repulsive core at short distances, prevent the description of the nucleus in terms of mean field and consequently within the SM framework. However, the introduction of the G matrix by Keith Brueckner and coworkers [122] was the first milestone for the development of a microscopic interpretation of the SM. In the G matrix, strong short-range correlations are renormalized by summing all two-particle ladder-type interactions. It can be, therefore, used to perform Hartree-Fock self-consistent calculations or taken, in principle, as residual interaction in SM calculations. A further relevant step along this line is represented by the paper of Kuo and Brown [42], in which a new effective interaction was derived for the sd shell starting from the G matrix by a perturbative expansion including terms up to second order in G , namely the so-called *bubble* diagrams corresponding to one particle-one hole ($1p - 1h$) core-polarization excitations.

These pioneering works made it evident that the interaction used in SM calculations cannot be the bare one between free nucleons. In fact, the SM Hamiltonian is defined in a reduced space, and should therefore account – in an effective way – for the omitted degrees of freedom, namely for the excitations of core particles into the valence and external spaces as well as for the excitations of valence particles in the external space. Then, as testified by the large number of papers published on the subject, great attention was dedicated to the derivation of the effective SM Hamiltonian within a perturbative approach and to the assessment of its role in the study of nuclear structure. Nowadays, substantial progress has been made regarding the starting bare potential as well as the many-body technique for constructing the effective interaction, that will be presented in detail in forthcoming sections.

Within the class of phenomenological interactions, in which the introduced parameters are adjusted to reproduce a selected set of experimental data, an alternative way to the schematic interactions, introduced by Talmi in Ref. [123], consists in considering the Hamiltonian matrix elements themselves as free parameters. This approach is quite successful, and a comprehensive discussion and presentation of such a procedure can be found in Refs. [41, 115, 121, 124, 125]. Here, we report just a few examples of this kind of interactions, as the p -shell interaction by Cohen and Kurath [39], the so-called universal interaction developed for the sd shell by Brown *et al.* [40, 126], or the GXPF1 [127] and JUN45 [128] interaction by M. Honma *et al.*, respectively, for the fp and $f_{5/2}p_{g_{9/2}}$ valence spaces. For large valence spaces, the number of matrix elements increases drastically and they are determined by choosing a starting Hamiltonian, as for instance the G matrix of a realistic NN potential, and using the linear combination method of Ref. [40], where only selected linear combinations of matrix elements are varied to fit experimental data. All these phenomenological interactions have been largely used in nuclear structure studies providing a successful description of a certain variety of phenomena.

It is worthwhile to point out that in the vast majority of SM calculations, only two-body interactions have been used. As mentioned in the Introduction, the explicit inclusion of 3NFs has historically been neglected in SM treatment due to the ambiguity in producing a 3N term consistent with the NN one, as well as to the difficulty in handling such a term in many-body systems. On the other hand, the good agreement between theory and experiment obtained with SM calculations employing

phenomenological interactions suggests that the effects of 3NFs can be empirically taken into account. We already mentioned that Zucker and coworkers [47] argued that the main effects of 3NFs concentrate in the monopole component of the effective interaction.

As a matter of fact, modifications of the monopole component were first proposed, without a clear connection with 3NFs, to cure the deficiencies of effective Hamiltonians derived from realistic NN potentials related to their bad saturation and shell formation properties [129]. The phenomenological adjustment of monopole terms in realistic effective Hamiltonians has been largely applied by the Strasbourg-Madrid group to various mass regions providing interactions able to give an accurate description of the nuclear spectroscopy. Examples of monopole corrected interactions are KB3 [129] in the fp shell, SDPF-U [130] in the $sdfp$ shell, and LNPS [131] including the fp shell for protons and the $f_{5/2}pg_{9/2}d_{5/2}$ orbitals for neutrons.

In the last decade SM calculations that explicitly take into account 3NF have been carried out and they will be discussed in detail in the following sections.

3.2 *The derivation of realistic effective interactions and operators*

The SM is grounded on the ansatz that each nucleon belonging to a nucleus moves independently in a spherically symmetric auxiliary potential, which accounts for the average interaction with the other protons and neutrons. This potential is usually described by a Woods-Saxon (WS) or an HO potential including a spin-orbit term. Actually, it is clear that the residual interaction between valence nucleons, which is not explicitly included in the one-body auxiliary potential, has to be considered to describe quantitatively the low-energy structure of nuclei with two or more valence nucleons confined to move in the valence space. In fact, the action of the residual interaction generates a mixing of different configurations thus removing the degeneracy of states belonging to the same configuration.

In general, when considering only the valence nucleons interacting in the reduced number of orbitals of the valence space, one is left with the problem to construct a SM Hamiltonian and decay operators defined in a truncated space, but whose matrix elements should account for the neglected degrees of freedom. Namely, we need an effective Hamiltonian H_{eff} and effective decay operators Θ_{eff} .

We start by sketching out the fundamentals of the derivation of H_{eff} in a formal way, by considering, without loss of generality, an A -body Hamiltonian with no transitional invariance. This is appropriate in SM calculations performed including only one proton and/or neutron major shell above the closed core. A purely intrinsic Hamiltonian will be introduced in Section 3.3. The full Hilbert-space eigenvalue problem is then written as

$$H|\Psi_\alpha\rangle = E_\alpha|\Psi_\alpha\rangle, \quad (12)$$

where

$$H = H_0 + H_1, \quad (13)$$

and

$$H_0 = \sum_{i=1}^A \left(\frac{p_i^2}{2m} + U_i \right), \quad (14)$$

$$H_1 = \sum_{i<j=1}^A V_{ij}^{NN} - \sum_{i=1}^A U_i. \quad (15)$$

As mentioned before, to introduce the SM framework we must consider an auxiliary one-body potential U to break up the nuclear Hamiltonian as the sum of a one-body term H_0 , which describes the independent motion of the nucleons, and the residual interaction H_1 .

Without any loss of generality and for the sake of simplicity, we assume that the interaction between the nucleons is described only by a two-body force, and neglect 3NF contributions. The generalization of the formalism to include a three-body potential will be considered later.

The solution of Eq. (12) requires the diagonalization of the infinite matrix H , a task that is obviously unfeasible. Then, one has to reduce this huge matrix to a smaller one H_{eff} – defined in a model space made of the only configurations allowed by the valence nucleons within the adopted valence space – by requiring that its eigenvalues belong to the set of the eigenvalues of H . This model space is defined in terms of a subset of eigenvectors of H_0 , $|\Phi_i\rangle$, namely as appropriate combinations of the Slater determinants of Eq. (6), written, in general, in the angular momentum-coupled scheme.

It is worth introducing the projection operators P and $Q = 1 - P$, which project from the complete Hilbert space onto the model space and its complementary space, respectively. The operator P can be expressed by way of the states Φ_i as

$$P = \sum_{i=1}^d |\Phi_i\rangle\langle\Phi_i|, \quad (16)$$

where d is the dimension of the model space. The projection operators P and Q then satisfy the properties

$$P^2 = P, \quad Q^2 = Q, \quad PQ = QP = 0. \quad (17)$$

The aim of the effective SM interaction theory is to reduce the eigenvalue problem of Eq. (12) to a model-space eigenvalue problem

$$H_{\text{eff}}P|\Psi_\alpha\rangle = E_\alpha P|\Psi_\alpha\rangle, \quad (18)$$

where $\alpha = 1, \dots, d$ and H_{eff} is defined only in the model space.

As mentioned in Section 3.1, there are two ways to tackle the problem of deriving H_{eff} , namely by

1. employing a phenomenological approach,
2. starting from bare realistic nuclear forces and then resorting to the many-body theory.

References about the phenomenological approach and some examples of this kind of interactions were given in Section 3.1, while here we discuss in some detail the second way.

Nowadays, novel non-perturbative methods have been developed to derive a effective SM Hamiltonian starting from the bare nuclear interaction, like valence-space in-medium SRG (VS-IMSRG) [132], SM coupled cluster (SMCC) [67], or NCSM with a core [133–136], all of them based on similarity transformations. These non-perturbative approaches are rooted in many-body theory and provide somehow different paths to H_{eff} . However, they can all be derived in a general theoretical framework, that consists in expressing H_{eff} as the result of a similarity transformation acting on the original Hamiltonian

$$H_{\text{eff}} = Pe^{\mathcal{G}}He^{-\mathcal{G}}P, \quad (19)$$

where the transformation is parametrized as the exponential of a generator \mathcal{G} , which needs to satisfy the decoupling condition

$$QH_{\text{eff}}P = 0. \quad (20)$$

An extended and up-to-date presentation of non-perturbative approaches to the derivation of H_{eff} from realistic nuclear interactions can be found in Ref. [37], showing how the different methods can be derived in such a general framework and describing the approximation schemes that have to be employed in each of them.

As mentioned in the Introduction, in the present review we focus on the MBPT approach to H_{eff} , since it is at the moment the one that has been most largely adopted in SM calculations where the role of 3NFs has been investigated.

3.2.1 The perturbative expansion of effective shell-model Hamiltonian

Here, we introduce the formalism of the perturbative derivation of the effective SM Hamiltonian H_{eff} , using the similarity transformation introduced by Lee and Suzuki [34,137]. The starting point is the Schrödinger equation for the A -nucleon system in the whole Hilbert space as defined in Eq.(12).

Then, by following Eqs. (13)-(15), we introduce an auxiliary one-body potential U to break up the nuclear Hamiltonian as the sum of an unperturbed one-body term H_0 , that describes the independent motion of the nucleons, and the residual interaction Hamiltonian H_1 .

The robust energy gap between the shells allows considering as inert the $A - \mathfrak{N}$ core nucleons, which fill the energy orbitals below the Fermi surface. The SP states that are accessible to the \mathfrak{N} valence nucleons are those included in the major shell placed in energy above the closed core, and constitute the valence space. The configurations allowed by the valence nucleons within this valence space define a reduced Hilbert space, the so-called model space, by way of a finite subset of d eigenvectors of H_0 . The operators that project the wave functions from the complete Hilbert space onto the model space and its complementary space are, respectively, P and Q , satisfying the properties of Eq. (17).

As already mentioned before, the goal is to reduce the eigenvalue problem of Eq. (12) to the model-space eigenvalue problem of Eq. (18). Therefore, we need to obtain a new Hamiltonian \mathcal{H} whose eigenvalues are the same of the Hamiltonian H for the A -nucleon system, but satisfying the decoupling equation between the model space P and its complement Q

$$Q\mathcal{H}P = 0, \quad (21)$$

in order to guarantee that the effective Hamiltonian is $H_{\text{eff}} = P\mathcal{H}P$.

Clearly, the Hamiltonian \mathcal{H} has to be obtained by way of a similarity transformation defined in the whole Hilbert space

$$\mathcal{H} = X^{-1}HX. \quad (22)$$

The class of transformation operators X such that \mathcal{H} satisfies the decoupling equation (21) is infinite, and Lee and Suzuki [34,137] have suggested an operator X defined as $X = e^\omega$. Without loss of generality, ω is chosen to satisfy the following properties:

$$\omega = Q\omega P, \quad (23)$$

$$P\omega P = Q\omega Q = P\omega Q = 0, \quad (24)$$

with Eq. (23) implying that

$$\omega^2 = \omega^3 = \dots = 0. \quad (25)$$

The above equation leads us to write the operator X as $X = 1 + \omega$, and, consequently, H_{eff} takes the form

$$H_{\text{eff}} = P\mathcal{H}P = PHP + PHQ\omega, \quad (26)$$

while the decoupling equation (21) can be expressed as

$$QHP + QHQ\omega - \omega PHP - \omega PHQ\omega = 0. \quad (27)$$

This is a non-linear matrix equation and can easily provide a solution for ω as long as the Hamiltonian H is explicitly expressed in the whole Hilbert space. Actually, this is not feasible and some sort of approximations would be necessary.

A successful way to solve Eq. (27) and derive H_{eff} for SM calculations is to introduce a vertex function, the \hat{Q} box, which is suitable for a perturbative expansion. In the following, we make explicit

the \hat{Q} -box approach assuming, for the sake of simplicity, that the unperturbed Hamiltonian H_0 is degenerate for those states belonging to the model space,

$$PH_0P = \epsilon_0 P. \quad (28)$$

This limitation may be overcome by introducing multi-energy \hat{Q} boxes, which are able to account for non-degenerate spaces [35]. Actually, this approach is quite complicated for practical applications, but recently two methods have been introduced, which may be implemented straightforwardly in the derivation of H_{eff} s with eigenstates of H_0 non-degenerate in the model space. The details of these procedures are reported in Refs. [138, 139].

Starting from Eq. (26), the effective interaction $H_1^{\text{eff}} = H_{\text{eff}} - PH_0P$ can be written in terms of ω as

$$H_1^{\text{eff}} = P\mathcal{H}P - PH_0P = PH_1P + PH_1Q\omega, \quad (29)$$

where we have used the diagonality of H_0 in the P and Q states which implies

$$QHP = QH_1P + QH_0P = QH_1P, \quad (30)$$

$$PHQ = PH_1Q + PH_0Q = PH_1Q. \quad (31)$$

Similarly, the decoupling equation (27) takes the form

$$QH_1P + QHQ\omega - \omega(PH_0P + PH_1P + PH_1Q\omega) = QH_1P + QHQ\omega - \omega(\epsilon_0P + H_1^{\text{eff}}) = 0, \quad (32)$$

which leads to a new identity for the operator ω

$$\omega = Q \frac{1}{\epsilon_0 - QHQ} QH_1P - Q \frac{1}{\epsilon_0 - QHQ} \omega H_1^{\text{eff}}. \quad (33)$$

Finally, by inserting Eq. (33) into the identity (29) we obtain a recursive equation for H_1^{eff}

$$H_1^{\text{eff}}(\omega) = PH_1P + PH_1Q \frac{1}{\epsilon_0 - QHQ} QH_1P - PH_1Q \frac{1}{\epsilon_0 - QHQ} \omega H_1^{\text{eff}}(\omega). \quad (34)$$

Then, by defining the \hat{Q} -box vertex function as

$$\hat{Q}(\epsilon) = PH_1P + PH_1Q \frac{1}{\epsilon - QHQ} QH_1P, \quad (35)$$

the recursive equation (34) can be written as

$$H_1^{\text{eff}}(\omega) = \hat{Q}(\epsilon_0) - PH_1Q \frac{1}{\epsilon_0 - QHQ} \omega H_1^{\text{eff}}(\omega). \quad (36)$$

Lee and Suzuki suggested two possible iterative schemes to solve Eq. (36), which are based on the calculation of the \hat{Q} box and its derivatives, known as the Krenciglowa-Kuo (KK) and the Lee-Suzuki (LS) techniques [34].

Let us start from the KK iterative method, which traces back to the coupling of Eqs. (36) and (33), providing the relation

$$H_1^{\text{eff}}(\omega_n) = \sum_{m=0}^{\infty} \left[-PH_1Q \left(\frac{-1}{\epsilon_0 - QHQ} \right)^{m+1} QH_1P \right] [H_1^{\text{eff}}(\omega_{n-1})]^m. \quad (37)$$

The quantity inside the square brackets of Eq. (37), which is commonly dubbed as $\hat{Q}_m(\epsilon_0)$, is proportional to the m -th derivative of the \hat{Q} box calculated in $\epsilon = \epsilon_0$

$$\hat{Q}_m(\epsilon_0) = -PH_1Q \left(\frac{-1}{\epsilon_0 - QHQ} \right)^{m+1} QH_1P = \frac{1}{m!} \left[\frac{d^m \hat{Q}(\epsilon)}{d\epsilon^m} \right]_{\epsilon=\epsilon_0}. \quad (38)$$

We may then rewrite Eq. (37), according to the above identity, as

$$H_1^{\text{eff}}(\omega_n) = \sum_{m=0}^{\infty} \frac{1}{m!} \left[\frac{d^m \hat{Q}(\epsilon)}{d\epsilon^m} \right]_{\epsilon=\epsilon_0} [H_1^{\text{eff}}(\omega_{n-1})]^m = \sum_{m=0}^{\infty} \hat{Q}_m(\epsilon_0) [H_1^{\text{eff}}(\omega_{n-1})]^m. \quad (39)$$

The starting point of the KK iterative method is the assumption $H_1^{\text{eff}}(\omega_0) = \hat{Q}(\epsilon_0)$, leading to rewrite Eq. (39) as

$$H_1^{\text{eff}} = \sum_{i=0}^{\infty} F_i, \quad (40)$$

where

$$\begin{aligned} F_0 &= \hat{Q}(\epsilon_0) \\ F_1 &= \hat{Q}_1(\epsilon_0)\hat{Q}(\epsilon_0) \\ F_2 &= \hat{Q}_2(\epsilon_0)\hat{Q}(\epsilon_0)\hat{Q}(\epsilon_0) + \hat{Q}_1(\epsilon_0)\hat{Q}_1(\epsilon_0)\hat{Q}(\epsilon_0) \\ &\dots \end{aligned} \quad (41)$$

The above expression is a different form of the well-known folded-diagram expansion of the effective Hamiltonian as introduced by Kuo and Krencigłowa, since in Ref. [140] it has been demonstrated the operatorial identity

$$\hat{Q}_1\hat{Q} = -\hat{Q} \int \hat{Q}, \quad (42)$$

where the integral sign corresponds to the so-called folding operation as introduced by Brandow in Ref. [141].

An alternative approach to the solution of Eq. (36) is to resort to the LS technique. This can be carried out by rearranging Eq. (36) in order to obtain an explicit expression of the effective Hamiltonian H_1^{eff} as a function of the operators ω and \hat{Q} [34]

$$H_1^{\text{eff}}(\omega) = \left(1 + PH_1Q \frac{1}{\epsilon_0 - QHQ} \omega \right)^{-1} \hat{Q}(\epsilon_0). \quad (43)$$

The iterative form of this equation is

$$H_1^{\text{eff}}(\omega_n) = \left(1 + PH_1Q \frac{1}{\epsilon_0 - QHQ} \omega_{n-1} \right)^{-1} \hat{Q}(\epsilon_0), \quad (44)$$

while an iterative expression of Eq. (33) is given by

$$\omega_n = Q \frac{1}{\epsilon_0 - QHQ} QH_1P - Q \frac{1}{\epsilon_0 - QHQ} \omega_{n-1} H_1^{\text{eff}}(\omega_n). \quad (45)$$

The starting point of the procedure is to choose $\omega_0 = 0$, so that we may write

$$\begin{aligned} H_1^{\text{eff}}(\omega_1) &= \hat{Q}(\epsilon_0) \\ \omega_1 &= Q \frac{1}{\epsilon_0 - QHQ} QH_1P. \end{aligned}$$

Using some algebra, the following identity can be demonstrated

$$\hat{Q}_1(\epsilon_0) = -PH_1Q \frac{1}{\epsilon_0 - QHQ} Q \frac{1}{\epsilon_0 - QHQ} QH_1P = -PH_1Q \frac{1}{\epsilon_0 - QHQ} \omega_1, \quad (46)$$

and for the iteration step $n = 2$ we have

$$\begin{aligned} H_1^{\text{eff}}(\omega_2) &= \left(1 + PH_1 \frac{1}{\epsilon_0 - QHQ} \omega_1 \right)^{-1} \hat{Q}(\epsilon_0) = \frac{1}{1 - \hat{Q}_1(\epsilon_0)} \hat{Q}(\epsilon_0), \\ \omega_2 &= Q \frac{1}{\epsilon_0 - QHQ} QH_1P - Q \frac{1}{\epsilon_0 - QHQ} \omega_1 H_1^{\text{eff}}(\omega_2). \end{aligned} \quad (47)$$

Finally, the LS iterative expression of H_{eff} is

$$H_1^{\text{eff}}(\omega_n) = \left[1 - \hat{Q}_1(\epsilon_0) \sum_{m=2}^{n-1} \hat{Q}_m(\epsilon_0) \prod_{k=n-m+1}^{n-1} H_1^{\text{eff}}(\omega_k) \right]^{-1} \hat{Q}(\epsilon_0). \quad (48)$$

It is important noting that the KK and LS iterative techniques, even if they have been both conceived to solve the decoupling equation (32), do not provide necessarily the same H_{eff} . Suzuki and Lee have shown that by way of the KK iterative approach one obtains eigenstates that have a large overlap with the model space. On the other side, when H_{eff} is derived by employing the LS technique, its eigenvalues are the lowest in energy among those belonging to the set of the full Hamiltonian H [34].

The heart of the matter is now the calculation of the \hat{Q} -box vertex function defined in Eq. (35). Within a perturbative framework, the term $1/(\epsilon - QHQ)$ appearing in Eq. (35) should be expanded as a power series

$$\frac{1}{\epsilon - QHQ} = \sum_{n=0}^{\infty} \frac{1}{\epsilon - QH_0Q} \left(\frac{QH_1Q}{\epsilon - QH_0Q} \right)^n. \quad (49)$$

It is common to employ a diagrammatic approach of the perturbative expansion by representing the \hat{Q} box as a collection of irreducible Goldstone diagrams – diagrams with at least one line between two successive vertices not belonging to the model space – that have at least one H_1 -vertex and are linked to minimum one external valence line [142].

Usually, the derivation of H_{eff} is performed for systems with one and two valence nucleons. Single valence-nucleon nuclei supplies the one-body component of H_{eff} , H_{eff}^{1b} , namely the theoretical effective SP energies, while the TBMEs are obtained from the effective Hamiltonian for systems with two-valence nucleons, we indicate by H_{eff}^{2b} . In particular, the TBMEs are obtained by way of a subtraction procedure, which consists in removing from H_{eff}^{2b} the diagonal component of H_{eff}^{1b} [143].

In Ref. [144], the topic of the calculation of \hat{Q} -box diagrams in the angular momentum-coupled representation is extensively treated. It should be noted that in literature the effective SM Hamiltonians are derived accounting for \hat{Q} -box diagrams up to at most the third order in perturbation theory, and their complete list is reported in Ref. [145]. This limitation is dictated by the computational cost of performing calculations that include complete higher-order sets of diagrams.

The diagrammatic reported in Refs. [36, 145] is constrained to the derivation of H_{eff} s for one- and two-valence nucleon systems, but many-body diagrams must be included to obtain H_{eff} s for systems with three or more valence nucleons.

At present, few codes can perform the diagonalization of SM Hamiltonians including a three body component, like BIGSTICK [117] and MFDN [119]. They are however mainly oriented to NCSM and limited to light nuclei.

Then, in order to include the contribution of \hat{Q} -box diagrams with at least three incoming and outgoing valence particles in H_{eff} , one can resort to the same approximation used to manage the

input of 3NFs, namely the so-called normal-ordering decomposition of the three-body component of a many-body Hamiltonian [146]. To this end, we start with a \hat{Q} box including second-order three-body diagrams, which, for nuclei with more than two-valence nucleons, account for the interaction via the two-body force of the valence nucleons with core excitations as well as with virtual intermediate nucleons scattered above the valence space (see Fig. 4).

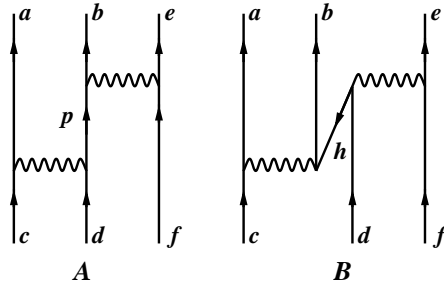


Figure 4: Second-order three-body diagrams. The sum over the intermediate lines runs over particle and hole states outside the valence space, shown by A and B, respectively. For the sake of simplicity, for each topology we report only one of the diagrams which correspond to the permutations of the external lines.

According to the definition of 3NFs introduced in Section 2.1, the contributions reported in Fig. 4 are proper three-body forces, since the intermediate states are orbitals belonging to shells outside the valence space and, consequently, they cannot be constructed by iterating 2NF diagrams with valence-space external lines. The analytical expressions of these diagrams are in Ref. [147].

As discussed in Ref. [37], the main advantage of expressing many-body operators in normal-ordered form is to include as much information as possible from the higher-particle-rank operators into the lower-rank operators. Then, after the normal-ordered decomposition, the approximation consists in neglecting the residual three-body component and, consequently, H_{eff} may be employed in standard SM codes. Such a procedure allows to obtain, starting from the calculation of each (A, B) topology in Fig. 4, nine one-loop diagrams represented by the graph (α) in Fig. 5.

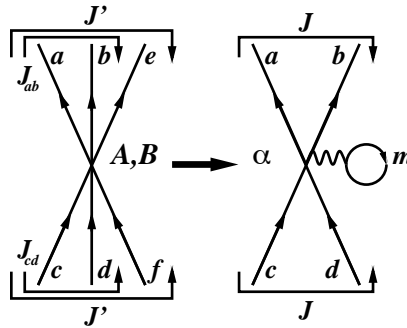


Figure 5: Density-dependent two-body contribution that is obtained from a three-body one. The graph α is obtained by summing over one incoming and outgoing particle of the three-body graphs A, B reported in Fig. 4.

Their explicit form, in terms of the three-body graphs (A, B) , is

$$V_{ab,cd,J}^{\alpha} = \sum_{m,J'} \rho_m \frac{\hat{j}^{\prime 2}}{\hat{j}^2} \langle (a, b), m; J J' | V^{A,B} | (c, d), m; J J' \rangle_A, \quad (50)$$

where the summation over m runs in the valence space, and ρ_m is the unperturbed occupation density of the orbital m according to the number of valence nucleons. The definition of the antisymmetrized but unnormalized three-body states, $|(a, b), c; JJ'\rangle_A$, can be found in Appendix A.

Finally, the perturbative expression of the \hat{Q} box contains one- and two-body diagrams up to third order in V_{NN} , and a density-dependent two-body contribution that includes the effect of three-body diagrams at second-order in V_{NN} [147, 148].

Obviously, this means that a specific effective SM Hamiltonian has to be derived for a given system, depending on the number of valence protons and neutrons, and the obtained set of H_{eff} s differs only in the TBMEs. The role played by density-dependent H_{eff} s in the calculation of g.s. energies in nuclei with many-valence nucleons has been investigated in Refs. [89–91], and discussed in Section 4.2.4.

Now we draw our attention on the calculation of H_{eff} accounting also for the contributions of the 3NF component of a realistic nuclear potential, such as, for example, the N²LO 3N potential reported in Fig. 3. In SM calculations where H_{eff} has been derived perturbatively, this contribution is introduced at first-order in many-body perturbation theory only for the one- and two-valence nucleon systems.

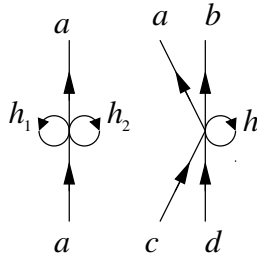


Figure 6: First-order one- and two-body diagrams with a three-body-force vertex. See text for details.

In Fig. 6, both first order one- and two-body diagrams of \hat{Q} box from a 3N potential are shown, and their explicit expressions are

$$\epsilon_a^{(3\text{NF})} = \sum_{\substack{h_1, h_2 \\ J_{12} J}} \frac{\hat{j}^2}{2\hat{j}_a} \langle (h_1, h_2), a; J_{12} J | V_{3N} | (h_1, h_2), a; J_{12} J \rangle_A, \quad (51)$$

$$V_{ab, cd, J}^{(3\text{NF})} = \sum_{h, J'} \frac{\hat{j}'^2}{\hat{j}^2} \langle (a, b), h; J J' | V_{3N} | (c, d), h; J J' \rangle_A, \quad (52)$$

where the indices h refer to core states, while the three-body matrix element on the right hand side of both equations, expressed within the proton-neutron formalism, is antisymmetrized but not normalized, and its explicit form is given, for example, by Eq. (110).

The three-body component of a many-body Hamiltonian is therefore written in terms of one- and two-body pieces, which correspond, respectively, to interactions among one-valence and two-core nucleons, or two-valence and one-core nucleon, with coefficients given by the expressions in Eqs. (51) and (52). It is worth noting that these two pieces arise from the normal-ordering two-body decomposition of the 3NF with respect to the core as reference state. This means that the 3NF among valence nucleons is neglected, which may lead to underestimation of the 3NF repulsion and to overbinding that acquire more relevance with an increasing number of valence particles, as pointed out in Refs. [37, 69]. In Ref. [69], an ensemble or mixed-state reference was introduced to account for these interactions in an approximate way within the VS-IMSRG framework, which it is shown to cure this deficiency. In this connection, it will be certainly relevant to investigate the relative importance of the missing 3NF contributions in our approach. However, we would mention here, as discussed in detail in section 4.1,

that of our SM results for p shell nuclei obtained by using an $NN + 3N$ potential are in close agreement with those of NCSM. In particular, we are able to reproduce the experimental sequence of observed states in ^{10}B , as it is done by NCSM calculations. The agreement between the results of the SM and NCSM models including 3NFs is on the overall of the same quality of that obtained when using the NN force only. Larger discrepancies are found only for energies of high excited states, which may be related to our approximation in the 3NF treatment.

In concluding this section, it may be useful to give a summary of the diagrams we include in the derivation of our SM effective Hamiltonians. We arrest the \hat{Q} -box expansion to the one- and two-body Goldstone diagrams at third order in the NN potential, which are explicitly shown in the Appendices of Ref. [145], while we consider only diagrams at first order in the 3N force whose expressions are given in Eqs. 51 and 52. In addition, to account for the progressive filling of the valence space in systems with more than two-valence particles we include the density-dependent two-body contributions of Eq. 50 arising from the second-order three-body diagrams of Fig. 4.

3.2.2 *The perturbative expansion of effective shell-model decay operators*

Besides the calculation of energy spectra, SM wave functions may provide also the matrix elements of operators Θ which are related to physical observables, such as electromagnetic transition rates, multipole moments, etc.

As it has been previously pointed out, the wave functions $|\psi_\alpha\rangle$ obtained diagonalizing H_{eff} are not the true ones $|\Psi_\alpha\rangle$, but their projections onto the model space ($|\psi_\alpha\rangle = P|\Psi_\alpha\rangle$). Then, it is necessary to renormalize Θ in order to account for the neglected degrees of freedom belonging to configurations outside the model space. Formally, an effective operator Θ_{eff} has to be derived, such that

$$\langle \tilde{\Psi}_\alpha | \Theta | \Psi_\beta \rangle = \langle \tilde{\psi}_\alpha | \Theta_{\text{eff}} | \psi_\beta \rangle. \quad (53)$$

The perturbative expansion of effective operators has been approached in the early attempts to employ realistic potentials for SM calculations by L. Zamick for the problematics of electromagnetic transitions [149–151] and by I. S. Towner for the study of the quenching of spin-dependent decay-operator matrix elements [152, 153].

A formally improved structure to the derivation of non-Hermitian effective operators has been elaborated by Suzuki and Okamoto in Ref. [154], where they have introduced an expansion formula for the effective operators in terms of a vertex function $\hat{\Theta}$ box that, analogously to the \hat{Q} box in the effective Hamiltonian theory, is the building block for constructing effective operators.

We outline now some details about this procedure. According to Eq. (26) and keeping in mind that $\omega \equiv Q\omega P$, H_{eff} may be written as

$$H_{\text{eff}} = PH(P + \omega), \quad (54)$$

so that the true eigenstates $|\Psi_\alpha\rangle$ and their orthonormal counterparts $\langle \tilde{\Psi}_\alpha |$ are given by

$$|\Psi_\alpha\rangle = (P + \omega)|\psi_\alpha\rangle \quad , \quad \langle \tilde{\Psi}_\alpha | = \langle \tilde{\psi}_\alpha | (P + \omega^\dagger \omega)(P + \omega^\dagger). \quad (55)$$

Actually, a general effective operator expression in the bra-ket representation is written as

$$\Theta_{\text{eff}} = \sum_{\alpha\beta} |\psi_\alpha\rangle \langle \tilde{\Psi}_\alpha | \Theta | \Psi_\beta \rangle \langle \tilde{\psi}_\beta |, \quad (56)$$

where Θ is a given time-independent Hermitian operator. Then, Θ_{eff} in an operator form is

$$\Theta_{\text{eff}} = (P + \omega^\dagger \omega)^{-1} (P + \omega^\dagger) \Theta (P + \omega). \quad (57)$$

It is worth noting that Eq. (53) holds whatever it is the normalization of $|\Psi_\alpha\rangle$ and $|\psi_\alpha\rangle$, but if the true eigenvectors are normalized, then $\langle\tilde{\Psi}_\alpha| = \langle\Psi_\alpha|$ and $|\psi_\alpha\rangle$ should be normalized as

$$\langle\tilde{\psi}_\alpha|(P + \omega^\dagger\omega)|\psi_\alpha\rangle = 1. \quad (58)$$

To calculate Θ_{eff} , it is convenient to introduce the vertex function $\hat{\Theta}$ box, which is defined as

$$\hat{\Theta} = (P + \omega^\dagger)\Theta(P + \omega), \quad (59)$$

in order to factorize Θ_{eff} as follows

$$\Theta_{\text{eff}} = (P + \omega^\dagger\omega)^{-1}\hat{\Theta}. \quad (60)$$

Therefore, to derive Θ_{eff} one needs to calculate both $\hat{\Theta}$ and $\omega^\dagger\omega$. Let us tackle the first issue: according to Eq. (59) and to the following expression of ω in terms of H_{eff}

$$\omega = \sum_{n=0}^{\infty} (-1)^n \left(\frac{1}{\epsilon_0 - QHQ} \right)^{n+1} QH_1P(H_1^{\text{eff}})^n, \quad (61)$$

the following relation can be written for $\hat{\Theta}$

$$\hat{\Theta} = \hat{\Theta}_{PP} + (\hat{\Theta}_{PQ} + h.c.) + \hat{\Theta}_{QQ}, \quad (62)$$

where

$$\hat{\Theta}_{PP} = P\Theta P, \quad (63)$$

$$\hat{\Theta}_{PQ} = P\Theta\omega P = \sum_{n=0}^{\infty} \hat{\Theta}_n(H_1^{\text{eff}})^n, \quad (64)$$

$$\hat{\Theta}_{QQ} = P\omega^\dagger\Theta\omega P = \sum_{n,m=0}^{\infty} (H_1^{\text{eff}})^n \hat{\Theta}_{nm} (H_1^{\text{eff}})^m, \quad (65)$$

and $\hat{\Theta}_m, \hat{\Theta}_{mn}$ are defined as

$$\hat{\Theta}_m = \frac{1}{m!} \left. \frac{d^m \hat{\Theta}(\epsilon)}{d\epsilon^m} \right|_{\epsilon=\epsilon_0}, \quad (66)$$

$$\hat{\Theta}_{mn} = \frac{1}{m!n!} \left. \frac{d^m}{d\epsilon_1^m} \frac{d^n}{d\epsilon_2^n} \hat{\Theta}(\epsilon_1; \epsilon_2) \right|_{\epsilon_1=\epsilon_0, \epsilon_2=\epsilon_0}, \quad (67)$$

with

$$\hat{\Theta}(\epsilon) = P\Theta P + P\Theta Q \frac{1}{\epsilon - QHQ} QH_1P, \quad (68)$$

$$\hat{\Theta}(\epsilon_1; \epsilon_2) = PH_1Q \frac{1}{\epsilon_1 - QHQ} Q\Theta Q \frac{1}{\epsilon_2 - QHQ} QH_1P. \quad (69)$$

By way of definition (38), the product $\omega^\dagger\omega$ takes the form

$$\omega^\dagger\omega = - \sum_{n=1}^{\infty} \sum_{m=1}^{\infty} ((H_1^{\text{eff}})^\dagger)^{n-1} \hat{Q}(\epsilon_0)_{n+m-1} (H_1^{\text{eff}})^{m-1}. \quad (70)$$

Using now the expression of H_1^{eff} in terms of the \hat{Q} box and its derivatives – Eqs. (40) and (41) – the above quantity may be rewritten as

$$\omega^\dagger\omega = -\hat{Q}_1 + (\hat{Q}_2\hat{Q} + h.c.) + (\hat{Q}_3\hat{Q}\hat{Q} + h.c.) + (\hat{Q}_2\hat{Q}_1\hat{Q} + h.c.) + \dots \quad (71)$$

Melting together Eqs. (68) and (71), the final perturbative expansion form of the effective operator Θ_{eff} is

$$\Theta_{\text{eff}} = (P + \hat{Q}_1 + \hat{Q}_1\hat{Q}_1 + \hat{Q}_2\hat{Q}_1 + \hat{Q}_2\hat{Q}_2 + \dots) \times (\chi_0 + \chi_1 + \chi_2 + \dots), \quad (72)$$

where

$$\chi_0 = (\hat{\Theta}_0 + h.c.) + \hat{\Theta}_{00}, \quad (73)$$

$$\chi_1 = (\hat{\Theta}_1\hat{Q} + h.c.) + (\hat{\Theta}_{01}\hat{Q} + h.c.), \quad (74)$$

$$\chi_2 = (\hat{\Theta}_1\hat{Q}_1\hat{Q} + h.c.) + (\hat{\Theta}_2\hat{Q}\hat{Q} + h.c.) + (\hat{\Theta}_{02}\hat{Q}\hat{Q} + h.c.) + \hat{Q}\hat{\Theta}_{11}\hat{Q}. \quad (75)$$

...

It is worth to evidence the link existing between H_{eff} , derived in terms of the \hat{Q} box, and any effective operator. This is achieved by inserting the identity $\hat{Q}\hat{Q}^{-1} = \mathbf{1}$ in Eq. (72), and consequently obtaining the following expression:

$$\begin{aligned} \Theta_{\text{eff}} &= (P + \hat{Q}_1 + \hat{Q}_1\hat{Q}_1 + \hat{Q}_2\hat{Q}_1 + \hat{Q}_2\hat{Q}_2 + \dots)\hat{Q}\hat{Q}^{-1} \times (\chi_0 + \chi_1 + \chi_2 + \dots) \\ &= H_{\text{eff}}\hat{Q}^{-1}(\chi_0 + \chi_1 + \chi_2 + \dots). \end{aligned} \quad (76)$$

The χ_n series must be arrested to a finite order, and the starting point is the derivation of a perturbative expansion of $\hat{\Theta}_0 \equiv \hat{\Theta}(\epsilon_0)$ and $\hat{\Theta}_{00} \equiv \hat{\Theta}(\epsilon_0; \epsilon_0)$, including diagrams up to a finite order in the perturbation theory, consistently with the \hat{Q} -box expansion. The issue of the convergence of the χ_n series and of the perturbative expansion of $\hat{\Theta}_0$ and $\hat{\Theta}_{00}$ has been investigated in Refs. [155–157], and in Ref. [38], which report details about the calculation of the diagrams appearing in the $\hat{\Theta}_0$ expansion for a one-body operator Θ .

3.3 Gamow shell model with three-body forces

As the number of protons or neutrons in the nucleus increases to the existence limit of the dripline, exotic phenomena such as halo and resonances can emerge. With extreme proton-neutron imbalance, the nuclei around the dripline are weakly bound or unbound. They belong to open quantum systems in which the coupling to the continuum can be significant and should be properly treated. Due to the large spatial distributions of wave functions in resonance and continuum states, using a standard spatially-localized HO basis would not be a good option. In the past two decades, several methods have been developed to overcome this challenge. The conventional SM has been extended to include the continuum effect, e.g., SM embedded in the continuum [158–161] and the continuum-coupled SM [162].

An elegant treatment of the continuum coupling is to use the Berggren representation [163] in which the one-body Schrödinger equation is generalized to a complex-momentum (complex- k) plane. This creates naturally bound, resonance and continuum single-particle states on an equal footing, see Fig. 7. The many-body Hamiltonian can be expressed in the Berggren basis, and tackled by many-body methods in the complex- k space. The SM has been successfully extended to the complex- k Berggren basis, leading to the so-called GSM, in which the continuum effect is included at the basis level. In the first GSM applications to atomic nuclei, phenomenological interactions were used with the potential parameters determined by fitting nuclear structure data [82, 164–169]. Soon, the GSM was developed with realistic nuclear interactions [170–175]. Meanwhile, the Berggren technique was also used in CC [176–178] and IMSRG approaches [179].

Along with the continuum coupling, 3NFs also play an important role in the descriptions of exotic nuclei. In Refs. [92–94], the realistic GSM was extended with 3NFs considered. The inclusions of both the continuum coupling and 3NFs can give a better quantitative description of exotic nuclei [92]. With 3NFs included, two steps of development towards a full self-consistent *ab initio* GSM have been

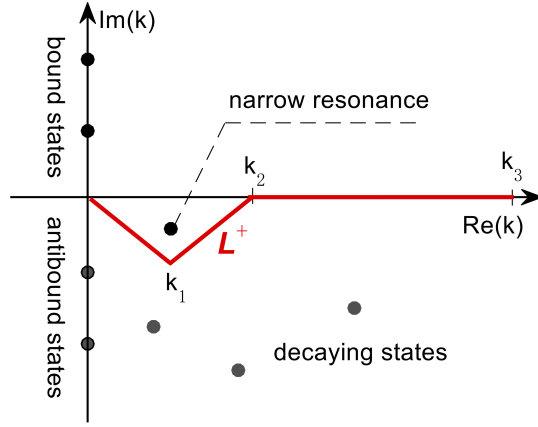


Figure 7: Schematic Berggren complex- k plane. The bound, resonant and scattering states construct the Berggren completeness relation. The contour L^+ has to be chosen in such a way that all the discrete narrow resonant states are contained in the domain between L^+ and the real- k axis [173].

made: i) the WS potential has been used to generate the complex- k Berggren basis, and the many-body GSM with realistic 2NFs and 3NFs has been performed in the WS basis [92, 93], whose WS parameters have been determined by fitting data; ii) for a more self-consistent calculation, the Berggren basis has been created starting from realistic interaction itself using the complex- k Gamow Hartree-Fock (GHF) method, and the complex GSM has been performed in the GHF basis. The 3NF has been included in both the GHF and GSM calculations, as done in Ref. [94].

Similar to standard SM calculations, an auxiliary one-body potential U is usually introduced into the Hamiltonian to obtain a one-body term H_0 describing the independent motions of the nucleons and a residual interaction H_1 . However, here we rewrite the Hamiltonian (13) to include the 3NF and remove the center of mass kinetic energy thus obtaining an intrinsic transitionally invariant Hamiltonian,

$$\begin{aligned}
 H &= \sum_{i<j} \frac{(\mathbf{p}_i - \mathbf{p}_j)^2}{2mA} + \hat{V}_{\text{NN}} + \hat{V}_{\text{3N}} \\
 &= \left[\sum_{i=1}^A \left(\frac{p_i^2}{2m} + U_i \right) \right] + \left[\sum_{i<j}^A \left(V_{\text{NN}}^{(ij)} - \frac{\mathbf{p}_i \cdot \mathbf{p}_j}{mA} \right) - \sum_{i=1}^A \left(U_i + \frac{p_i^2}{2mA} \right) + \sum_{i<j<k}^A V_{\text{3N}}^{(ijk)} \right] \\
 &= H_0 + H_1,
 \end{aligned} \tag{77}$$

To generate the Berggren basis, U is usually taken as the WS potential produced by the core for the GSM calculation with a core [92, 93]. The radial wave functions of the Berggren SP states are obtained by solving the SP Schrödinger equation in the complex- k space with the WS potential U . The Berggren SP states form a complete set of basis states with discrete bound, resonant and continuum scattering states, as shown in Fig. 7. Due to the complexity and computational task of many-body calculations with full 3NF, as discussed in the Introduction and in Section 3.2.1, we adopt the normal-ordering approximation with neglecting the residual three-body term [24, 86, 89, 92, 93]. The normal-ordered zero-body and one-body terms are absorbed into the core Hamiltonian which generates the Berggren basis, while the final GSM Hamiltonian has a two-body form but with normal-ordered two-body term of the 3NF included (see Eq.(52)). With the overlap method of wave functions [173, 180], the Hamiltonian can be transferred to the complex- k Berggren basis.

With the Hamiltonian matrix elements given in the Berggren basis, the \hat{Q} -box folded-diagram method is used to construct the realistic complex effective interaction for a chosen model space. In

general, such kind of model space should include relevant bound, resonant and continuum states. Therefore, the basis states are certainly not degenerate, and we exploit an extension of the Kuo-Krenciglowa (EKK) method [181] to the complex- k space to build the effective GSM interaction. At last, the complex-symmetry GSM Hamiltonian is diagonalized in the model space using the Jacobi-Davidson method [182].

Although the Hamiltonian is intrinsic, the GSM wavefunction is not factorized into the center-of-mass (CoM) and intrinsic parts. This means that the effect from the CoM motion has not been removed exactly. In the HO basis, the CoM effect can be treated using the Lawson method [183]. In principle, one can generalize the Lawson method, for example, in the real-energy CC [184] and IMSRG [185] calculations which adopted the Hartree-Fock basis. Unfortunately, the generalization is not valid in the complex-energy Berggren basis due to the fact that the R^2 matrix elements (R is the CoM position) cannot be regularized in resonance and continuum states, which are not square integrable in fact. However, we have well discussed in the previous works [173, 174, 179] that the CoM effect is not significant in low-lying states.

4 Applications and comparison with experiment

In this section, we shall review recent results of SM calculations based on effective Hamiltonians derived from realistic two- and three-body potentials. The aim of the presentation is essentially to highlight the role of 3NFs in explaining phenomena such as the location of the neutron dripline in isotopic chains and the shell evolution as a function of the number of valence nucleons, as well as to investigate the combined effects of 3NFs and the coupling with continuum for the description of unbound nuclei and unbound resonance states in the vicinity of the dripline or of the Borromean structure of halo nuclei. We shall focus on systems ranging from the very light-mass p -shell nuclei to those with intermediate mass belonging to the fp shell.

In the subsection devoted to p -shell nuclei, we have found it useful to evidence the validity of our perturbative approach in deriving the effective SM Hamiltonian. To this end, in the first part we illustrate the convergence properties of the \hat{Q} -box vertex function as concerns the truncation of the intermediate-state space, the order-by-order convergence, and the dependence on the HO parameter. The analyses is based on an NN potential since as concerns 3NFs only first-order contributions of the normal-ordered one- and two-body parts are taken into account. Then, once shown how the introduced approximations can be taken under control, we compare our SM results arising from the chiral NN -only and $NN+3N$ forces with the corresponding ones obtained by the *ab initio* NCSM.

4.1 Benchmark calculations in the $0p$ -shell region

Benchmark calculations are very important to test methods as well as computational approaches. More specifically, they may be helpful to understand to what extent a many-body method is working and to estimate the impact of the necessary truncations and approximations that have been introduced. In Ref. [145], an extensive study has been carried out to compare the results of SM calculations for p -shell nuclei obtained by using an effective Hamiltonian derived from an NN chiral potential at N³LO [16, 55] with those obtained with the *ab initio* NCSM [18, 87, 88, 186]. In Ref. [86], this investigation has been extended by including in the derivation of H_{eff} for p -shell nuclei the one- and two-body components of a normal-ordered 3N chiral potential at N²LO.

The work in Ref. [145] has also tried to assess the behavior of the perturbative expansion of H_{eff} with respect to the dimension of the intermediate state space and the order-by-order convergence, when starting from chiral potentials. As regards this aspect, we recall that the Q space appearing in Eq. (35) is the complement of the model space in the whole Hilbert space, therefore it is composed by an infinite

number of configurations. It is clearly unfeasible to employ an infinite Q space, and consequently the perturbative expansion of the \hat{Q} box implies a truncation of the space of the intermediate states, which belong to the Q space by definition. The common procedure is to employ an energy truncation, which consists in including only those intermediate states whose unperturbed excitation energy is smaller than a fixed value E_{\max} expressed in terms of the number of oscillator quanta N_{\max} , namely as an integer multiple of the HO parameter $\hbar\omega$

$$E_{\max} = N_{\max}\hbar\omega.$$

In Ref. [145] the theoretical energies of the yrast states in ${}^6\text{Li}$, corresponding to the absolute energy values relative to ${}^4\text{He}$, have been calculated as a function of E_{\max} (see Fig. 8), using an effective Hamiltonian derived from the N^3LO NN potential and including in the \hat{Q} -box diagrams up to the second order in H_1 .

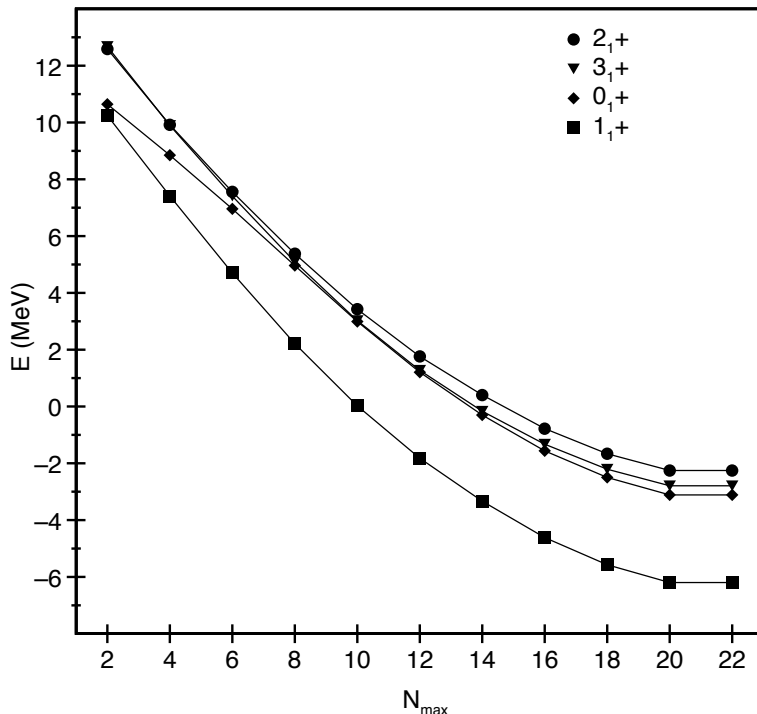


Figure 8: Theoretical energies of ${}^6\text{Li}$ yrast states relative to ${}^4\text{He}$, obtained with the N^3LO NN potential, as a function of N_{\max} [145].

As can be seen in Fig. 8, the convergence is reached when intermediate states at least up to $E_{\max} = 20 \hbar\omega$, with $\hbar\omega = 19$ MeV, are included. This value of the HO parameter is close to the one provided by the expression [187] $\hbar\omega = 45A^{-1/3} - 25A^{-2/3}$ for $A = 4$. This is no surprise if we consider that the NN potential is characterized (in momentum-space representation) by a certain cutoff momentum Λ , which is also the maximum relative momentum of the two-nucleon system. Consequently, the maximum value of the energy corresponding to the relative motion of two nucleons is

$$E_{\max} = \frac{\hbar^2\Lambda^2}{M}, \quad (78)$$

where M is the nucleon mass. This relation may be rewritten in terms of N_{\max} and $\hbar\omega$,

$$N_{\max}\hbar\omega = \frac{\hbar^2\Lambda^2}{M}. \quad (79)$$

Equation (79) constrains the value of N_{\max} for a chosen HO parameter and depends on the cutoff Λ of the NN potential. The chiral $N^3\text{LO}$ potential under consideration is characterized by a cutoff $\Lambda = 2.5, 2.6 \text{ fm}^{-1}$ [16, 55], and, therefore, if $\hbar\omega = 19 \text{ MeV}$, one should include in the \hat{Q} -box expansion the contributions of the Q -space configurations at least up to $N_{\max} = 16$. It is worth pointing out that the $N^3\text{LO}$ potential is multiplied by a smooth regulator function with a gaussian shape [188]. This characteristic slows down the convergence behavior of the NN potential and justifies the need to include a larger number of Q -space configurations.

Actually, in Ref. [145] the convergence with respect to the number of intermediate states has been studied also considering an NN potential with a sharp cutoff as regulator function, a chiral potential dubbed $N^3\text{LOW}$ [189]. This potential, whose cutoff is $\Lambda = 2.1 \text{ fm}^{-1}$, is characterized by a faster convergence, and the convergence is reached at $N_{\max} = 10$, which is consistent with the relationship (79) for $\hbar\omega = 19 \text{ MeV}$.

Another important aspect to be studied is the order-by-order convergence properties of the H_{eff} expansion, namely the dependence of SM results on the order at which the perturbative expansion of the \hat{Q} box is arrested. It is worth mentioning that this relevant topic has been first investigated by Barrett and Kirson in the pioneering period of the perturbative expansion of H_{eff} [190], and it has been reprised in Ref. [145] within the \hat{Q} -box approach, using \hat{Q} boxes at second ($H_{2\text{nd}}^{\text{eff}}$) and third ($H_{3\text{rd}}^{\text{eff}}$) order in perturbation theory. Moreover, in order to estimate the value to which the perturbative series may converge, H_{eff} has been derived by calculating the Padé approximant [2|1] [191, 192] of the \hat{Q} box ($H_{\text{Padé}}^{\text{eff}}$).

In Fig. 9 the energies of ${}^6\text{Li}$ yrast states with respect to ${}^4\text{He}$, obtained with the $N^3\text{LO}$ NN potential, are reported as calculated with $H_{1\text{st}}^{\text{eff}}$, $H_{2\text{nd}}^{\text{eff}}$, $H_{3\text{rd}}^{\text{eff}}$, and $H_{\text{Padé}}^{\text{eff}}$, $H_{1\text{st}}^{\text{eff}}$ representing the one-body first-order \hat{Q} -box diagrams plus the NN bare potential.

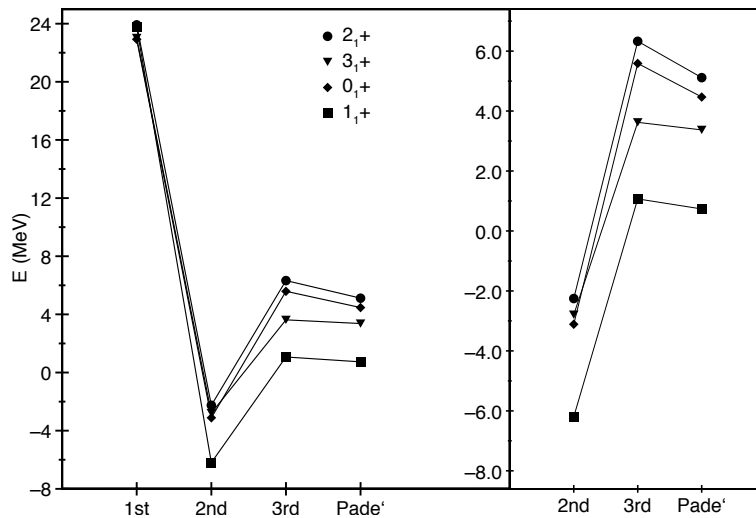


Figure 9: Theoretical energies of ${}^6\text{Li}$ yrast states relative to ${}^4\text{He}$, obtained with $H_{1\text{st}}^{\text{eff}}$, $H_{2\text{nd}}^{\text{eff}}$, $H_{3\text{rd}}^{\text{eff}}$, and $H_{\text{Padé}}^{\text{eff}}$ derived from the $N^3\text{LO}$ NN potential (see text for details). In the right side of the figure, where an expanded scale is adopted, the $H_{1\text{st}}^{\text{eff}}$ results are omitted [145].

There are a couple of aspects that should be evidenced from the inspection of Fig. 9:

1. the large gap between the results at first order in perturbation theory and those at higher orders shows that the employment of a bare NN potential in SM calculations, without any renormalization due to long-range correlations, leads to a poor description of the physics of atomic nuclei;

2. the results for ${}^6\text{Li}$ obtained with $H_{3\text{rd}}^{\text{eff}}$ are very close to those with $H_{\text{Pad}\acute{e}}^{\text{eff}}$, and this supports the hypothesis that SM calculations may have a weak dependence on higher-order \hat{Q} -box perturbative terms.

On the above grounds, in all subsequent SM calculations the effective Hamiltonians have been derived by calculating the Pad\`e approximant [2|1] of the \hat{Q} box.

Finally, it is worth to examine another aspect that has been evidenced in Ref. [145]. We recall that, because of Eqs. (13-15), there could be a dependence of H_{eff} on the choice of the auxiliary potential U introduced to construct the SP basis employed to expand the matrix elements of the input interaction. More precisely, since we choose the HO basis, the results of the SM calculations may depend on the choice of the HO parameter $\hbar\omega$. This is due to the approximations inherent our calculations, namely, as discussed above, to the truncation of the space of intermediate states and of the perturbative expansion of the \hat{Q} -box at a certain order.

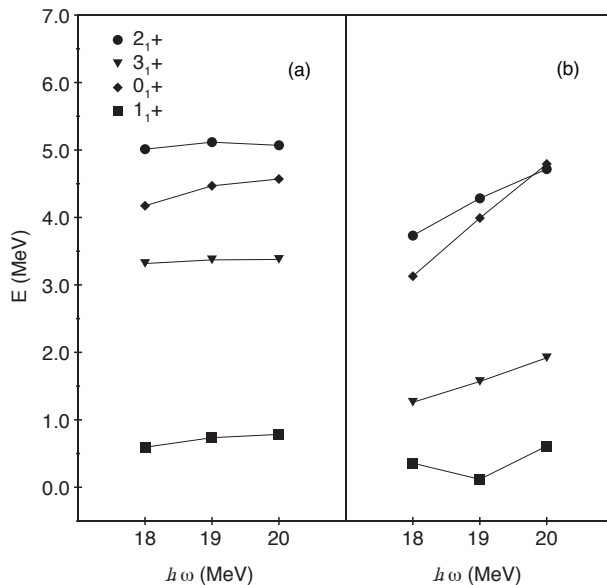


Figure 10: Theoretical energies of ${}^6\text{Li}$ yrast states relative to ${}^4\text{He}$, obtained with the N^3LO NN potential, as a function of $\hbar\omega$ [145]. See text for details.

In Fig. 10, the theoretical energies of the yrast states in ${}^6\text{Li}$ are reported as a function of $\hbar\omega$ for three effective Hamiltonians derived from the N^3LO potential by using as HO parameter $\hbar\omega = 18, 19,$ and 20 MeV. The panel (a) of Fig. 10 refers to effective Hamiltonians derived including all third-order diagrams in the \hat{Q} box, and then calculating its Pad\`e approximant [2|1]. On the other hand, the spectra in panel (b) are obtained by retaining in the \hat{Q} box only the first-order ($V-U$)-insertion diagram (see Fig. 1 in Ref. [145]) and neglecting higher-order terms of the same class of diagrams, and again calculating its Pad\`e approximant [2|1]. These results show very clearly that ($V-U$)-insertion diagrams play a crucial role to reduce the dependence on the HO parameter.

Once a complete survey of all possible sources of approximations induced by the perturbative expansion has been completed, a comparison of the SM results with those provided by the *ab initio* NCSM can be performed [18, 186].

Actually, it should be pointed out that the results reported in Fig. 8-10 have been obtained starting from the A -body Hamiltonian of Eqs. (13)-(15), which is not translationally invariant, while NCSM calculations employ a purely intrinsic Hamiltonian. Therefore, to compare our SM results with the NCSM ones we have to remove the center of mass kinetic energy from Eqs.(13)-(15), namely we have to use the Hamiltonian defined in Eq. (77).

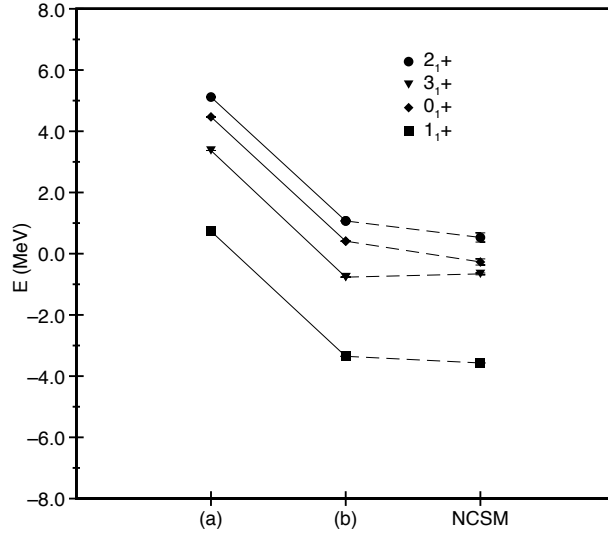


Figure 11: Theoretical energies of ${}^6\text{Li}$ yrast states relative to ${}^4\text{He}$, obtained with N^3LO NN potential. (a) SM calculation with an effective intrinsic plus center of mass Hamiltonian. (b) SM calculation with an effective intrinsic Hamiltonian. (c) NCSM calculation [145].

The calculated energies of the yrast states in ${}^6\text{Li}$ relative to ${}^4\text{He}$ are reported in Fig. 11; the results labelled with (a) refer to a SM calculation with an effective Hamiltonian derived from Eqs. (13)-(15), the spectrum (b) corresponds to an effective Hamiltonian derived from the translationally invariant Hamiltonian of Eq. (77) retaining only the NN component. The NCSM spectrum (c) is obtained considering the calculated binding energy of ${}^6\text{Li}$ in Ref. [87] with respect to the ${}^4\text{He}$ ground state energy [18], and the ${}^6\text{Li}$ excitation energies reported in Ref. [186]. The results in Fig. 11 evidence how relevant is to employ a purely intrinsic Hamiltonian to compare correctly the ground-state energies of SM and NCSM. This choice of the Hamiltonian does not affect, however, the energy spacings, and it should be noted that the difference between the not translationally invariant and intrinsic Hamiltonians rapidly decreases with growing A .

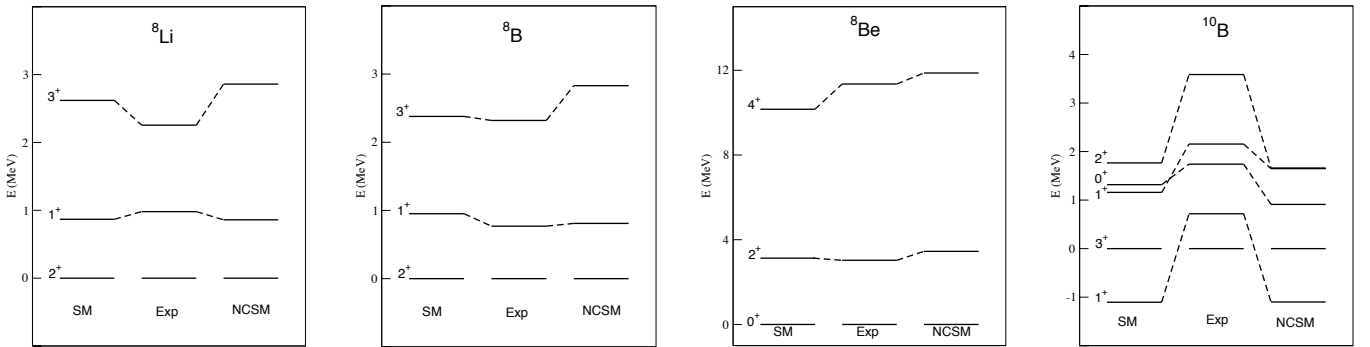


Figure 12: Theoretical and experimental spectra for ${}^8\text{Li}$, ${}^8\text{B}$, ${}^8\text{Be}$, and ${}^{10}\text{B}$. The theoretical energies have been obtained using the N^3LO NN potential within SM and NCSM calculations. Figure adapted from Ref. [86].

Moreover, we can conclude that the agreement between the SM and NCSM results for ${}^6\text{Li}$, which is a two-valence nucleon system with respect to ${}^4\text{He}$ core, is quite good. This conclusion may be extended also to calculations of nuclei with a number of valence nucleons larger than two.

In Figs. 12 and 13 the low-energy excitation spectra of ${}^8\text{Li}$, ${}^8\text{B}$, ${}^8\text{Be}$, ${}^{10}\text{B}$, ${}^{11}\text{B}$, ${}^{12}\text{C}$, and ${}^{13}\text{C}$, calculated with SM [86] and NCSM [87,88] are reported and compared with experiment [193]. From the inspection of these two figures we see that, as regards the excitation spectra of many-valence nucleon systems, the comparison between SM calculations with H_{eff} derived within the perturbative approach and *ab initio* calculations is quite satisfactory.

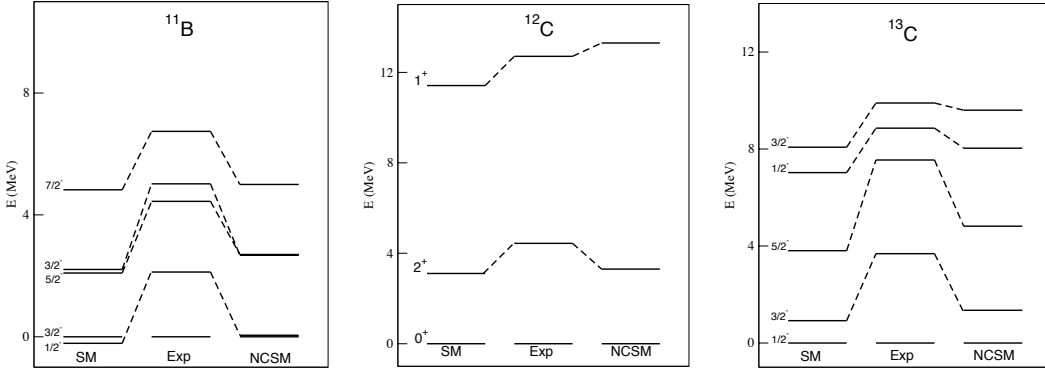


Figure 13: Same as in Fig. 12, but for ${}^{11}\text{B}$, ${}^{12}\text{C}$, and ${}^{13}\text{C}$. Figure adapted from [86].

In Fig. 14 (a), the ground-state energies, relative to ${}^4\text{He}$, for the $N = Z$ nuclei with mass $6 \leq A \leq 12$ calculated within the SM (dot-dashed line) [145] are compared with those of NCSM calculations (dotted line) and the experimental ones (continuous line) [194].

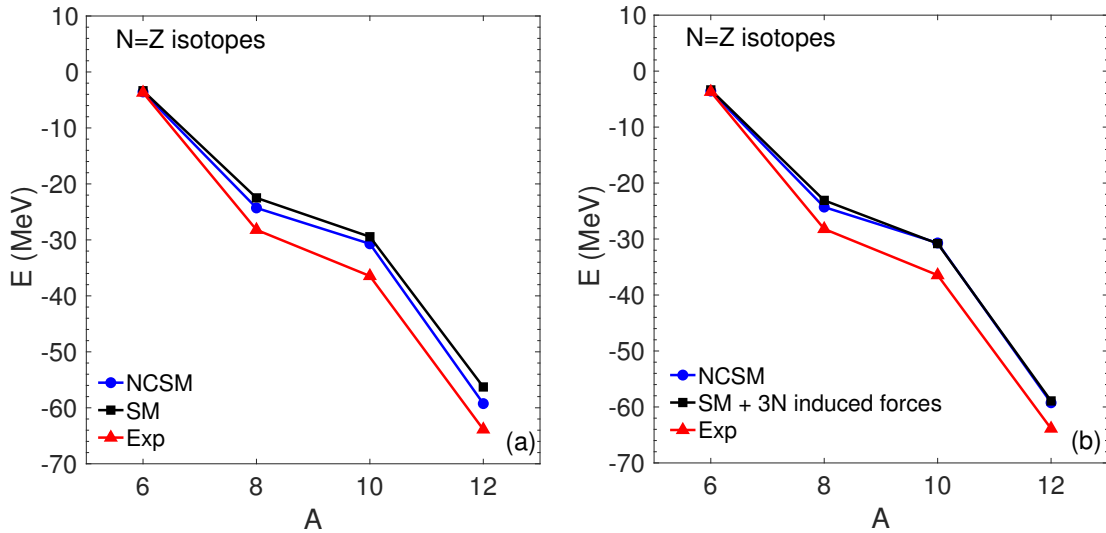


Figure 14: Experimental ground-state energies for $N = Z$ nuclei with mass $6 \leq A \leq 12$ are compared with theoretical values obtained using the $N^3\text{LO}$ NN potential within the NCSM and SM. SM results refer to calculations (a) without and (b) with contributions from 3N induced forces [86,145].

We see that discrepancies between SM and NCSM results increase with the number of valence nucleons, and this may be ascribed to the fact that many-body (> 2) components of H_{eff} have not been taken into account.

As mentioned in Section 3.2.1, for nuclei with a number of valence nucleons larger than two, the \hat{Q} box should contain diagrams with at least three incoming and outgoing valence particles, as for

example the second-order three-body diagrams in Fig. 4. In order to include the effects of these contributions, in Ref. [86] the monopole component of the diagrams in Fig. 4 has been calculated and added to the theoretical g.s. energies. The results of this procedure are reported in Fig. 14 (b), where the new calculated SM g.s. energies (black squares) are compared with both the experimental ones (red triangles) and those obtained with NCSM (blue bullets) [86]. As it can be seen, the comparison between SM and NCSM has been efficiently improved with respect to that of Fig. 14 (a), the largest discrepancy being about 4% for ${}^8\text{Be}$.

So far, we have shown that the derivation of H_{eff} via a perturbative expansion of the \hat{Q} -box vertex function provides SM results that are in a satisfactory agreement with those of the *ab initio* method NCSM, when accounting for realistic NN potential only. In Ref. [86] a step forward has been made by including in the derivation of H_{eff} contributions from a chiral 3NF [18].

It is worth recalling that in the chiral perturbative expansion the 3N potentials appear from $N^2\text{LO}$ on, and at this order the 3N potential consists of three components (see Fig. 3), which are the 2PE, the 1PE, and the contact terms. The adopted intrinsic Hamiltonian is defined in Eq. (77).

As reported in Section 2.2, a great advantage of ChPT is that it generates nuclear two- and many-body forces on an equal footing [14–16], namely most interaction vertices that appear in the 3NF also occur in the NN potential. The parameters carried by these vertices are fixed in the construction of the chiral 2NF, and for the $N^2\text{LO}$ 3N potential they are the LECs c_1 , c_3 , and c_4 , appearing in $v_{3N}^{(2\pi)}$. However, the 3N 1PE term and the contact interaction are characterized by two extra LECs (known as c_D and c_E), which cannot be constrained by two-body observables, and should be fitted by reproducing observables in systems with mass $A > 2$.

The goal of the work of Ref. [86] has been to benchmark SM calculations, now including also the contribution from a $N^2\text{LO}$ 3N potential, against those obtained with NCSM [87, 88], and consequently the adopted c_D, c_E values are -1, -0.34, respectively, as those employed in Ref. [87] (see Fig. 1 in [87]).

As already mentioned before, H_{eff} is calculated introducing the contribution of the $N^2\text{LO}$ 3N potential at first-order in many-body perturbation theory only for one- and two-valence nucleon systems. The contribution at first order to the single-particle and two-body components of the \hat{Q} box from a three-body potential are shown in Fig. 6 and their expression is reported in Eqs. (51) and (52). In Section 3.2.1 we have also pointed out that these expressions give the coefficients which multiply the one-body and two-body terms, respectively, arising from the normal-ordering decomposition of the three-body component of a many-body Hamiltonian [146].

In Figs. 15 and 16, we show the low-energy spectra of ${}^6\text{Li}$, ${}^8\text{Li}$, ${}^8\text{B}$, ${}^8\text{Be}$, ${}^{10}\text{B}$, ${}^{11}\text{B}$, ${}^{12}\text{C}$, and ${}^{13}\text{C}$, calculated within the SM framework, now including also the contributions from the $N^2\text{LO}$ 3N potential. They are compared with the experimental ones [193] and the NCSM results [87, 88].

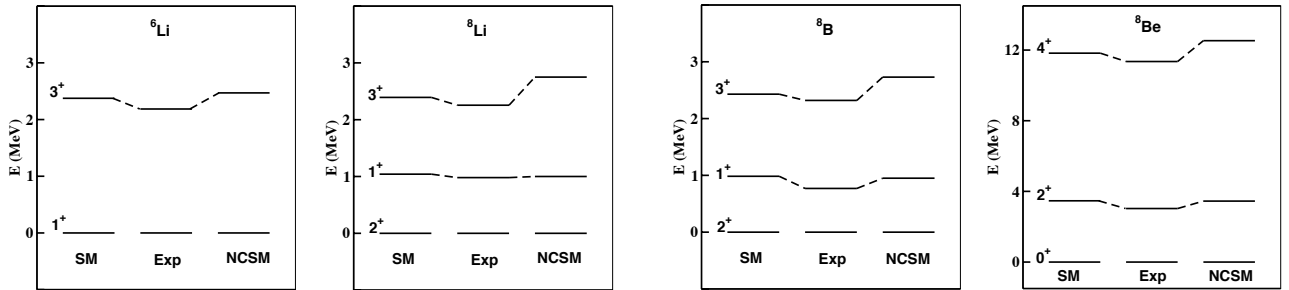


Figure 15: Theoretical and experimental spectra for ${}^6\text{Li}$, ${}^8\text{Li}$, ${}^8\text{B}$, and ${}^8\text{Be}$. The theoretical energies have been obtained using the $N^3\text{LO}$ NN plus $N^2\text{LO}$ 3N potentials within SM and NCSM calculations. Figure adapted from Ref. [86].

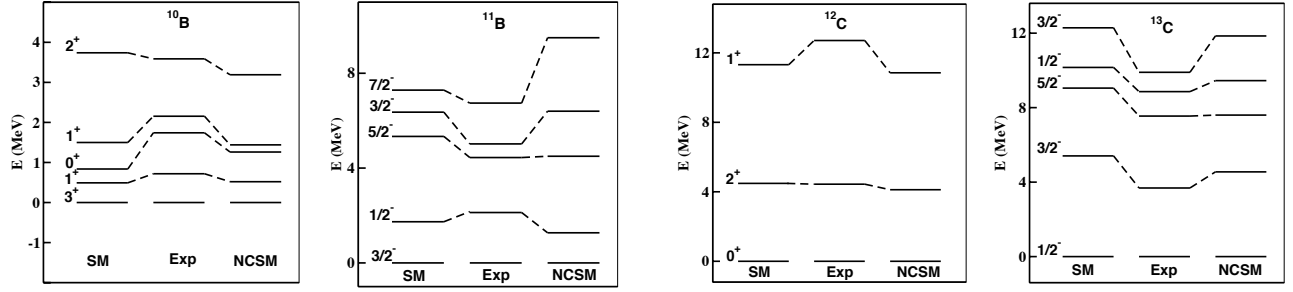


Figure 16: Same as in Fig. 15, but for ^{10}B , ^{11}B , ^{12}C , and ^{13}C . Figure adapted from Ref. [86].

From the inspection of Figs. 15 and 16, the results obtained with H_{eff} derived by expanding perturbatively the \hat{Q} box and the NCSM ones are in a close agreement, as in the case with only the NN potential. Moreover, the theory with the 3NF compares far better with experiment, as can be seen in all the reported spectra. In this regard, it is paramount, among other observations, to note that the experimental sequence of observed states in ^{10}B is restored, and the degeneracies of $J^\pi = 1/2_1^-, 3/2_1^-$ and $J^\pi = 3/2_2^-, 5/2_1^-$ states in ^{11}B are removed. This supports the crucial role played by the 3N potential to improve the spectroscopic description of p -shell nuclei.

4.2 Approaching the weakly bound systems

4.2.1 The limit of oxygen isotopes

The oxygen isotopic chain exhibits, in addition to the conventional doubly magic ^{16}O , the occurrence of two new shell closures in ^{22}O [195] and ^{24}O [54, 196, 197] with $N = 14$, and 16, respectively. Of particular interest is that the dripline is located at ^{24}O [198] very close to stability line, the so-called ‘‘Oxygen anomaly’’. The heaviest experimentally identified isotopes, ^{25}O and ^{26}O , are indeed unbound with respect to neutron emission [199, 200]. As a matter of fact, the doubly-closed nature of ^{24}O was suggested, before to be experimentally confirmed, by various SM calculations employing phenomenological interactions, which were also able to explain the occurrence of the neutron dripline at $N = 16$ [201–203]. In these papers, it was shown that the $N = 16$ shell gap arises from an upward shift of the $0d_{3/2}$ orbital, whose energy increases rapidly becoming close to zero while neutrons fill the sd shell. As for the $0s_{1/2}$ orbital, these calculations indicate that it remains bound and the $0d_{5/2} - 1s_{1/2}$ spacing opens up from $N = 8$ and 14 making $N = 14$ a magic number. On the other hand, realistic SM calculations based on 2NF-only predict that the $0d_{3/2}$ orbital comes down in energy with increasing number of valence neutrons and remains well bound in ^{24}O and beyond, putting the neutron dripline in an incorrect position.

The first study that has explicitly included the 3NF in the derivation of the effective SM Hamiltonian for oxygen isotopes has been carried out by Otsuka and coworkers [52]. In the Introduction, we referred to this work by mentioning calculations using a chiral NN $N^3\text{LO}$ potential plus 3N contributions. However, Ref. [52] also reports on the comparison with calculations employing phenomenological and realistic NN interactions, which more clearly highlights the effects of 3N forces on the limit of oxygen isotopes.

Specifically, g.s. energies of the oxygen isotopes are also obtained by using i) phenomenological SDPF-M [204] and USD-B [205] forces; ii) NN effective interactions derived by way of the MBPT at second order from a G matrix and including Fujita-Miyazawa 3N forces due to Δ excitations.

The comparison between results of these calculations is illustrated in Fig. 17. We see that the energies from phenomenological interactions well agree with experiment and the minimum value correctly

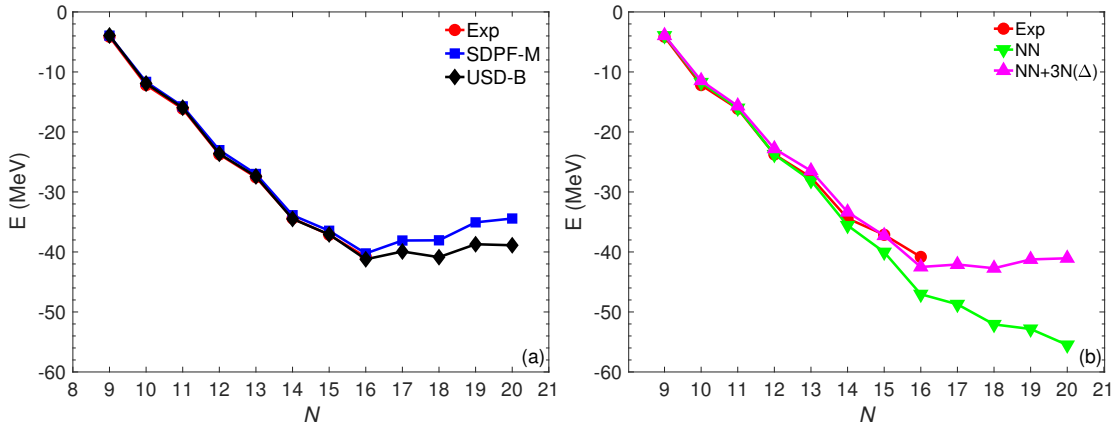


Figure 17: Ground-state energies of oxygen isotopes measured from ^{16}O , including experimental values of the bound $^{16-24}\text{O}$. Energies obtained from (a) phenomenological forces SDPF-M [201] and USD-B [126], (b) a G matrix and including Fujita-Miyazawa 3N forces due to Δ excitations. Figure adapted from Ref. [52].

locates at $N = 16$. By contrast, the energies based on the NN force-only do not stop to decrease putting the dripline at $N = 20$, regardless of the renormalization procedure employed for the NN potential (the same results are obtained by using the $V_{\text{low-k}}$ instead of the G matrix). Then, the effects introduced by including the Fujita-Miyazawa 3N contributions, which become more relevant with increasing neutron number, correct the behavior of the binding energies bringing a significant raise from $N = 16$ to 18.

Results of Ref. [52], have been confirmed by more recent calculations based on large many-body spaces and with improved MBPT and nonperturbative valence-space Hamiltonians. A summary of these calculations performed by using different *ab initio* approaches, including references, is in Ref. [59], where it is shown that they all predict the correct dripline position at ^{24}O when large many-body spaces are adopted with binding energy differing only within a few percentage.

As concerns oxygen isotopes beyond the dripline, the description of their binding energies and excitation spectra requires to consider the coupling with the continuum in addition to the 3NF contribution. This issue is presented within the GSM framework in Section 4.2.2, where also unbound resonance states in ^{24}O are discussed. The role played by the coupling with the continuum and the 3NF contribution is also evidenced for the proton-rich Borromean ^{17}Ne in Section 4.2.3.

4.2.2 3NF and continuum in neutron-rich oxygen isotopes

Neutron-rich oxygen isotopes have been attracting many interests from both experiment and theory, not only because of the famous ‘‘Oxygen Anomaly’’ [52], discussed above, but also their many peculiar phenomena. The ^{26}O ground state has been found barely unbound with two-neutron separation energy of only -18 keV [206], and an excited state in the unbound resonant isotope ^{25}O has been observed in a recent experiment [207]. Even though many theoretical works [52, 66, 208, 209] have shown the importance of 3NFs in nuclear structure calculations to reproduce the oxygen dripline position, there still exists a strong demand to consider the coupling to the continuum, which is crucial to the understanding of the loose structures of exotic nuclei. Using the GSM with chiral NN and 3N forces, we have investigated oxygen isotopes up to beyond the neutron dripline, in which both effects from the 3NF and continuum are considered.

For neutron-rich oxygen isotopes, we choose the doubly magic system ^{16}O as core, with its ground-state Slater determinant as reference state for the normal-ordering decomposition of 3NF. The Berggren basis is generated by the WS potential. We adopt the universal WS parameters [210], but reduce

the depth parameter by 2.3 MeV to obtain a reasonable $0d_{3/2}$ resonance width compared with the experimental width extracted in ^{17}O . This WS potential gives bound $0d_{5/2}$ and $1s_{1/2}$ orbitals and a resonant $0d_{3/2}$ orbital. In this Berggren basis produced by the WS potential, we construct the effective GSM interaction for the model space $\{0d_{5/2}, 1s_{1/2}, 0d_{3/2} \text{ pole plus continuum}\}$, using the MBPT of \hat{Q} -box folded diagrams, named EKK [181]. The detail about the complex- k MBPT can be found in our previous papers [173,180]. The continuum effect enters the model through both the complex effective interaction and the active model space which includes continuum partial waves. As discussed in the previous Section 3.3, the complex symmetric GSM Hamiltonian is diagonalized in the complex model space via the Jacobi-Davidson method.

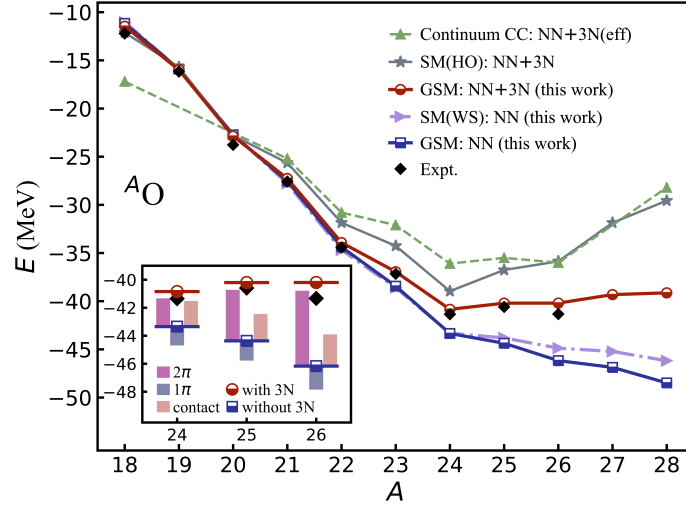


Figure 18: Calculated $^{18-28}\text{O}$ ground-state energies with respect to the ^{16}O core [92], compared with experimental data and other calculations: conventional SM (HO) with 3NF but without continuum [52] and continuum CC with a density-dependent effective 3NF [178]. The inset shows the 3NF contributions from 2PE (2π), 1PE (1π) and contact terms.

We have calculated the binding energies of oxygen isotopes, shown in Fig. 18. The comparison of different calculations given in the figure shows that both 3NF and continuum play important roles in reproducing the experimental binding energies, especially in the vicinity of the dripline. The 3NF gives repulsive contributions to g.s. energies and the effect increases with the increase of the number of valence neutrons. In the inset of Fig. 18, the 3NF effect has been dissected in $^{24-26}\text{O}$. We find that the attractive $v_{3N}^{(1\pi)}$ and repulsive $v_{3N}^{(\text{ct})}$ terms have similar values but opposite signs. Consequently, their effects are almost canceled out, implying that $v_{3N}^{(2\pi)}$ term is responsible for the observed 3NF repulsive effect in this mass region.

Fig. 19 displays the calculated excitation spectra of $^{24-26}\text{O}$. We see that 3NF also improves spectrum calculations compared with experimental data, especially for unbound resonance states, such as the excited 2_1^+ and 1_1^+ in ^{24}O and the ground state of ^{25}O . The calculations with 3NF included give better agreements with data in resonance widths.

4.2.3 3NF and continuum in proton-rich Borromean ^{17}Ne

Due to the Coulomb repulsion, the proton dripline is not so far from the stability line compared with the neutron dripline, which has been reached experimentally up to $Z \approx 90$ more than a decade ago [198]. However, when focusing on the light proton-rich region where the Coulomb barrier is not so high and continuum effect is prominent, interesting phenomena (such as halo and Borromean structures) may

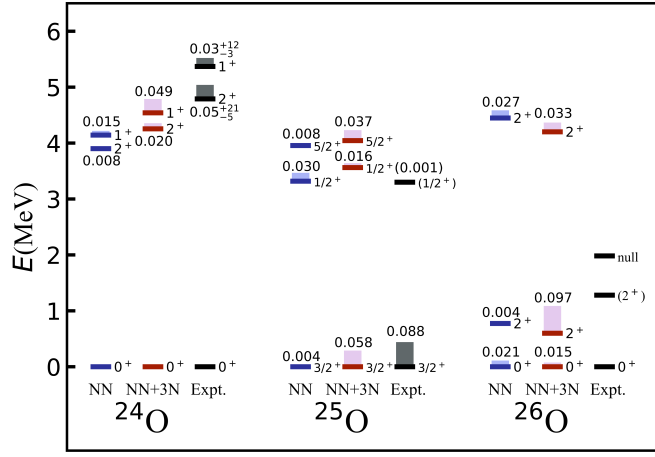


Figure 19: GSM calculations of excitation spectra for $^{24-26}\text{O}$ [92]. The experimental data are taken from [197, 200, 206, 207].

emerge. Among these nuclei, the Borromean ^{17}Ne is of particular interest in both experiment [211–213] and theory [214–216]. It may bear a similarity to the two-neutron halo nucleus ^6He which can be described as a three-body $^4\text{He} + 2n$ system. To see the weakly-bound characteristic in ^{17}Ne , we performed a realistic GSM calculation with the chiral N^3LO 2NF and N^2LO 3NF which were discussed already in Section 4.2.2.

In this calculation, we choose the closed-shell ^{14}O as the core. The GSM valence space contains the neutron bound states $\nu\{0p_{1/2}, 0d_{5/2}, 1s_{1/2}, 0d_{3/2}\}$ and the proton resonances $\pi\{1s_{1/2}, 0d_{5/2}\}$ plus continua $\pi\{s_{1/2}, d_{5/2}\}$. To reproduce the inverse positions of proton $1s_{1/2}$ and $0d_{5/2}$ orbitals in ^{15}F , the WS parameters need to be adjusted [93]. In detail, we reduce the spin-orbital coupling strength to 2 MeV, and reduce the depth parameter by 2 MeV for the proton WS potential. The valence-space Hamiltonian was obtained using MBPT as described in Sec. 4.2.2, and diagonalized by the Jacobi-Davidson method. More details can be found in Ref. [93].

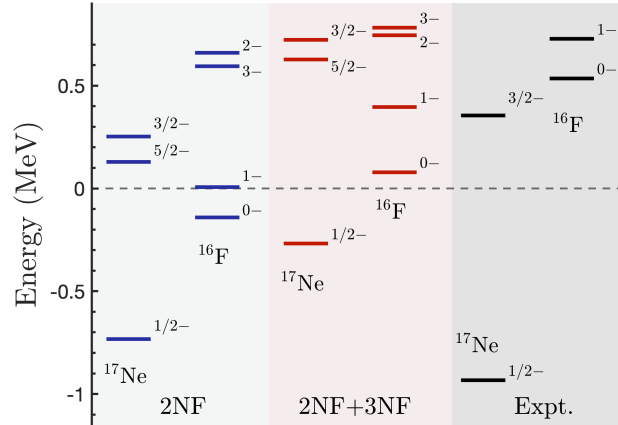


Figure 20: Calculated excitation spectra of ^{17}Ne along with its isotone ^{16}F , with respect to the ^{15}O ground-state energy [93]. Blue and red lines are the GSM calculations with 2NF only and 2NF+3NF, respectively. Experimental data are taken from Refs. [194, 212].

The calculated low-lying levels of ^{17}Ne and its subsystem ^{16}F are present in Fig. 20, with respect to the ^{15}O ground-state energy. It is seen that the 3NF lifts the whole spectra of ^{17}Ne and ^{16}F , which

makes ^{16}F unbound and leads to a Borromean structure of ^{17}Ne . In the g.s. of ^{17}Ne , we have found strong configuration mixing with a 54% s-wave component of $\pi 1s_{1/2}^2 \otimes \nu 0p_{1/2}^1$, which is consistent with that in Ref. [216].

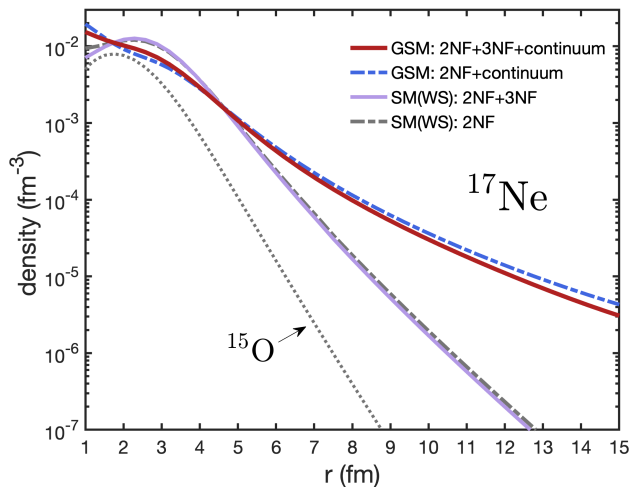


Figure 21: The ^{17}Ne density in the valence space, calculated by GSM with 2NF only (blue dot-dashed line) and 2NF+3NF (red line). SM (WS) stands for the conventional SM calculations performed in the non-continuum discrete WS basis, with 2NF+3NF (purple line) and 2NF only (grey dot-dashed line). The ^{15}O density (black dash line) in the valence space is also displayed for comparison.

The small two-proton separation energy and large weight of s-wave component suggest a halo structure in the ground state of ^{17}Ne . We have calculated the one-body density by GSM, shown in Fig. 21. Compared with ^{15}O , there exist a long tail in the density of ^{17}Ne , which is a direct evidence to support the halo nature of ^{17}Ne . From Fig. 21, we see that 3NF effect on the density is small, while the effect from the continuum coupling is significant. More detailed discussions can be found in Ref. [93].

4.2.4 The calcium isotopes dripline

The Ca isotopic chain, from the experimental point of view, presents characteristics similar to the oxygen one. In analogy to the shell gaps found in correspondence of $N = 14$ and 16 for oxygen isotopes, it exhibits two neutron shell closures at $N = 32$ [217–219] and 34 [220] in addition to the standard ones at $N = 20$ and 28 . However, while oxygen isotopes have been studied experimentally even beyond the neutron dripline [199, 206], not even its position is known in Ca isotopic chain. Indeed, experimental studies have reached only ^{60}Ca [221] with $N/Z = 2$ and 12 neutrons more than the last stable isotope.

From the theoretical side, calculations for Ca isotopes have been performed by both mean field and microscopic approaches – as relativistic Hartree-Bogoliubov or density functional theories (DFT) in the first case and SM or *ab initio* methods in the second – but their results provide ambiguous indications about the behavior of the g.s. energies as well as about the location of the neutron dripline. As matter of fact, some studies predict the neutron dripline around ^{60}Ca [63, 222–224] while others pushes it up ^{70}Ca [90, 225–230]. However, the available experimental data, including the recent evidence of a bound ^{60}Ca [221] and the mass measurements of heavy odd calcium isotopes [78, 219], may be very helpful to narrow the spread of the theoretical predictions.

As an illustrative example, we compare in Fig. 22 the experimental two-neutron separation energies ($S_{2n,s}$) for even Ca isotopes with results from different calculations. We see that DFT using the Skyrme interaction of Ref. [231] predicts that ^{60}Ca is well bound and the neutron dripline is around ^{70}Ca , as it comes out from other mean field calculations [225–229]. It is worth mentioning, however, that

the results depend on the symmetry energy, as clearly underlined in Ref. [227]. The last bound Ca isotope was located well beyond $N = 40$ also by GSM calculations which start from the CD-Bonn NN potential [230]. On the other hand, the position of the dripline predicted by the IM-SRG approach [224] is around ${}^{60}\text{Ca}$, as it is confirmed by other microscopic approaches (see Refs. [63, 223]). However, Holt and coworkers [25], who updated the SM results of Ref. [63], have underlined the difficulty of a precise prediction for the dripline due to the flat evolution of the g.s. energies beyond ${}^{60}\text{Ca}$. Figure 22 also reports S_{2n} s from SM calculations in the fp valence space based on the KB3G phenomenological interaction [232], and we see that the theoretical values nicely overlap the available experimental data and locate between the DFT and GSM curves.

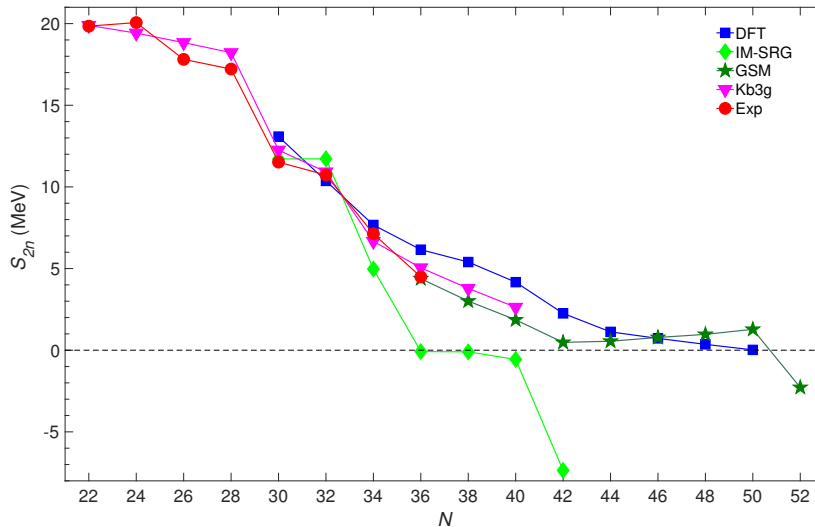


Figure 22: Experimental [233] two-neutron separation energies as a function of the neutron number N for Ca isotopes compared with the results of a variety on many-body methods. See text for details.

The study of the evolution of the nuclear masses in isotopic chains has pushed forward our understanding of the nuclear forces, drawing attentions on new aspects of nuclear forces that develop going from the valley of stability to the limits of existence. In this connection, particular attention is focused on 3NFs, which have shown to be critical in calculations of extreme neutron-rich systems. The effect of 3NFs on the dripline and on the shell evolution in Ca region has been the subject of investigations only in the last decade or so. The g.s. energies along the Ca isotopic chain have been studied starting from chiral NN and $3N$ potentials by way of the SM [25, 63, 89, 90], CC model [223], IM-SRG [224] and self-consistent Green function theory [33] approaches. In particular, SM calculations of Ref. [63] - performed within the fp space - have first evidenced that the inclusion of the three-body component in the derivation of the effective Hamiltonian leads to a repulsive contribution needed to correct the overbinding obtained when considering the NN force only, and provides a better agreement with the available experimental data, as observed for oxygen nuclei [52]. In Ref. [63], it was also shown that predictions with $NN+3N$ forces are quite close to those resulting from the phenomenological GXPF1 [127] and KB3G [232] NN interactions, which show similar monopole components [127] although developed by employing different techniques. This supports the relevant role of 3N forces in removing deficiencies of the two-body monopole component arising from NN -only theory. A careful analysis of the contribution of chiral 3NFs to the monopole component of the effective SM Hamiltonian is reported in Section 4.3.2.

Here, we shall discuss predictions of Ca dripline based on the realistic SM calculations of Refs. [89,90] performed in the $0f_{7/2}$, $0f_{5/2}$, $1p_{3/2}$, $1p_{1/2}$ (fp) neutron space as well as in the extended space including the neutron $0g_{9/2}$ orbital ($fp g_{9/2}$). In both cases, a chiral $NN+3N$ potential is chosen as starting point

to construct the effective SM Hamiltonians, but for the fp space we also report results obtained with the NN force only. The NN and 3N forces were derived within the ChPT framework [55] stopping the perturbative series at $N^3\text{LO}$ and at $N^2\text{LO}$, respectively (see Sections 2.2 and 4.1). We would like to reiterate here that the NN and 3N forces consistently share the same nonlocal regulator function and some LECs which are determined by the renormalization procedure described in Ref. [16], while the values of the additional LECs appearing in the 3N force, c_D and c_E , are taken from Ref. [87].

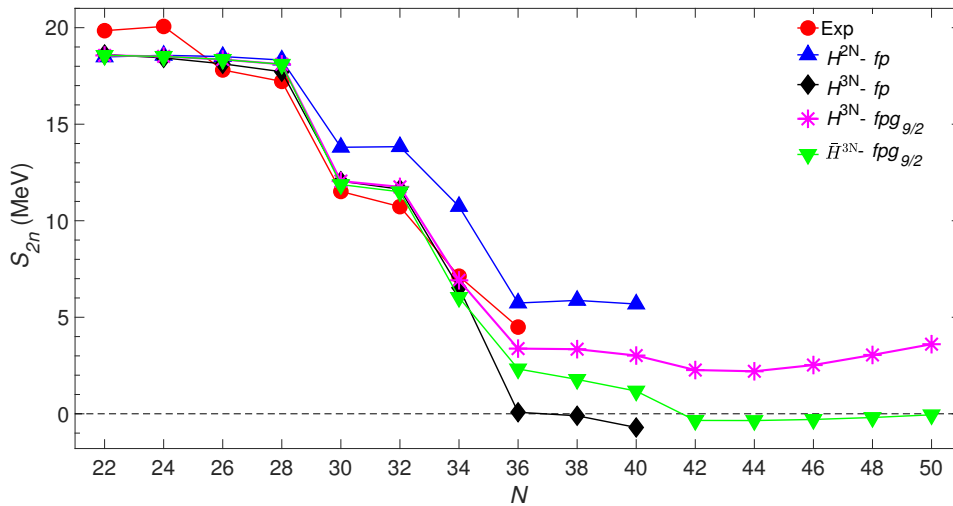


Figure 23: Experimental [233] two-neutron separation energies as a function of the neutron number N for Ca isotopes compared with SM results obtained within the fp and $fp g_{9/2}$ spaces. Calculations are based on the NN and $NN+3N$ forces. See text for details.

The effective Hamiltonians were derived within the framework of the MBPT outlined in Section 3.2.1 by arresting the \hat{Q} -box expansion of the one- and two-body Goldstone diagrams at third order in the NN potential and at first order in the 3N one, the latter diagrams corresponding to the normal-ordered one- and two-body parts of the 3N force. Moreover, calculations were carried out, as described in Section 3.2.1, by employing density-dependent H_{eff} s, whose TBMEs change according to the number of valence nucleons and take into account the interactions via two-body force of clusters of three-valence nucleons with configurations outside the model space. This means that, in addition to genuine 3N forces, we consider also induced 3N contributions, that come into play for systems with more than two-valence nucleons. It is worth mentioning that similar calculations, in both the fp and $fp g_{9/2}$ valence spaces, were performed in [25, 63], where, however, the NN chiral potential was renormalized through the $V_{\text{low-k}}$ technique [56] and the effects of induced three-body contributions in the derivation of H_{eff} were neglected.

The experimental S_{2n} s are compared with calculated values in Fig. 23. Results within the fp space obtained by using the NN and $NN+3N$ force are dubbed, respectively, as $H^{2N} - fp$ and $H^{3N} - fp$, while $H^{3N} - fpg_{9/2}$ indicates results in the $fp g_{9/2}$ space with the $NN+3N$ force. By comparing the $H^{2N} - fp$ and $H^{3N} - fp$ results, we see that both calculations reproduce the rather flat experimental S_{2n} behavior up to $N = 28$. Then, the measured values are overestimated when using the NN -only force, while, in line with the results of Refs. [25, 63], the repulsion due to the 3NF leads to less bound g.s. energies and improves the agreement with experiment. However, at $N = 36$ a too sudden drop is found by $H^{3N} - fp$, at variance with the experimental finding, which may be ascribed to the missing contributions arising from the $0g_{9/2}$ orbital. We find, indeed, that a larger S_{2n} , quite close to the experimental value, is predicted by $H^{3N} - fpg_{9/2}$ calculations at $N = 36$. As a matter of fact, when including both the neutron $0g_{9/2}$ orbital and the 3N force we are able to well describe the available experimental data, and in particular to predict ^{60}Ca as a bound system, consistently with the recent

experiment of Ref. [221]. We have also found that calcium isotopic chain is bound at least up to ^{70}Ca in line with the results of the DFT [231] and GSM [230] calculations mentioned above, and the recent Bayesian analysis of different DFT calculations [228].

In Fig. 23, labelled by $\bar{H}^{3N} - fpg_{9/2}$, we have also reported the S_{2n} s obtained by considering only a genuine chiral 3N force without accounting for induced 3N contributions. In this case, the same Hamiltonian derived for the two-body system is adopted for all Ca isotopes.

We see that results of the two Hamiltonians, $H^{3N} - fpg_{9/2}$ and $\bar{H}^{3N} - fpg_{9/2}$, almost overlap up to $N = 32$, but then differences between them start to grow and become larger and larger with increasing number of valence neutrons. Actually, from $N = 34$ on the inclusion of induced 3NFs brings an upshift of the two-neutron separation energies evidencing their attractive contribution which counterbalances in part the one arising from a genuine 3NF.

We may therefore conclude that the effects of these two 3NFs with very different origin are both equally important in determining the dripline of Ca isotopes. It is worth mentioning that similar results are obtained for Ti isotopes as shown in Ref. [91].

4.3 Shell evolution and the role of three-body forces

4.3.1 Overview: the fp shell region

The access to experimental information for nuclear systems with a large unbalanced number of neutrons and protons, the so-called exotic nuclei, has opened up new possibilities to advance our understanding of nuclear physics. One of the key questions that modern research has allowed to be address concerns the robustness of the standard magic numbers, namely the evolution of the shell structure as a function of N/Z , in particular when moving far from the stability line and approaching the driplines.

Significant theoretical and experimental efforts have been devoted in the last four decades to this issue by investigating nuclear structure properties along isotopic and isotonic chains. Experiments have been performed with radioactive beams to identify the disappearance of conventional magic numbers or the appearance of new ones, and at the same time a number of theoretical papers have been published aimed at understanding the underlying mechanisms determining such behaviour and the specific role of the various components of the nuclear interaction (see for instance [121, 234]). Noteworthy examples of disappearance or weakening of canonical magic numbers has been observed in light nuclei at $N = 8$, $N = 20$, and $N = 28$ for ^{12}Be , ^{32}Mg and ^{42}Si , respectively [235–240], while the onset of new shell closures at $N = 14$, 16 and $N = 32$, 34 has been evidenced, respectively, in neutron-rich oxygen [54, 197] and calcium isotopes [81, 217–220, 241–243]. As an illustration, we report in Fig. 24 the behaviour of the experimental excitation energy of the first 2^+ state and its $E2$ transition rate to the g.s. in the even $Z = 8$ isotopes and $N = 20$ isotones as a function of increasing N and Z , respectively [193].

We see that the 2^+ energy of oxygen isotopes in the left-hand side of Fig. 24 drops by a factor of about three from $N = 8$ to 10 before rising up at $N = 14$, with a more dramatic increase at $N = 16$. The behavior of the 2^+ energy may be seen as a manifestation of the doubly-magic nature of $^{24}\text{O}_{16}$, corresponding to the complete filling of the neutron $0d_{5/2}$ and $1s_{1/2}$ orbitals, and to the appearance of a significant $0d_{3/2} - 1s_{1/2}$ subshell gap. The increase in energy from $N = 12$ to $N = 14$ together with a decrease in the $B(E2, 2_1^+ \rightarrow 0_1^+)$ value testifies the existence of a consistent gap also between the neutron $0d_{5/2}$ and $1s_{1/2}$ orbitals.

The evolution of the $N = 20$ shell gap is illustrated on the right-hand side of Fig. 24. The persistence of the shell closure at $N = 20$ and the existence of significant $\pi 1s_{1/2} - \pi 0d_{5/2}$ and $\pi 0d_{3/2} - \pi 1s_{1/2}$ gaps account for the behavior of the 2_1^+ energy and $B(E2, 2_1^+ \rightarrow 0_1^+)$ transition rate in the $N = 20$ isotones from ^{34}Si to ^{40}Ca . However, no SM calculations limited to the sd space can account for the sudden and strong change from ^{32}Mg to ^{34}Si , where the 2^+ increases from ~ 0.9 to 3.3 MeV and the $B(E2)$ value decreases by a factor of about 4. This indicated a collective nature for ^{32}Mg , which can be explained only

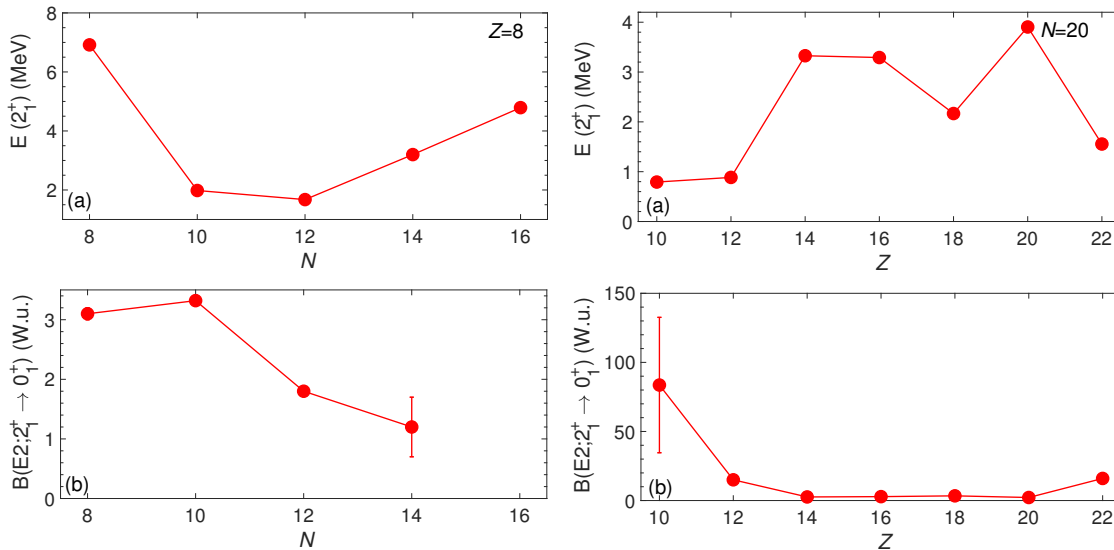


Figure 24: Experimental (a) 2_1^+ excitation energies and (b) $B(E2, 2_1^+ \rightarrow 0_1^+)$ transition rates in the $Z = 8$ isotopes (left) and $N = 20$ isotones (right).

by taking in account the correlation energy due to $2p - 2h$ neutron excitations [244]. These excitations are favoured over the normal sd configurations by the lowering of the gap between the sd and fp shells, that is produced as soon as protons are removed from the $0d_{5/2}$ orbital.

These changes in the shell structure, called shell evolution, and the interplay between spherical configurations and deformation are strictly connected to the monopole component of the interaction (Eq. (8)). In fact, as mentioned in Section 3.1, this component governs the behaviour of the ESPs (see Eq. (10)) by accounting for the variations in the SP energies arising from the residual interaction between the valence nucleons. In this connection, a particularly appealing subject is the role of the different components of the nuclear force in determining the monopole interaction, that was first raised in 2001 by T. Otsuka and collaborators [202]. More specifically, attention has been focused in literature on the evaluation of the contributions originating from the central, vector, tensor components as obtained from the spin-tensor decomposition of the SM Hamiltonian [245]. In Refs. [246, 247], it has been shown that the splitting of the spin-orbit partners is essentially due to the tensor component, although any part of the Hamiltonian can give a relevant contribution to the shell evolution.

Another important question that has been recently addressed is the relevance of 3NFs in the shell formation, as well as in the location of the neutron dripline as discussed in Section 4.2. In particular, its role in the shell formation has been investigated within the SM and IM-SRG approach for light- and medium-mass nuclei [25, 52, 58–61, 63, 69, 86, 89–91, 248], focusing mainly on the oxygen [52, 58–60, 69] and calcium [25, 60, 63, 89, 90] isotopic chains. In all these calculations, the effective Hamiltonians are derived from NN and $3N$ potentials built up within the chiral perturbative theory, while in [52, 249] the Fujita-Miyazawa three-body force is employed to study the low-lying states of neutron-rich nuclei with $Z = 8$, $Z = 10 - 14$ and $N \sim 20$.

The main results of all these works is that $3N$ forces give rise to a repulsive interaction between the valence particles that improves the agreement with experimental data. For instance, in Ref. [52], it was shown that the $3NF$ is able to correct the strong attractiveness of the monopole interaction between the $0d_{3/2}$ and $0d_{5/2}$ neutron orbitals, which explains the change in the location of the neutron dripline from ^{28}O to the experimentally observed ^{24}O , as discussed in Section 4.2.1.

Here, to illustrate the role of the $3NF$ in providing a reliable monopole component of the effective SM Hamiltonian we choose as physics case the nuclei of the fp shell, namely Ca, Ti, Cr, Fe, Ni isotopes

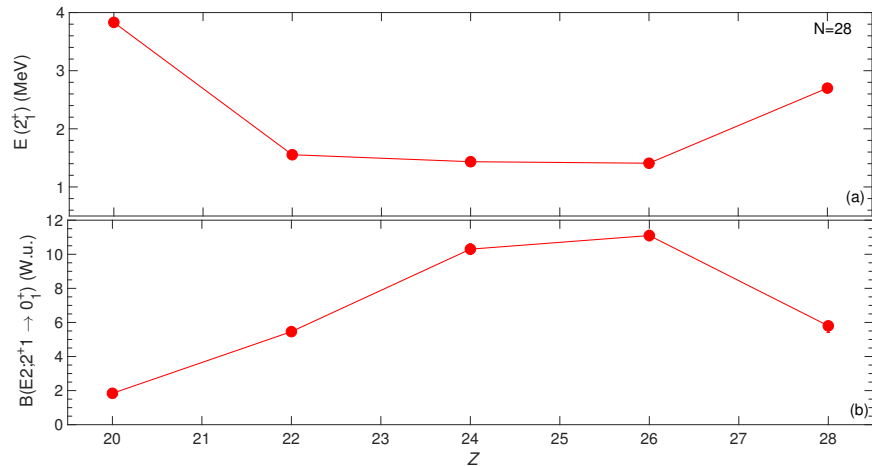


Figure 25: Experimental (a) 2_1^+ excitation energies and (b) $B(E2, 2_1^+ \rightarrow 0_1^+)$ transition rates in the $N = 28$ isotones.

from $N = 20$ to 32. Within this mass region, two doubly magic nuclei, ^{48}Ca and ^{56}Ni , are known, while an enhancement in the collectivity is observed for nuclei with $22 \leq Z \leq 26$ and $N = 28$, as can be seen in Fig. 25 reporting the experimental 2_1^+ excitation energies and the $B(E2, 2_1^+ \rightarrow 0_1^+)$ values for the $N = 28$ isotones [193].

This case may be, therefore, a good testing ground to investigate the relevance of 3NFs in generating gaps, and it may be of particular interest to study how 3NFs affect the $N = 28$ shell closure when the proton $0f_{7/2}$ orbital is getting filled.

In the next section, on the basis of the results obtained in Ref. [89], we discuss physical quantities as the excitation energies of the yrast 2^+ states, the $B(E2, 2_1^+ \rightarrow 0_1^+)$ values, and the two neutron separation energies focusing on the changes produced by the the 3N force on the monopole component of the effective interaction and on the ESPEs. In Section 4.3.3, the 3NF monopole component is analyzed in terms of the central, vector, and tensor contributions.

4.3.2 Monopole interaction and effective single-particle energies

Calculations have been performed within the SM framework by considering valence protons and neutrons interacting in the valence space composed by the $0f_{7/2}$, $0f_{5/2}$, $1p_{3/2}$, and $1p_{1/2}$ orbitals outside doubly magic ^{40}Ca . The adopted effective Hamiltonians are derived within the MBPT approach starting from the chiral NN -only and $NN+3N$ forces, as described in Section 4.2.4. As for the proton-proton channel the Coulomb force is added. We limit to consider nuclei from $N = 20$ to 32 to avoid that our predictions are affected by the choice of the adopted model space (see Section 4.2.4).

In the following, we focus on the S_{2n} s and excitation energies of the yrast 2^+ states by comparing the experimental data with the results of SM calculations obtained by employing effective Hamiltonians derived from the NN force only (H^{2N}) and the complete $NN + 3N$ force (H^{3N}). Furthermore, to better pinpoint the role of the monopole component and how it is affected by the 3NF we have also introduced a third Hamiltonian, H^{mon} , which is made up by summing the monopole component of H^{3N} to the multipole component of H^{2N} .

However, as a preliminary step, we should comment on the SP energies of the adopted effective Hamiltonians. As mentioned in Section 3.2.1, the derivation of H_{eff} for one-valence nucleon systems provides the theoretical SP energies, which are then subtracted from the diagonal matrix elements of H_{eff} derived for the two-valence nucleon systems to obtain the TBMEs of the residual interaction. The SP energies arising from NN -only theory do not supply a reasonable proton and neutron gap between the

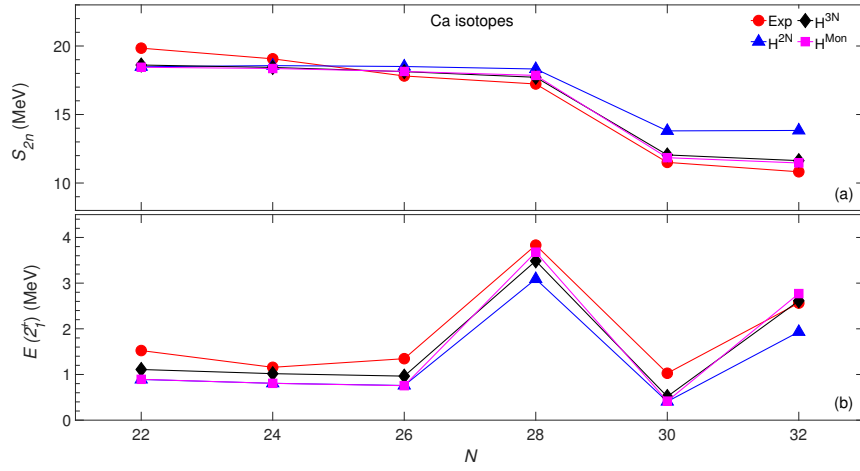


Figure 26: Experimental and calculated (a) two-neutron separation energies and (b) 2_1^+ excitation energies for calcium isotopes from $N = 22$ to 32 . See text for details.

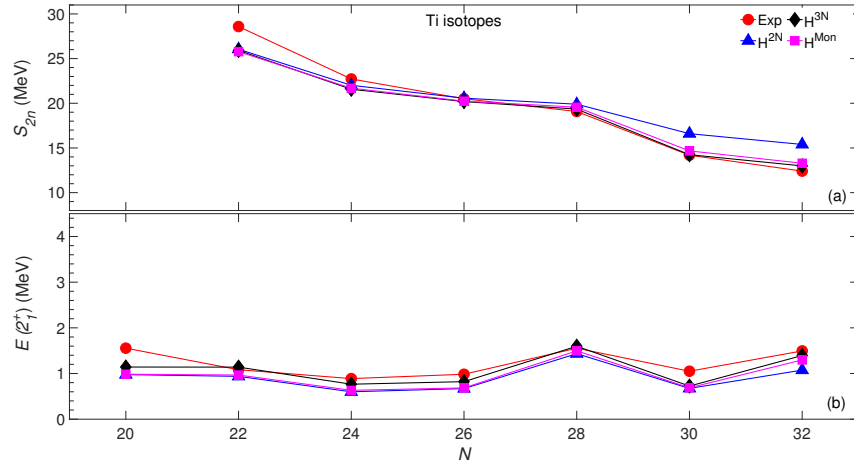


Figure 27: Experimental and calculated (a) two-neutron separation energies and (b) 2_1^+ excitation energies for titanium isotopes from $N = 20$ to 32 . See text for details.

$0f_{7/2}$ orbital and the remaining three orbitals [89], which might prevent the description of the observed shell closure at $Z, N = 28$. Therefore, in order to remove the effects due to the SP energies and concentrate on those produced by the two-body part of the effective Hamiltonians, specifically on their monopole components, calculations in all three cases (H^{2N} , H^{3N} , and H^{mon}) are carried out starting from the same set of SP energies, namely those derived from the $NN+3N$ force. The values of the neutron and proton SP energies can be found in Ref. [89].

In Figs. 26 – 30, the experimental data for the S_{2n} [233] and the excitation energies of the yrast 2^+ states [193] for Ca, Ti, Cr, Fe, and Ni isotopes from $N = 20$ to 32 are compared with the theoretical values obtained with H^{2N} , H^{3N} , and H^{mon} . Note that empty red circles for the experimental S_{2n} values refer to the estimated values reported in Ref. [233].

By comparing the theoretical S_{2n} s from H^{2N} and H^{3N} we observe, as already pointed out in Section 4.2.4, that the repulsive contributions of the 3NF is essential to quench the overbinding induced by the NN force only, thus producing a downshift of the S_{2n} curve and improving the agreement with experiment. When these contributions are taken into account, the calculated results follow closely the experimental behaviour for all the considered isotopes, while their omission leads to a bad reproduction

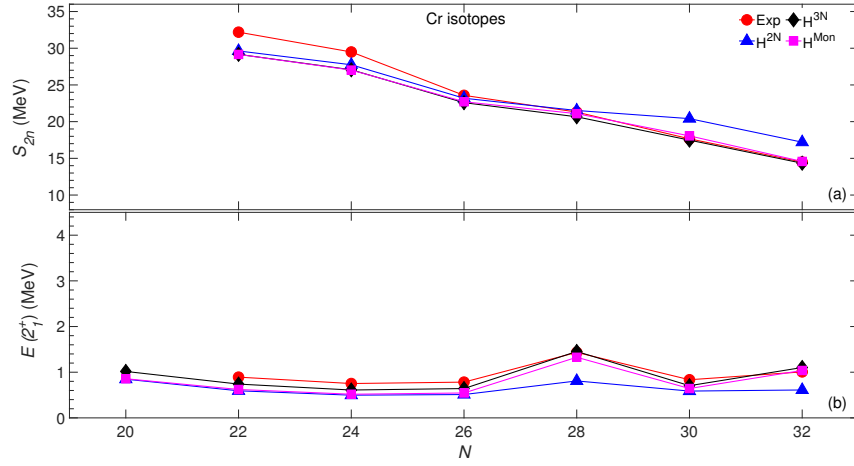


Figure 28: Experimental and calculated (a) two-neutron separation energies and (b) 2_1^+ excitation energies for chromium isotopes from $N = 20$ to 32. See text for details.

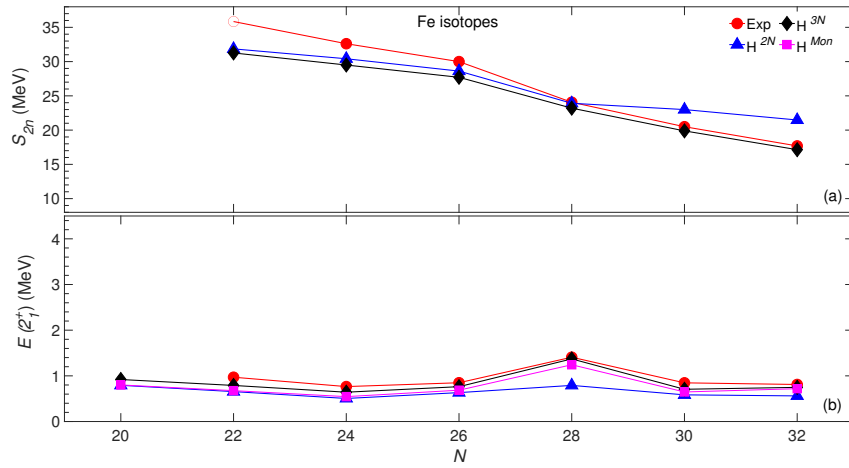


Figure 29: Experimental and calculated (a) two-neutron separation energies and (b) 2_1^+ excitation energies for iron isotopes from $N = 20$ to 32. See text for details.

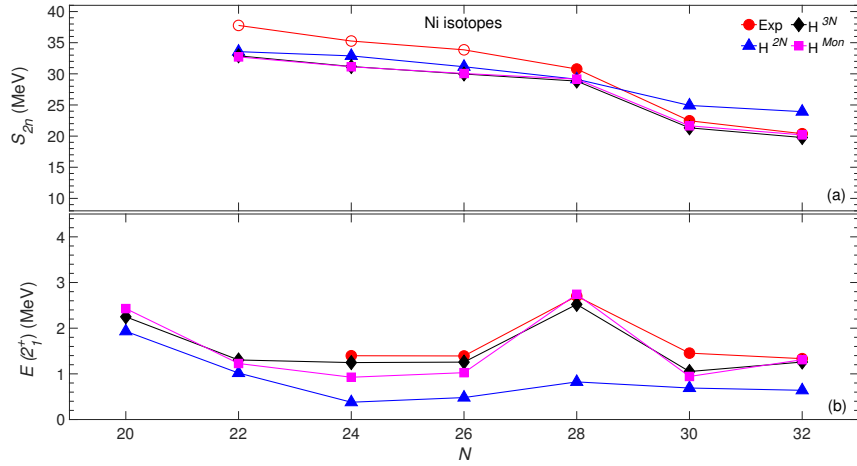


Figure 30: Experimental and calculated (a) two-neutron separation energies and (b) 2_1^+ excitation energies for nickel isotopes from $N = 20$ to 32. See text for details.

of the observed energy drop between $N = 28$ and 30. This drop can be seen as a manifestation of the shell closure at $N = 28$, corresponding to the filling of the $0f_{7/2}$ neutron orbital, and the deficiency of H^{2N} ascribed to the inadequate gap between the $0f_{7/2}$ and $1p_{3/2}$ neutron ESPE provided by this Hamiltonian.

On the other hand, H^{mon} and H^{3N} give very similar results, thus confirming the inaccuracy of the monopole components obtained by considering the NN force only, as well as the central role of these components in determining the S_{2n} evolution and the $N = 28$ shell closure. At the end of this section, we shall analyze the changes introduced by the 3NF in the neutron and proton ESPEs, which only depend on the monopole components of the Hamiltonian.

Similar considerations follow also from the excitation energies of the yrast 2^+ states. As shown in panel (b) of Fig. 26, the shell closure at $N = 28$ in Ca isotopes is very well reproduced by H^{3N} and H^{mon} , while the 2_1^+ state predicted by H^{2N} lies about 0.7 MeV below the experimental one. For Ti isotopes, we see in Fig. 27 that the experimental behavior is, overall, well reproduced by all three SM Hamiltonians, while for Cr and Fe isotopes (Figs. 28 and 29) the energy gap at $N = 28$ predicted by H^{2N} is underestimated by ~ 0.6 MeV, and the difference increases up ~ 1.8 MeV in Ni isotopes (Fig. 30). Another subshell closure at $N = 32$ is observed in Ca, Ti, Cr isotopes, although not so strong as that at $N = 28$, corresponding to the filling of the $1p_{3/2}$ neutron orbital. Also in this case results from H^{2N} provide, in general, a less satisfactory agreement with experimental data.

For all considered isotopic chains, calculations with H^{2N} underestimate the experimental excitation energy of the 2_1^+ states at both $N = 28$ and $N = 32$ providing too much collectivity. When moving from Ca isotopes with only identical valence nucleons to systems with $Z > 20$, we see a change in the closure properties that may arise from the collectivity induced from the proton-neutron channel of the residual interaction. This change reflects on the evolution of the $N = 28$ shell closure as a function of Z , which shows a lowering of the yrast 2^+ state and an increase of the $B(E2; 2_1^+ \rightarrow 0_1^+)$ value for nuclei with $22 \leq Z \leq 26$. as discussed at the end of Section 4.3 from the experimental point of view.

In Fig. 31, the experimental excitation energies of the 2_1^+ states and the $B(E2; 2_1^+ \rightarrow 0_1^+)$ values are compared with the H^{2N} , H^{3N} , and H^{mon} results. The proton and neutron effective charges to calculate the $B(E2)$ s have been consistently obtained with the same perturbation approach of the Hamiltonian, without any empirical adjustment, as described in Section 3.2.1.

The collectivity evolution between ^{48}Ca and ^{56}Ni is well reproduced by H^{3N} and H^{mon} , but not by H^{2N} . In particular, the latter Hamiltonian is not able to describe the doubly magic nature of ^{56}Ni . The

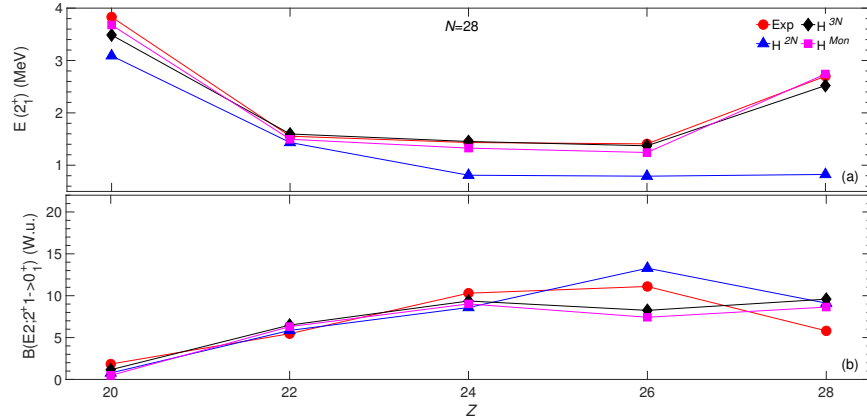


Figure 31: Experimental and calculated (a) 2_1^+ excitation energies and (b) $B(E2, 2_1^+ \rightarrow 0_1^+)$ transition rates for $N = 28$ isotones from $Z = 20$ to 28. See text for details.

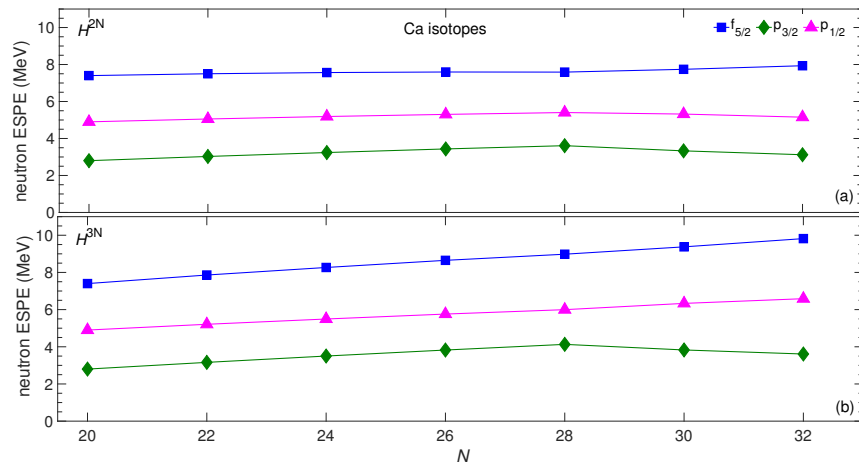


Figure 32: Neutron ESPEs from (a) H^{2N} and (b) H^{3N} for calcium isotopes as a function of the neutron number. See text for details.

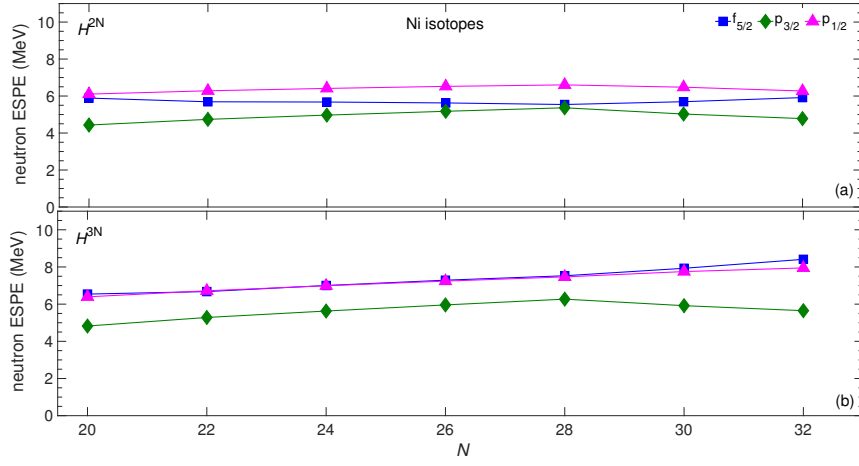


Figure 33: Neutron ESPEs from (a) H^{2N} and (b) H^{3N} for nickel isotopes as a function of the neutron number. See text for details.

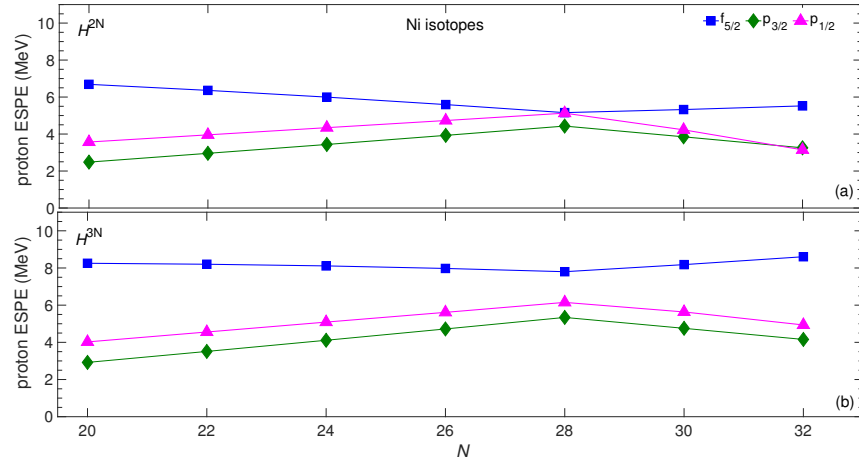


Figure 34: Proton ESPEs from (a) H^{2N} and (b) H^{3N} for nickel isotopes as a function of the neutron number. See text for details.

monopole component of H^{2N} , responsible for the evolution of the neutron and proton ESPEs, cannot balance indeed the collectivity induced by higher multipole components in the proton-neutron channel.

To better elucidate this point we examine, in the following, the proton and neutron ESPEs as a function of the number of valence neutrons. In particular, we compare the neutron ESPEs for Ca isotopes and both neutron and proton ESPEs for Ni isotopes obtained by employing the monopole component of H^{2N} and H^{3N} . The ESPEs are defined in Eq. (10) with the g.s. occupation numbers, n_b^τ , fixed by employing the normal filling scheme, namely by putting the valence nucleons into the possible lowest orbit one by one. The results are reported in Figs. 32, 33, 34 where the ESPEs are referred to the lowest lying $0f_{7/2}$ orbital. It is worth recalling that in all cases the starting SP energies are those derived by adopting the $NN+3N$ force.

From the inspection of Fig. 32, for calcium isotopes, we can observe that the inclusion of the 3NF does not affect the general behavior of the neutron ESPEs, but provides specific features that give rise to the difference in the results of the H^{2N} and H^{3N} discussed above. We see, in fact, that the neutron monopole component H^{3N} produces an increase in the $1p_{3/2} - 0f_{7/2}$ energy gap at $N = 28$ inducing a stronger shell closure, and also a larger $1p_{1/2} - 1p_{3/2}$ splitting in correspondence of the $N = 32$ subshell

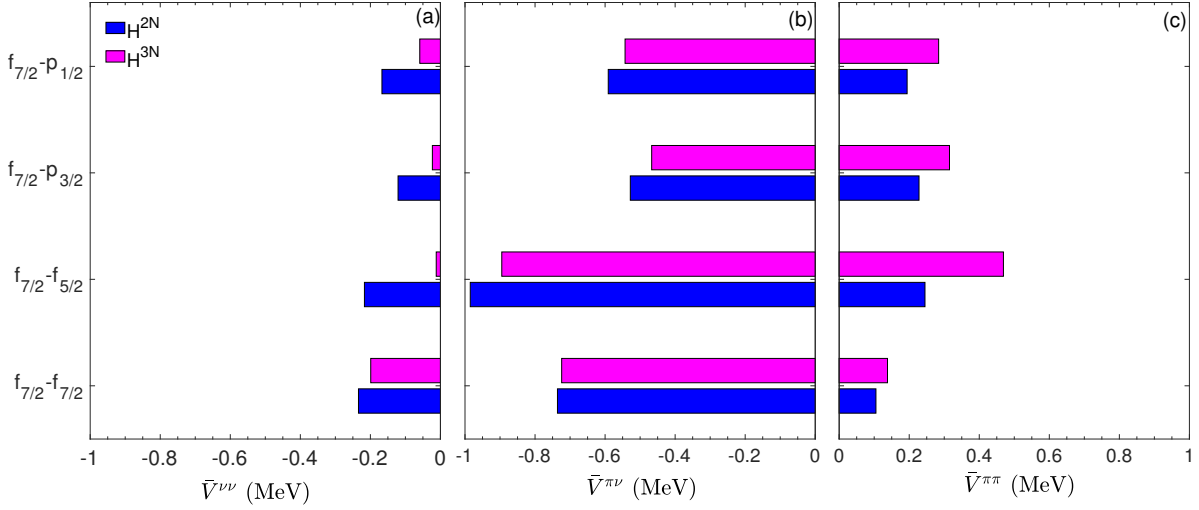


Figure 35: (a) Neutron-neutron, (b) proton-neutron (b), and (c) proton-proton monopole matrix elements of the effective interactions with and without 3N force. See text for details

closure. It is also interesting to note that a larger energy splitting is found for both pairs of the $1p$ and $0f$ spin-orbit partners when 3NFs are taken into account. This effect grows with increasing neutron number.

Similar comments can be made for the neutron and proton ESPEs in Ni isotopes, which are shown in Figs. 33 and 34. It can be seen that the inclusion of the 3NF provides an increase in the $0f_{7/2} - 1p_{3/2}$ and $1p_{1/2} - 1p_{3/2}$ splittings at $N = 28$ and $N = 32$, respectively, for both the neutron and proton ESPEs. In general, the contribution of the 3NF leads to a substantial expansion of the orbital separations with respect to the NN force only. In particular, the $0f_{7/2} - 0f_{5/2}$ spin-orbit splitting at $N = 28$ increases by about 2 and 3 MeV for neutrons and protons, respectively. Furthermore, the strong narrowing we observe at $N = 28$ for the $0f_{5/2}$ and $1p_{3/2}$ orbitals with the NN force is significantly attenuated by including the 3NF.

To summarize, we have shown that the monopole component of the 3NF is crucial to correct the behavior of the ESPEs and smooth the too much collectivity resulting from H^{2N} thus leading to results able to reproduce the experimental data and the doubly magic nature of ^{56}Ni . A careful analysis of the difference in the monopole components of H^{2N} and H^{3N} will be presented in the next section.

4.3.3 Spin-tensor decomposition of the shell-model interaction

The difference in the behavior of the ESPEs resulting when employing the NN force only and the complete $NN + 3N$ force lies in the effects produced by the 3N component on the monopole matrix elements of the effective SM Hamiltonian. In order to better substantiate this statement, we consider the ^{56}Ni case, whose neutron and proton shell gaps are strongly affected by the inclusion of the 3NF, as discussed in the previous section. We therefore compare the monopole matrix elements, namely the centroids of the two density-dependent Hamiltonians, H^{2N} and H^{3N} , we have used for the calculations of this nucleus. In particular, for the sake of simplicity we focus on the matrix elements $\bar{V}_{ab}^{\tau\tau'}$ (see Eq. (9)) with at least one of the two indices, a or b , representing the $0f_{7/2}$ orbital. In fact, since in the calculation of the ESPEs we adopt the normal filling scheme only these matrix elements come into play for ^{56}Ni . In Fig. 35, we report the centroids $\bar{V}_{0f_{7/2}b}^{\tau\tau'}$ of H^{2N} and H^{3N} for the neutron-neutron, proton-neutron, and proton-proton channels. It is worth mentioning that neutron-neutron and proton-neutron interactions determine the neutron ESPEs, while the proton ones depend on proton-proton

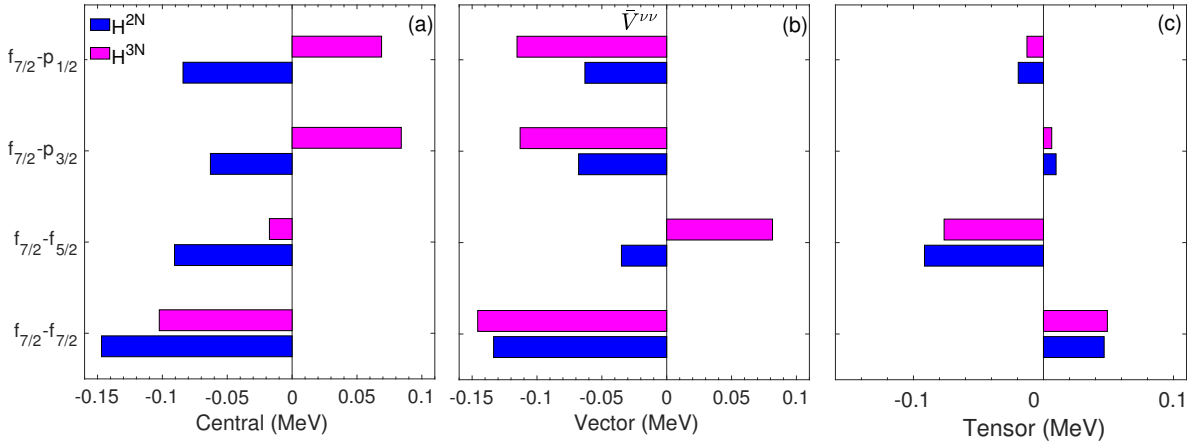


Figure 36: (a) Central, (b) vector, and (c) tensor contributions to $\bar{V}_{0f_{7/2}b}^{\tau\tau'}$ with and without 3N force. See text for details.

and proton-neutron interactions. We see that the 3NF provides a repulsive contribution to all matrix elements, which makes the neutron-neutron and proton-neutron matrix elements less attractive and the proton-proton ones more repulsive. However, the size of the contributions depends on the involved orbitals, ranging from few tens of keV to about 200 keV, which produces a substantial change in the spacings between the ESPE's and consequently in the variation of the shell structure in correspondence of a sizable occupation of a specific orbital, as it is the case of the $0f_{7/2}$ orbital in ^{56}Ni . In all three channels, the changes produced by H^{3N} are larger for the $\bar{V}_{0f_{7/2}b}^{\tau\tau'}$ matrix elements with $b \neq 0f_{7/2}$ than for the diagonal ones. This leads to a larger gap between the $0f_{7/2}$ orbital and the remaining orbitals in both the proton and neutron space when the complete $NN + 3N$ force is adopted, which results in a stronger shell closure at $N = 28$ for Ni isotopes as discussed in Section 4.3.2.

It can be also observed that the increased spacing between the $0f_{7/2} - 0f_{5/2}$ spin-orbit partners and the $0f_{5/2} - 1p_{3/2}$ orbitals, obtained when including the 3NF, is directly related to the stronger effects that this force has on the $\bar{V}_{0f_{7/2}0f_{5/2}}^{\tau\tau'}$ matrix elements as compared to the other ones.

In closing this section, we have found it instructive to analyze the monopole matrix elements of H^{2N} and H^{3N} in terms of their tensorial structure. As mentioned in Section 4.3.1, several studies, aimed to understand the mechanism behind the ESPE variations, have been devoted to investigate the role of the central, vector, and tensor components of the effective interactions in governing the shell evolution (see, for instance, Refs. [121, 246, 247, 250, 251]). As a main result, it has been found that the behavior of each ESPE is essentially controlled by the central component, while it is the interplay of all the three components to determine the evolution of the spacings between the ESPEs, with the tensor one significantly contributing to the changes in the spin-orbit splittings. However, these studies have concerned essentially phenomenological effective interactions and microscopic effective interactions derived from the NN force only. In particular, it has been shown that empirical adjustments of the latter interactions introduce, in general, more significant changes in the central and vector components than in the tensor one, especially for the proton-neutron matrix elements [247].

Here, we are interested to explicitly investigate the effects of the 3N force on the effective interaction to see if its contribution affects in particular a specific component of the effective interaction, and verify the conclusions drawn from the investigations of empirical adjusted interactions. To this end, we shall employ the spin-tensor decomposition to extract the central, vector, tensor contributions from the monopole matrix elements of our effective interaction, by following the procedure presented in Ref. [245] and outlined below for the sake of completeness.

Any scalar two-body interaction V for spin 1/2 fermions can be written in terms of spherical tensors

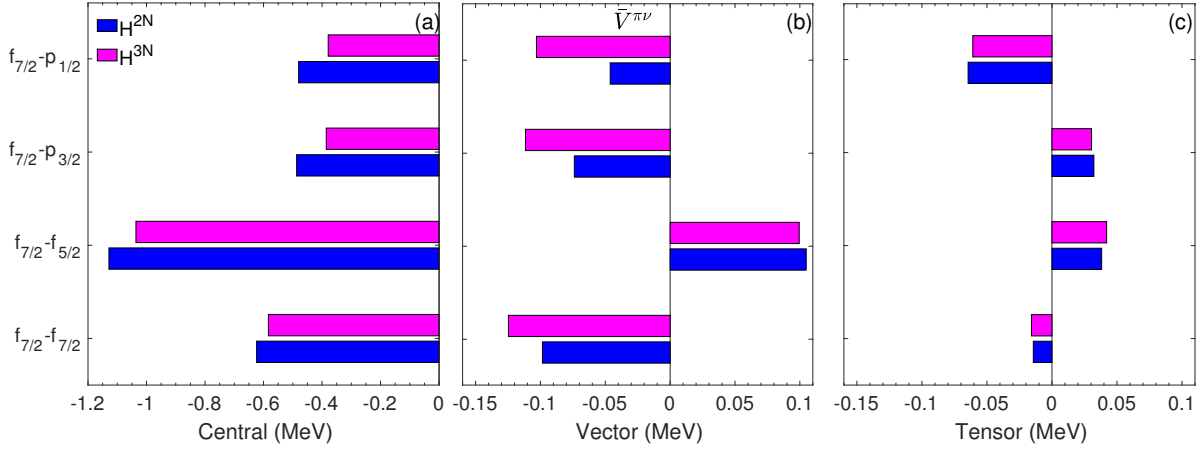


Figure 37: (a) Central, (b) vector, and (c) tensor contributions to $\bar{V}_{0f_{7/2}b}^{\pi\nu}$ with and without 3N force. See text for details. Note that a different scale is used for the vector and tensor components with respect to the central one.

by coupling the spin tensor operators (S^k) with the corresponding rank tensors in the configuration space (Q^k) as

$$V(1,2) = \sum_{k=0,1,2} (S^k \cdot Q^k) = \sum_{k=0,1,2} V^k, \quad (80)$$

where V^0 , V^1 , and V^2 are, respectively, the central, vector, and tensor components of the interaction V . Their matrix elements take the expression

$$\begin{aligned} \langle a\tau b\tau'; J|V^k|c\tau d\tau'; J\rangle &= \sum_{LL'SS'} U \begin{pmatrix} l_a & 1/2 & j_a \\ l_b & 1/2 & j_b \\ L & S & J \end{pmatrix} U \begin{pmatrix} l_c & 1/2 & j_c \\ l_d & 1/2 & j_d \\ L' & S' & J \end{pmatrix} \\ &\times \hat{k}^2 \begin{Bmatrix} L & S & J \\ S' & L' & k \end{Bmatrix} \sum_{J'} (-1)^{J'} \hat{J}' \begin{Bmatrix} L & S & J' \\ S' & L' & k \end{Bmatrix} \langle n_a l_a \tau n_b l_b \tau'; LSJ'|V|n_c \tau l_c n_d l_d \tau'; L'S'J' \rangle, \end{aligned} \quad (81)$$

with the coefficients U representing the generalized $9-j$ symbols

$$U \begin{pmatrix} l_a & 1/2 & j_a \\ l_b & 1/2 & j_b \\ L & S & J \end{pmatrix} = \hat{j}_a \hat{j}_b \hat{L} \hat{S} \begin{Bmatrix} l_a & 1/2 & j_b \\ l_b & 1/2 & j_a \\ L & S & J \end{Bmatrix}. \quad (82)$$

The LS -coupling matrix elements of V in Eq. 81 are obtained from the jj -coupling scheme in the standard way

$$\begin{aligned} \langle n_a l_a \tau n_b l_b \tau'; LSJ|V|n_c \tau l_c n_d l_d \tau'; L'S'J \rangle &= \sum_{j_a j_b j_c j_d} U \begin{pmatrix} l_a & 1/2 & j_a \\ l_b & 1/2 & j_b \\ L & S & J \end{pmatrix} U \begin{pmatrix} l_c & 1/2 & j_c \\ l_d & 1/2 & j_d \\ L' & S' & J \end{pmatrix} \\ &\times \langle a\tau b\tau'; J|V|c\tau d\tau'; J \rangle. \end{aligned} \quad (83)$$

By employing Eq. 80, the monopole matrix elements $\bar{V}_{ab}^{\tau\tau'}$, presented in Fig. 35, are decomposed in their central, vector, tensor contents, which are reported in Figs. 36, 37, and 38 for the the neutron-neutron, proton-neutron, and proton-proton channels, respectively.

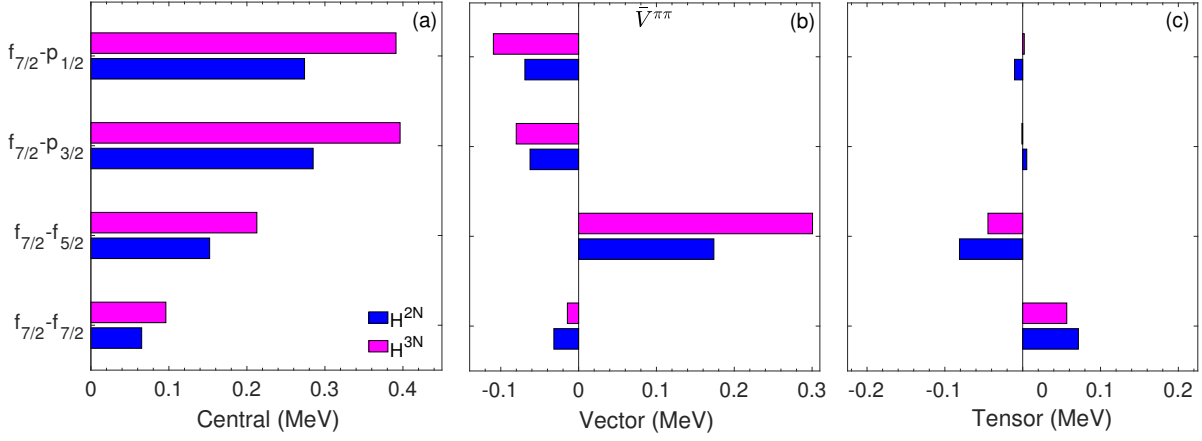


Figure 38: (a) Central, (b) vector and (c) tensor contributions to $\bar{V}_{0f_{7/2}b}^{\pi\pi}$ with and without 3N force. See text for details.

We see that the tensor content of all matrix elements is rather small with respect to the central and vector ones for $H^{2\text{NF}}$ as well as for $H^{3\text{NF}}$. As matter of fact, the tensor components in both cases are of the order of tens of keV, and changes due to the 3NF are limited to few keV in the vast majority of cases. The effects of the 3NF are instead more relevant for the the central and vector components. However, while the 3NF provides always a repulsive contribution to the central components, this is not the case for the vector ones. The nature of these matrix elements is, in fact, enhanced by the inclusion of the 3NF with the exception of $\bar{V}_{0f_{7/2}0f_{5/2}}^{\pi\nu}$ which changes from negative to positive.

Table 1: Spin-tensor contents of centroid differences $\Delta_b^{\tau\tau'}$ (in MeV). See text for details.

$V^{\nu\nu}$								
	$H^{2\text{N}}$				$H^{3\text{N}}$			
β	C	V	T	Tot	C	V	T	Tot
$0f_{5/2}$	0.056	0.090	-0.138	0.008	0.085	0.227	-0.126	0.186
$1p_{3/2}$	0.084	0.066	-0.037	0.113	0.187	0.033	-0.043	0.177
$1p_{1/2}$	0.063	0.070	-0.066	0.067	0.171	0.030	-0.061	0.140
$V^{\pi\nu}$								
	$H^{2\text{N}}$				$H^{3\text{N}}$			
β	C	V	T	Tot	C	V	T	Tot
$0f_{5/2}$	-0.505	0.203	0.053	-0.249	-0.453	0.224	0.058	-0.171
$1p_{3/2}$	0.137	0.025	0.047	0.209	0.198	0.013	0.046	0.257
$1p_{1/2}$	0.144	0.052	-0.050	0.146	0.204	0.022	-0.045	0.181
$V^{\pi\pi}$								
	$H^{2\text{N}}$				$H^{3\text{N}}$			
β	C	V	T	Tot	C	V	T	Tot
$0f_{5/2}$	0.087	0.206	-0.153	0.140	0.117	0.315	-0.101	0.331
$1p_{3/2}$	0.220	-0.031	-0.066	0.123	0.300	-0.066	-0.058	0.176
$1p_{1/2}$	0.209	-0.037	-0.082	0.090	0.295	-0.095	-0.055	0.145

As also evidenced in prior studies, the behavior of the ESPEs is largely determined for both $H^{2\text{N}}$ and $H^{3\text{N}}$ by the central and vector components, and in particular by the central monopole proton-

neutron interaction. It is this component that is mainly responsible for pushing down all the single-particle orbitals, and the attenuation of its attractiveness induced by the 3NF leads to a reduction of this phenomenon. However, in studying the shell-structure evolution we are more interested in the spacings between ESPEs than in their absolute values, and therefore attention should be focused on the differences between the centroids. These differences, calculated with respect to $\bar{V}_{0f_{7/2}0f_{7/2}}^{\tau\tau'}$, are denoted by $\Delta_b^{\tau\tau'}$ and reported in Table 4.3.3. It can be seen that the tensor content of the $\Delta_b^{\tau\tau'}$ is more relevant as compared to that of the single centroids and the central component loses in part its dominant role, all three components of the monopole interaction becoming important in determining the energy gaps.

In particular, as observed in Section 4.3.2, the inclusion of the 3NF brings an increase of about 2 MeV in the neutron $0f_{7/2} - 0f_{5/2}$ spin-orbit splitting at $N = 28$. As a matter of fact, the 2NF force only leads to a decrease of the same amount with respect to the original SP value (7.4 MeV) that is determined by the almost complete balancing of the central, vector, tensor components of $\Delta_{0f_{5/2}}^{\nu\nu}$ and by the consequent dominance of central monopole proton-neutron matrix element, whose attraction is only partially mitigated by the vector and tensor parts. The inclusion of the 3NF provides an increase of the repulsive neutron-neutron component, arising essentially from the increase of the vector term, that cancels the proton-neutron contribution. A similar mechanism explains the increase of ~ 3 MeV in the proton $0f_{7/2} - 0f_{5/2}$ spin-orbit splitting resulting from the 3NF.

As concerns the neutron and proton $0f_{7/2} - 1p_{3/2}$ spacings, a significant growth at $N = 28$ is produced already by the 2NF only (see Figs. 33 and 34). The $\Delta_b^{\tau\tau'}$ values of Table 4.3.3 evidence that it is related to the overall positive interference of all components of the monopole terms, while the further increase we find with H^{3N} comes out from the changes that the 3NF induces in the central terms.

5 Summary and conclusions

In this review paper, we have discussed the state of current developments to account for 3NFs within the SM framework and their impact on our understanding of nuclear structure properties. We have focused on realistic SM calculations with effective interactions derived from the QCD level and shown how crucial these forces are for describing binding energies and formation of shell structure. Particular attention has been devoted to the effects of 3NFs on the monopole component of the SM effective interaction by highlighting how relevant they are in correcting the monopole interaction derived from realistic the 2NF only.

As widely discussed in the text, starting from 1990s it was realized that the problems arising when using effective SM Hamiltonians derived from NN potentials by means of MBPT should be associated to deficiencies in its monopole component and adjustments were introduced so to obtain results of a quality comparable with the ones provided by phenomenological interactions [41]. However, the connection with the lack of the 3NF was only suggested few years later [47], and subsequently the first SM study including explicitly the effects of 3NFs was carried out for the sd shell nuclei [52].

We have focused on standard and Gamow shell models employing effective Hamiltonians derived within the MBPT approach from chiral NN and 3N forces, and reported calculations for nuclei ranging from light- to intermediate-mass nuclei. In addition to the effects of genuine chiral 3NFs, we have also discussed the role of induced 3NFs due to the interaction of clusters of three-valence nucleons with configurations outside the model space via the 2NF. Results are presented in Section 4 and compared with experiment, as well as with results from other approaches whenever possible and/or useful. In this section, we have also discussed in detail the interplay between 3NFs and the coupling with continuum for the description of weakly-bound states in the sd region and the structure of ^{17}Ne by means of the realistic GSM.

In the following, we shall summarize the main features coming from the results presented in Section 4.

1. We have evidenced the validity of the MBPT in deriving the effective SM Hamiltonian by using as testing ground p -shell nuclei. The perturbative behavior of H_{effs} derived from chiral NN potentials has been assessed by showing that the convergence properties of the \hat{Q} -box vertex function with respect to the dimension of the intermediate state space and the order-by-order convergence can be taken under control. Then, the quality of the results has been checked by benchmark calculations with the comparison of SM and ab initio NCSM results arising from chiral NN -only and $NN+3N$ forces.

2. The detailed discussion presented for fp shell nuclei clearly emphasizes the relevance of the 3NF contribution in determining the location of the neutron dripline and the evolution of the shell structure. We have shown that genuine 3NFs provide a repulsive interaction, which, although partially counterbalanced by induced 3N forces accounting for excitations outside the valence space, is essential to quench the overbinding of the g.s energies produced by the NN force. Our results for the S_{2n} s and the 2_1^+ excitation energies evidence that their effect increases with an increasing number of valence nucleons and is non-negligible in the formation of the shell structure, reflecting, in particular, on the closure properties of ^{58}Ni . Furthermore, our calculations with a modified interaction, obtained by combing the multipole and monopole components of effective Hamiltonians derived, respectively, from the NN and $NN+3N$ potential, soundly confirm that 3NFs affect essentially the monopole component. It has turned out that monopole component of the 3NF is crucial to correct the behavior of the ESPEs and produce the needed increase in the $0f_{7/2} - 0f_{5/2}$ spin-orbit splitting at $N = 28$ for both protons and neutrons. The main feature of the 3NF is its repulsive nature, as also evidenced in prior studies. However, the size of the contribution depends on the involved orbitals which produces a substantial change in the spacings between the ESPEs and consequently in the variation of the shell structure in correspondence of a large occupation of a specific orbital. From our analysis based on the spin-tensor decomposition of the monopole SM interaction, it has resulted that the central component - which acquires in all channels a significant repulsive contribution from the 3NF - is mainly responsible for the behavior of the ESPEs. On the other hand, when focusing on the spacings between ESPEs rather than on their absolute values, we have seen that also the vector and tensor components come into play, and therefore the shell structure depends on the interplay between all the three components.

3. Calculations performed within the GSM framework, in which continuum and resonance are included, have shown that 3NFs are non-negligible in explaining the dripline position in oxygen chain and the unbound properties of isotopes beyond the dripline as well as the Borromean structure of the proton-rich ^{17}Ne . As in standard SM calculations, the 3NF gives repulsive contributions to the g.s. energies, and its effect increases with the increase of the number of valence neutrons. As a matter of fact, it becomes crucial in the neutron dripline region by pushing up the $0d_{3/2}$ and $1s_{1/2}$ orbitals, when they start to be heavily occupied. Furthermore, a dissection of 3NF clearly evidences the main role of the two-pion exchange term with respect to the one-pion and contact ones which, having the same values but opposite signs, almost cancel out. An improved agreement with experiment and theory is found even in the case of spectra and resonance widths when including the 3NF. We have found that the repulsive contribution of the 3N force is also essential to explain the Borromean structure of ^{17}Ne by inducing an increase in energy of ^{16}F over the threshold of the proton emission.

Important demonstrations of the effect of 3NFs in the SM context are now available, which show their origin and importance in nuclear spectroscopy and explain the empirical modifications one should introduce in effective interactions derived from realistic NN potentials. A major step in this direction has been the derivation of nuclear potentials in terms of the chiral EFT that provides many-body forces consistently with the nature of the NN interaction. These are the so-called genuine 3N forces that originates from neglecting subnucleonic degrees of freedom. However, it is worth mentioning that, as long as we choose to use an inert core, there are also induced 3N forces accounting for excitations outside the valence space, which gives rise to the mass dependence of effective SM interactions.

In the future, important advances for a better understanding of the role of 3NFs within the realistic SM are the extension of calculations to heavier systems. Improvements in our 3NF treatment are also

desirable, as the inclusion of higher-order contributions with 3N vertices in the perturbative expansion of the effective Hamiltonian and the development of a technique to account for the 3NF among valence particles. We also would point out that completely consistent calculations require that all effective operators for general observables, not just the Hamiltonian, should be constructed from $NN+3N$ potentials derived within the framework of chiral EFT, by including two-body meson-exchange corrections originating from subnucleonic degrees of freedom.

In closing, it may be interesting to mention as possible development the inclusion of subleading 3NFs beyond the $N^2\text{LO}$ development. While the two-pion-exchange 3NFs at $N^3\text{LO}$ are expected to produce rather weak effects as evidenced in the calculations for the nucleon-deuteron system of Ishikawa *et al.* [111], the short-range 3NFs at $N^3\text{LO}$ [112] and $N^4\text{LO}$ [114] could play a non-negligible role in few-body systems. Therefore, the subleading-short-range 3NFs should be considered to include more sizeable contributions.

Acknowledgements

This work was supported by the Japan Society for the Promotion of Science KAKENHI under Grant No JP21K13919; the National Key R&D Program of China under Grant No. 2018YFA0404401; the National Natural Science Foundation of China under Grants No. 11835001, No. 11921006, No. 12035001, No. 121051062, and No. 121051063; the China Postdoctoral Science Foundation under Grants No. BX20200136, No. 2020M682747. The authors thank Nunzio Itaco for helpful comments and fruitful discussions.

A Three-body matrix elements for shell-model calculations

Here we show the formalism of the three-body matrix elements (MEs) of the chiral 3NF at $N^2\text{LO}$. First, we describe the three-body states in terms of the HO basis functions, which enables us to easily factor out the center-of-mass (c.m.) motion of the three-body states. Next, the antisymmetrization of the three-body states is explained. By introducing the Jacobi coordinates, the three-body MEs are reduced to simple forms, which we call the Jacobi-HO MEs. Finally, the Jacobi-HO MEs of each term of the chiral 3NF are given.

A.1 Three-body states

First, we define the single-particle state $|nljm_jm_\tau\rangle$ of a nucleon as

$$|nljm_jm_\tau\rangle = |\Phi_{nljm_j}\rangle \left| \varphi_{\frac{1}{2}m_\tau}^{(\tau)} \right\rangle, \quad (84)$$

$$|\Phi_{nljm_j}\rangle = \left| \left[\phi_{nl} \otimes \varphi_{\frac{1}{2}m_\tau}^{(\sigma)} \right]_{jm_j} \right\rangle, \quad (85)$$

where Φ_{nljm_j} is specified by the principal quantum number n , the orbital angular momentum l , and the total spin j . The projections to the z axis in association with l and j are respectively m_l and m_j . In Eq. (85), the wave function in the j scheme is obtained by coupling ϕ_{nlm_l} with the nucleon spin wave function $\varphi_{\frac{1}{2}m_\sigma}^{(\sigma)}$. The isospin component is expressed by $\varphi_{\frac{1}{2}m_\tau}^{(\tau)}$. Here m_σ and m_τ are the z components of the nucleon spin and isospin, respectively. The spatial wave function ϕ_{nlm_l} is expressed in terms of the HO basis functions:

$$\phi_{nlm_l}(\mathbf{r}) = \frac{R_{nl}(r)}{r} Y_{lm_l}(\hat{\mathbf{r}}), \quad (86)$$

with the spherical harmonics Y_{lm_l} , and \mathbf{r} specifying the position of the nucleon. The HO-wave function R_{nl} is written by

$$R_{nl}(r) = \left[\frac{2n!}{b_0^3 \Gamma(l+n+\frac{3}{2})} \right]^{\frac{1}{2}} r \left(\frac{r}{b_0} \right)^l \exp \left[- \left(\frac{r}{\sqrt{2}b_0} \right)^2 \right] L_n^{l+\frac{1}{2}} \left(\frac{r^2}{b_0^2} \right), \quad (87)$$

The so-called size parameter is expressed by $b_0 = \sqrt{\hbar/(m_N \omega)}$ with the HO-angular velocity ω and the average nucleon mass m_N , while Γ and $L_n^{l+\frac{1}{2}}$ are the gamma function and the Laguerre polynomial, respectively.

Next, we consider three interacting nucleons. In the following, we explicitly put the subscripts of the quantum numbers to distinguish the particles, a , b , and c . We symbolically express the single-particle quantum numbers as $a = \{n_a, l_a, j_a\}$. Thus, in the jj -coupling scheme, the product of the three single-particle wave functions reads

$$\begin{aligned} & |(a, b), c; J_{12} J T_{12} T\rangle \\ &= (-)^{J \hat{j}_a \hat{j}_b \hat{j}_c \hat{J}_{12}} \sum_{\substack{L_{12} S_{12} \\ L S}} (-)^{L+S} \hat{L}_{12}^2 \hat{S}_{12} \hat{L}^2 \hat{S}^2 \begin{Bmatrix} l_a & \frac{1}{2} & j_a \\ l_b & \frac{1}{2} & j_b \\ L_{12} & S_{12} & J_{12} \end{Bmatrix} \begin{Bmatrix} L_{12} & S_{12} & J_{12} \\ l_c & \frac{1}{2} & j_c \\ L & S & J \end{Bmatrix} \\ &\times \sum_{\substack{n_{12} l_{12} \\ \mathcal{N}_{12} \mathcal{L}_{12}}} (-)^{l_{12}+l_c+L_{12}} \langle\langle \mathcal{N}_{12} \mathcal{L}_{12} n_{12} l_{12}, L_{12} | n_a l_a n_b l_b, L_{12} \rangle\rangle_{d_1} \sum_{\mathcal{J}} (-)^{\mathcal{J}} \hat{\mathcal{J}}^2 \begin{Bmatrix} l_{12} & \mathcal{L}_{12} & L_{12} \\ l_c & L & \mathcal{J} \end{Bmatrix} \\ &\times \sum_{\substack{n_l \\ \mathcal{N} \mathcal{L}}} \langle\langle \mathcal{N} \mathcal{L} n l, \mathcal{J} | \mathcal{N}_{12} \mathcal{L}_{12} n_c l_c, \mathcal{J} \rangle\rangle_{d_2} \sum_{\substack{\mathcal{K} \mathcal{I} \\ I_{12} I}} \hat{\mathcal{K}}^2 \hat{\mathcal{I}}_{12} \hat{I} \begin{Bmatrix} \mathcal{L} & l & \mathcal{J} \\ l_{12} & L & \mathcal{K} \end{Bmatrix} \begin{Bmatrix} \mathcal{L} & \mathcal{K} & L \\ S & J & \mathcal{I} \end{Bmatrix} \begin{Bmatrix} l_{12} & l & \mathcal{K} \\ S_{12} & \frac{1}{2} & S \\ I_{12} & I & \mathcal{I} \end{Bmatrix} \\ &\times \sum_{\mathcal{M}_{\mathcal{L}} \mathcal{M}_{\mathcal{I}}} (\mathcal{L} \mathcal{M}_{\mathcal{L}} \mathcal{I} \mathcal{M}_{\mathcal{I}} | J M_J) |\phi_{\mathcal{N} \mathcal{L} \mathcal{M}_{\mathcal{L}}}\rangle |(n_{12} l_{12} S_{12}) I_{12} T_{12} (n l) I; \mathcal{I} T\rangle, \end{aligned} \quad (88)$$

where $|(n_{12} l_{12} S_{12}) I_{12} T_{12} (n l) I; \mathcal{I} T\rangle$ is the Jacobi-HO state defined by

$$\begin{aligned} & |(n_{12} l_{12} S_{12}) I_{12} T_{12} (n l) I; \mathcal{I} T\rangle \\ &= \left| \left[\left[\phi_{n_{12} l_{12}} \otimes \left[\varphi_{\frac{1}{2}}^{(\sigma)} \otimes \varphi_{\frac{1}{2}}^{(\sigma)} \right]_{S_{12}} \right]_{I_{12}} \otimes \left[\phi_{n l} \otimes \varphi_{\frac{1}{2}}^{(\sigma)} \right]_I \right]_{\mathcal{I} \mathcal{M}_T} \right\rangle \\ &\times \left| \left[\left[\varphi_{\frac{1}{2}}^{(\tau)} \otimes \varphi_{\frac{1}{2}}^{(\tau)} \right]_{T_{12}} \otimes \varphi_{\frac{1}{2}}^{(\tau)} \right]_{T \mathcal{M}_T} \right\rangle. \end{aligned} \quad (89)$$

The total angular momentum (total isospin) and its projection to the z axis are represented by J and M_J (T and M_T), respectively. We also introduce J_{12} (T_{12}), which are obtained by coupling j_a and j_b (the isospins of a and b). The harmonic-oscillator bracket, $\langle\langle \cdots | \cdots \rangle\rangle_{d_n}$, originates from the Talmi transformation [252–254], and its explicit expression is given, for example, in Refs. [255–257]. The subscript d_n specifies the mass ratio relevant to the Talmi transformation of the n -body system, namely, $d_1 = 1$ and $d_2 = 2$. One can see that the c.m. motion described by $|\phi_{\mathcal{N} \mathcal{L} \mathcal{M}_{\mathcal{L}}}\rangle$ is factored out.

A.2 Antisymmetrization

The three-body antisymmetrizer is given by

$$\hat{A}_3 = \frac{1}{3!} \left[\mathbb{1} - \hat{\mathcal{P}}_{ab} - \hat{\mathcal{P}}_{bc} - \hat{\mathcal{P}}_{ca} + \hat{\mathcal{P}}_{ab} \hat{\mathcal{P}}_{bc} + \hat{\mathcal{P}}_{ab} \hat{\mathcal{P}}_{ca} \right], \quad (90)$$

where $\mathbb{1}$ is the unity operator and $\hat{\mathcal{P}}_{ab}$ is the permutation operator with respect to the particles a and b . Using Eq. (88), the antisymmetrized jj -coupled state reads

$$\begin{aligned}
& |(a, b), c; J_{12}JT_{12}T\rangle_A \\
&= \sqrt{6}\hat{\mathcal{A}}_3 |(a, b), c; J_{12}JT_{12}T\rangle \\
&= (-)^{J\hat{j}_a\hat{j}_b\hat{j}_c\hat{J}_{12}} \sum_{\substack{L_{12}S_{12} \\ LS}} (-)^{L+S}\hat{L}_{12}^2\hat{S}_{12}\hat{L}^2\hat{S}^2 \begin{Bmatrix} l_a & \frac{1}{2} & j_a \\ l_b & \frac{1}{2} & j_b \\ L_{12} & S_{12} & J_{12} \end{Bmatrix} \begin{Bmatrix} L_{12} & S_{12} & J_{12} \\ l_c & \frac{1}{2} & j_c \\ L & S & J \end{Bmatrix} \\
&\times \sum_{\substack{n_{12}l_{12} \\ \mathcal{N}_{12}\mathcal{L}_{12}}} (-)^{l_{12}+l_c+L_{12}} \langle\langle \mathcal{N}_{12}\mathcal{L}_{12}n_{12}l_{12}, L_{12} | n_a l_a n_b l_b, L_{12} \rangle\rangle_{d_1} \sum_{\mathcal{J}} (-)^{\mathcal{J}} \hat{\mathcal{J}}^2 \begin{Bmatrix} l_{12} & \mathcal{L}_{12} & L_{12} \\ l_c & L & \mathcal{J} \end{Bmatrix} \\
&\times \sum_{\substack{nl \\ \mathcal{N}\mathcal{L}}} \langle\langle \mathcal{N}\mathcal{L}nl, \mathcal{J} | \mathcal{N}_{12}\mathcal{L}_{12}n_c l_c, \mathcal{J} \rangle\rangle_{d_2} \sum_{\substack{\mathcal{K}\mathcal{I} \\ I_{12}I}} \hat{\mathcal{K}}^2 \hat{\mathcal{I}}_{12} \hat{I} \begin{Bmatrix} \mathcal{L} & l & \mathcal{J} \\ l_{12} & L & \mathcal{K} \end{Bmatrix} \begin{Bmatrix} \mathcal{L} & \mathcal{K} & L \\ S & J & \mathcal{I} \end{Bmatrix} \begin{Bmatrix} l_{12} & l & \mathcal{K} \\ S_{12} & \frac{1}{2} & S \\ I_{12} & I & \mathcal{I} \end{Bmatrix} \\
&\times \sum_{\mathcal{M}_{\mathcal{L}}\mathcal{M}_{\mathcal{I}}} (\mathcal{L}\mathcal{M}_{\mathcal{L}}\mathcal{I}\mathcal{M}_{\mathcal{I}} | JM_J) |\phi_{\mathcal{N}\mathcal{L}\mathcal{M}_{\mathcal{L}}}\rangle |i_1; \mathcal{IT}\rangle_A, \tag{91}
\end{aligned}$$

with

$$|i; \mathcal{IT}\rangle_A = \sqrt{6}\hat{\mathcal{A}}_3 |i; \mathcal{IT}\rangle, \tag{92}$$

where the Jacobi-HO state $|i; \mathcal{IT}\rangle$ is defined by Eq. (89), and we simplify the set of quantum numbers:

$$i = \{n_{12}, l_{12}, S_{12}, I_{12}, T_{12}, n, l, I\}. \tag{93}$$

Now our task is to antisymmetrize the Jacobi-HO states. To this end, we expand the antisymmetrizer $\hat{\mathcal{A}}_3$ using the spectral decomposition as

$$\hat{\mathcal{A}}_3 = \sum_{\eta} \epsilon_{\eta} |\eta\rangle \langle\eta|, \tag{94}$$

where $|\eta\rangle$ are the eigenfunctions of $\hat{\mathcal{A}}_3$ characterized by a quantum number η . The eigenvalue ϵ_{η} should be 0 or 1 because the antisymmetrizer $\hat{\mathcal{A}}_3$ is idempotent. The eigenstates corresponding to $\epsilon_{\eta} = 1$ form physical antisymmetrized states, while the other eigenstates with $\epsilon_{\eta} = 0$ give spurious states [258, 259]. By selecting the physical states only, Eq. (92) can be written as

$$|i; \mathcal{IT}\rangle_A = \sqrt{6} \sum_j D_{ij}^{(\mathcal{IT})} |j; \mathcal{IT}\rangle, \tag{95}$$

$$D_{ij}^{(\mathcal{IT})} = \sum_{\eta}^{N_P} C_{\eta}^{i(\mathcal{IT})} C_{\eta}^{j(\mathcal{IT})*}, \tag{96}$$

$$C_{\eta}^{i(\mathcal{IT})} = \langle\eta | i; \mathcal{IT}\rangle, \tag{97}$$

with

$$j = \{n'_{12}, l'_{12}, S'_{12}, I'_{12}, T'_{12}, n', l', I'\}. \tag{98}$$

Here, $|\eta\rangle$ is expanded in terms of the partially antisymmetrized states, i.e., the antisymmetrization only for the first two particles (ab) is considered. Thus, the condition $(-)^{l_{12}+S'_{12}+T'_{12}} = -1$ is always satisfied. How to evaluate the number of the physical states N_P is given later.

The coefficient $C_\eta^{i(\mathcal{IT})}$ is computed as follows. Since $|\eta\rangle$ satisfies the eigenvalue equation,

$$\left(\hat{\mathcal{A}}_3 - \epsilon_\eta\right) |\eta\rangle = 0, \quad (99)$$

we obtain

$$\sum_j \langle i; \mathcal{IT} | \left(\hat{\mathcal{A}}_3 - \epsilon_\eta\right) | j; \mathcal{IT} \rangle C_\eta^{j(\mathcal{IT})*} = 0. \quad (100)$$

Thus, $C_\eta^{j(\mathcal{IT})*}$ is obtained by diagonalizing the antisymmetrizer matrix, the matrix element of which is given by

$$\mathcal{A}_{ij} = \langle i; \mathcal{IT} | \hat{\mathcal{A}}_3 | j; \mathcal{IT} \rangle = \frac{1}{3} \langle i; \mathcal{IT} | \left(\mathbb{1} - 2\hat{\mathcal{P}}_{bc}\right) | j; \mathcal{IT} \rangle, \quad (101)$$

and

$$\begin{aligned} \langle i; \mathcal{IT} | \hat{\mathcal{P}}_{bc} | j; \mathcal{IT} \rangle &= (-)^{l_{12}+l'_{12}} \hat{I}_{12} \hat{I}'_{12} \hat{I} \hat{I}' \hat{S}_{12} \hat{S}'_{12} \hat{T}_{12} \hat{T}'_{12} \begin{Bmatrix} \frac{1}{2} & \frac{1}{2} & T_{12} \\ \frac{1}{2} & T & T'_{12} \end{Bmatrix} \\ &\times \sum_{\lambda\sigma} \hat{\lambda}^2 \hat{\sigma}^2 \begin{Bmatrix} \frac{1}{2} & \frac{1}{2} & S_{12} \\ \frac{1}{2} & \sigma & S'_{12} \end{Bmatrix} \begin{Bmatrix} l_{12} & S_{12} & I_{12} \\ l & \frac{1}{2} & I \\ \lambda & \sigma & \mathcal{I} \end{Bmatrix} \begin{Bmatrix} l'_{12} & S'_{12} & I'_{12} \\ l' & \frac{1}{2} & I' \\ \lambda & \sigma & \mathcal{I} \end{Bmatrix} \\ &\times \langle \langle n_{12} l_{12} n l, \lambda | n'_{12} l'_{12} n' l', \lambda \rangle \rangle_{d_3}. \end{aligned} \quad (102)$$

Note that the Jacobi-HO states are orthonormal: $\langle i; \mathcal{IT} | j; \mathcal{IT} \rangle = \delta_{ij}$. The mass ratio in the harmonic-oscillator bracket is now $d_3 = 1/3$. The number of the physical states N_P is given as a sum of the eigenvalues, i.e., the trace of the antisymmetrizer matrix after the diagonalization.

A.3 Structures of three-body matrix elements

A.3.1 JT -coupled three-body matrix elements

From Eq. (91), the antisymmetrized JT -coupled matrix elements for the three-body interaction V_{3N} is given by

$$\begin{aligned} &{}_A \langle (d, e), f; J'_{12} J T'_{12} T | V_{3N} | (a, b), c; J_{12} J T_{12} T \rangle_A \\ &= \sum_{\substack{n_{12} l_{12} S_{12} I_{12} \\ n l I}} \sum_{\substack{n'_{12} l'_{12} S'_{12} I'_{12} \\ n' l' I'}} \sum_{\mathcal{I}} {}_A \langle \kappa'; \mathcal{IT} | V_{3N} | \kappa; \mathcal{IT} \rangle_A \\ &\times \sum_{\mathcal{N}\mathcal{L}} T_{abc J_{12} J \mathcal{I} \mathcal{N} \mathcal{L}}^{n_{12} l_{12} S_{12} I_{12} n l I} T_{def J'_{12} J \mathcal{I} \mathcal{N} \mathcal{L}}^{n'_{12} l'_{12} S'_{12} I'_{12} n' l' I'}, \end{aligned} \quad (103)$$

where the coefficient $T_{abcJ_{12}J\mathcal{L}N\mathcal{L}}^{n_{12}l_{12}S_{12}I_{12}nI}$, called the T coefficient [260, 261], is defined by

$$\begin{aligned}
T_{abcJ_{12}J\mathcal{L}N\mathcal{L}}^{n_{12}l_{12}S_{12}I_{12}nI} &= (-)^{l_c+l_{12}+J} \hat{j}_a \hat{j}_b \hat{j}_c \hat{J}_{12} \hat{S}_{12} \hat{I}_{12} \hat{I} \sum_{L_{12}LS\mathcal{J}} (-)^{L_{12}+L+S+\mathcal{J}} \hat{L}_{12}^2 \hat{L}^2 \hat{S}^2 \hat{\mathcal{J}}^2 \\
&\times \begin{Bmatrix} l_{12} & \mathcal{L}_{12} & L_{12} \\ l_c & L & \mathcal{J} \end{Bmatrix} \begin{Bmatrix} l_a & \frac{1}{2} & j_a \\ l_b & \frac{1}{2} & j_b \\ L_{12} & S_{12} & J_{12} \end{Bmatrix} \begin{Bmatrix} L_{12} & S_{12} & J_{12} \\ l_c & \frac{1}{2} & j_c \\ L & S & J \end{Bmatrix} \\
&\times \sum_{\mathcal{N}_{12}\mathcal{L}_{12}} \langle\langle \mathcal{N}_{12}\mathcal{L}_{12}n_{12}l_{12}, L_{12} | n_a l_a n_b l_b, L_{12} \rangle\rangle_{d_1} \langle\langle \mathcal{N}\mathcal{L}nl, \mathcal{J} | \mathcal{N}_{12}\mathcal{L}_{12}n_c l_c, \mathcal{J} \rangle\rangle_{d_2} \\
&\times \sum_{\mathcal{K}} \hat{\mathcal{K}}^2 \begin{Bmatrix} \mathcal{L} & l & \mathcal{J} \\ l_{12} & L & \mathcal{K} \end{Bmatrix} \begin{Bmatrix} \mathcal{L} & \mathcal{K} & L \\ S & J & \mathcal{I} \end{Bmatrix} \begin{Bmatrix} l_{12} & l & \mathcal{K} \\ S_{12} & \frac{1}{2} & S \\ I_{12} & I & \mathcal{I} \end{Bmatrix}. \tag{104}
\end{aligned}$$

Note that Eq. 104 can be simplified by using the 12- j symbol of the first kind [262]. Through diagonalizing the antisymmetrizer, the antisymmetrized Jaobi-HO matrix element is expressed by

$${}_A \langle \kappa'; \mathcal{I}T | V_{3N} | \kappa; \mathcal{I}T \rangle_A = 6 \sum_{\bar{\kappa}\bar{\kappa}'} D_{\kappa\bar{\kappa}}^{(\mathcal{I}T)} D_{\kappa'\bar{\kappa}'}^{(\mathcal{I}T)} \langle \bar{\kappa}'; \mathcal{I}T | V_{3N} | \bar{\kappa}; \mathcal{I}T \rangle. \tag{105}$$

The indices κ , $\bar{\kappa}$, κ' , and $\bar{\kappa}'$, respectively, stand for

$$\kappa = \{n_{12}, l_{12}, S_{12}, I_{12}, T_{12}, n, l, I\} \quad \left((-)^{l_{12}+S_{12}+T_{12}} = -1 \right), \tag{106}$$

$$\bar{\kappa} = \{\bar{n}_{12}, \bar{l}_{12}, \bar{S}_{12}, \bar{I}_{12}, \bar{T}_{12}, \bar{n}, \bar{l}, \bar{I}\} \quad \left((-)^{\bar{l}_{12}+\bar{S}_{12}+\bar{T}_{12}} = -1 \right), \tag{107}$$

$$\kappa' = \{n'_{12}, l'_{12}, S'_{12}, I'_{12}, T'_{12}, n', l', I'\} \quad \left((-)^{l'_{12}+S'_{12}+T'_{12}} = -1 \right), \tag{108}$$

$$\bar{\kappa}' = \{\bar{n}'_{12}, \bar{l}'_{12}, \bar{S}'_{12}, \bar{I}'_{12}, \bar{T}'_{12}, \bar{n}', \bar{l}', \bar{I}'\} \quad \left((-)^{\bar{l}'_{12}+\bar{S}'_{12}+\bar{T}'_{12}} = -1 \right), \tag{109}$$

where $\bar{\kappa}$ and $\bar{\kappa}'$ are the quantum numbers originating from the expansion by Eq. (95).

Once the three-body MEs are obtained withing the JT -coupled scheme by Eq. (103), those within the proton-neutron formalism can be constructed via

$$\begin{aligned}
{}_A \langle (d, e), f; J'_{12}J | V_{3N} | (a, b), c; J_{12}J \rangle_A &= \sum_{TT_{12}T'_{12}} \left(\frac{1}{2} m_{\tau_a} \frac{1}{2} m_{\tau_b} \left| T_{12} M_{T_{12}} \right. \right) \left(T_{12} M_{T_{12}} \frac{1}{2} m_{\tau_c} \left| T M_T \right. \right) \\
&\times \left(\frac{1}{2} m_{\tau_d} \frac{1}{2} m_{\tau_e} \left| T'_{12} M'_{T_{12}} \right. \right) \left(T'_{12} M'_{T_{12}} \frac{1}{2} m_{\tau_f} \left| T M_T \right. \right) \\
&\times {}_A \langle (d, e), f; J'_{12}JT'_{12}T | V_{3N} | (a, b), c; J_{12}JT_{12}T \rangle_A. \tag{110}
\end{aligned}$$

A.3.2 Chiral three-body potentials and nonlocal regularization

The three-nucleon force appears at N²LO of the chiral EFT, as explained in Sec. 2.2. It consists of the two-pion exchange (2PE) term, the one-pion exchange plus the two-body contact (1PE) term, and the three-body contact term, as shown in Fig. 3. In the momentum space, the potential v_{3N} of the operator V_{3N} is explicitly given by Eqs. (1) to (4).

Now we can show that the antisymmetrized three-body MEs can be simplified by

$$\begin{aligned}
{}_A \langle \kappa'; \mathcal{I}T | V_{3N} | \kappa; \mathcal{I}T \rangle_A &= 3 \sum_A \langle \kappa'; \mathcal{I}T | W_{3N} | \kappa; \mathcal{I}T \rangle_A \\
&= 18 \sum_{\bar{\kappa}\bar{\kappa}'} D_{\kappa\bar{\kappa}}^{(\mathcal{I}T)} D_{\kappa'\bar{\kappa}'}^{(\mathcal{I}T)} \langle \bar{\kappa}'; \mathcal{I}T | W_{3N} | \bar{\kappa}; \mathcal{I}T \rangle. \tag{111}
\end{aligned}$$

This is owing to the symmetry of the three-nucleon force with respect to the permutation of particles. In the following sections, the explicit form of $\langle \bar{\mathbf{k}}'; \mathcal{IT} | W_{3N} | \bar{\mathbf{k}}; \mathcal{IT} \rangle$ is presented. The reduced operator W_{3N} is defined by

$$\langle \mathbf{p}'_a, \mathbf{p}'_b, \mathbf{p}'_c | W_{3N} | \mathbf{p}_a, \mathbf{p}_b, \mathbf{p}_c \rangle = w_{3N}(\mathbf{q}_a, \mathbf{q}_b, \mathbf{q}_c) \delta(\mathbf{q}_a + \mathbf{q}_b + \mathbf{q}_c), \quad (112)$$

$$w_{3N}(\mathbf{q}_a, \mathbf{q}_b, \mathbf{q}_c) = w_{3N}^{(2\pi)}(\mathbf{q}_a, \mathbf{q}_b, \mathbf{q}_c) + w_{3N}^{(1\pi)}(\mathbf{q}_a, \mathbf{q}_b, \mathbf{q}_c) + w_{3N}^{(\text{ct})}(\mathbf{q}_a, \mathbf{q}_b, \mathbf{q}_c). \quad (113)$$

The two-pion exchange potential $w_{3N}^{(2\pi)}$ is given by

$$w_{3N}^{(2\pi)}(\mathbf{q}_a, \mathbf{q}_b, \mathbf{q}_c) = w_{3N}^{(2\pi; c_1)}(\mathbf{q}_a, \mathbf{q}_b, \mathbf{q}_c) + w_{3N}^{(2\pi; c_3)}(\mathbf{q}_a, \mathbf{q}_b, \mathbf{q}_c) + w_{3N}^{(2\pi; c_4)}(\mathbf{q}_a, \mathbf{q}_b, \mathbf{q}_c), \quad (114)$$

$$w_{3N}^{(2\pi; c_1)}(\mathbf{q}_a, \mathbf{q}_b, \mathbf{q}_c) = -\frac{1}{(2\pi)^6} \frac{g_A^2 c_1 m_\pi^2}{f_\pi^4} \frac{(\boldsymbol{\sigma}_b \cdot \mathbf{q}_b)(\boldsymbol{\sigma}_c \cdot \mathbf{q}_c)}{(q_b^2 + m_\pi^2)(q_c^2 + m_\pi^2)} \boldsymbol{\tau}_b \cdot \boldsymbol{\tau}_c, \quad (115)$$

$$w_{3N}^{(2\pi; c_3)}(\mathbf{q}_a, \mathbf{q}_b, \mathbf{q}_c) = \frac{1}{(2\pi)^6} \frac{g_A^2 c_3}{2f_\pi^4} \frac{(\boldsymbol{\sigma}_b \cdot \mathbf{q}_b)(\boldsymbol{\sigma}_c \cdot \mathbf{q}_c)}{(q_b^2 + m_\pi^2)(q_c^2 + m_\pi^2)} (\mathbf{q}_b \cdot \mathbf{q}_c) (\boldsymbol{\tau}_b \cdot \boldsymbol{\tau}_c), \quad (116)$$

$$w_{3N}^{(2\pi; c_4)}(\mathbf{q}_a, \mathbf{q}_b, \mathbf{q}_c) = \frac{1}{(2\pi)^6} \frac{g_A^2 c_4}{4f_\pi^4} \frac{(\boldsymbol{\sigma}_b \cdot \mathbf{q}_b)(\boldsymbol{\sigma}_c \cdot \mathbf{q}_c)}{(q_b^2 + m_\pi^2)(q_c^2 + m_\pi^2)} \{(\mathbf{q}_b \times \mathbf{q}_c) \cdot \boldsymbol{\sigma}_a\} \{(\boldsymbol{\tau}_b \times \boldsymbol{\tau}_c) \cdot \boldsymbol{\tau}_a\}, \quad (117)$$

while the other potentials $w_{3N}^{(1\pi)}$ and $w_{3N}^{(\text{ct})}$ are written as

$$w_{3N}^{(1\pi)}(\mathbf{q}_a, \mathbf{q}_b, \mathbf{q}_c) = -\frac{1}{(2\pi)^6} \frac{g_{ACD}}{4f_\pi^4 \Lambda_\chi} \frac{(\boldsymbol{\sigma}_c \cdot \mathbf{q}_c)(\boldsymbol{\sigma}_b \cdot \mathbf{q}_c)}{q_c^2 + m_\pi^2} \boldsymbol{\tau}_b \cdot \boldsymbol{\tau}_c, \quad (118)$$

$$w_{3N}^{(\text{ct})}(\mathbf{q}_a, \mathbf{q}_b, \mathbf{q}_c) = \frac{1}{(2\pi)^6} \frac{c_E}{f_\pi^4 \Lambda_\chi} \boldsymbol{\tau}_a \cdot \boldsymbol{\tau}_b. \quad (119)$$

Note that w_{3N} is one component of Eqs. (1) to (4). Also pay attention that our potential w_{3N} contains a prefactor $1/(2\pi)^6$, which originates from our convention of the normalization: $\langle \mathbf{p}'_a | \mathbf{p}_a \rangle = \delta(\mathbf{q}_a)$. See Refs. [87, 99] for more details.

It is convenient to define the Jacobi-HO momenta as

$$\mathbf{k} = \frac{1}{\sqrt{2}}(\mathbf{p}_a - \mathbf{p}_b), \quad \mathbf{K} = \sqrt{\frac{2}{3}} \left[\frac{1}{2}(\mathbf{p}_a + \mathbf{p}_b) - \mathbf{p}_c \right], \quad \mathbf{K}_0 = \frac{1}{\sqrt{3}}(\mathbf{p}_a + \mathbf{p}_b + \mathbf{p}_c). \quad (120)$$

Then, one finds that the transferred momenta are expressed with the Jacobi-HO momenta:

$$\mathbf{q}_a = \frac{1}{\sqrt{3}}(\mathbf{K}'_0 - \mathbf{K}_0) + \frac{1}{\sqrt{2}}(\mathbf{k}' - \mathbf{k}) + \frac{1}{\sqrt{6}}(\mathbf{K}' - \mathbf{K}), \quad (121)$$

$$\mathbf{q}_b = \frac{1}{\sqrt{3}}(\mathbf{K}'_0 - \mathbf{K}_0) - \frac{1}{\sqrt{2}}(\mathbf{k}' - \mathbf{k}) + \frac{1}{\sqrt{6}}(\mathbf{K}' - \mathbf{K}), \quad (122)$$

$$\mathbf{q}_c = \frac{1}{\sqrt{3}}(\mathbf{K}'_0 - \mathbf{K}_0) - \sqrt{\frac{2}{3}}(\mathbf{K}' - \mathbf{K}). \quad (123)$$

Thus, the operator W_{3N} is given as

$$\begin{aligned} W_{3N} &= \iiint \iiint \iiint dk d\mathbf{K} d\mathbf{K}_0 dk' d\mathbf{K}' d\mathbf{K}'_0 | \mathbf{k}', \mathbf{K}', \mathbf{K}'_0 \rangle \\ &\quad \times w_{3N}(\mathbf{q}_a, \mathbf{q}_b, \mathbf{q}_c) \delta\left(\sqrt{3}[\mathbf{K}'_0 - \mathbf{K}_0]\right) \langle \mathbf{k}, \mathbf{K}, \mathbf{K}_0 | \\ &= \frac{1}{(\sqrt{3})^3} \iiint \iiint dk d\mathbf{K} dk' d\mathbf{K}' | \mathbf{k}', \mathbf{K}' \rangle w_{3N}^{(\text{c.m.})}(\mathbf{q}_a, \mathbf{q}_b, \mathbf{q}_c) \langle \mathbf{k}, \mathbf{K} |. \end{aligned} \quad (124)$$

Here $w_{3N}^{(\text{c.m.})}(\mathbf{q}_a, \mathbf{q}_b, \mathbf{q}_c) = w_{3N}(\mathbf{q}_a, \mathbf{q}_b, \mathbf{q}_c)|_{\mathbf{K}_0 = \mathbf{K}'_0}$. Below we adopt always the condition $\mathbf{K}_0 = \mathbf{K}'_0$, and therefore, we omit the superscript (c.m.) from w_{3N} for simplicity. It should be paid attention that, in Eq. (124), we have the prefactor $1/(\sqrt{3})^3$ originating from the delta function in Eq. (112).

Since the chiral EFT is valid only in the low-momentum region, we introduce the regularization to suppress the high-momentum component of the potential. In our approach, the nonlocal regulator [263] depending on the sum of the Jacobi momenta is employed. Note that, consistently, we employ the chiral two-nucleon potential nonlocally regularized [16, 188]. Moreover, in the nonlocal regularization, there is an advantage over the local regularization that the Fierz rearrangement freedom holds exactly [264–266]. The nonlocal regulator has the form,

$$u_{\nu_0}(k, K, \Lambda_0) = \exp\left[-\left(\frac{k^2 + K^2}{2\Lambda_0^2}\right)^{\nu_0}\right]. \quad (125)$$

The cutoff momentum Λ_0 and the power ν_0 must be fixed consistently with the LECs, c_D and c_E . Thus, the nonlocally regularized potential reads

$$w_{3N}(\mathbf{q}_a, \mathbf{q}_b, \mathbf{q}_c) \rightarrow u_{\nu_0}(k', K', \Lambda_0) w_{3N}(\mathbf{q}_a, \mathbf{q}_b, \mathbf{q}_c) u_{\nu_0}(k, K, \Lambda_0). \quad (126)$$

A.3.3 Contact term

Here, we formulate the Jacobi-HO matrix element $\langle \bar{\kappa}'; \mathcal{I}T | W_{3N}^{(\text{ct})} | \bar{\kappa}; \mathcal{I}T \rangle$ of the contact term. Using (124), we obtain

$$\begin{aligned} & \langle \bar{\kappa}'; \mathcal{I}T | W_{3N}^{(\text{ct})} | \bar{\kappa}; \mathcal{I}T \rangle \\ &= \frac{1}{2\sqrt{3}\pi^4} \frac{c_E}{f_\pi^4 \Lambda_\chi} \delta_{\bar{l}_{12}0} \delta_{\bar{l}'_0} \delta_{\bar{l}'_{12}0} \delta_{\bar{l}'_0} \delta_{\bar{s}_{12}\bar{l}_{12}} \delta_{\bar{s}'_{12}\bar{l}'_{12}} \delta_{\bar{l}'_{12}} \delta_{\bar{l}'_{12}} \delta_{\bar{s}_{12}\bar{s}'_{12}} \delta_{\bar{T}_{12}\bar{T}'_{12}} (-)^{\bar{T}_{12}+1} \begin{Bmatrix} \frac{1}{2} & \frac{1}{2} & \bar{T}_{12} \\ \frac{1}{2} & \frac{1}{2} & 1 \end{Bmatrix} \\ & \times \iint dk dK k K P_{\bar{n}_{12}0}(k) P_{\bar{n}_0}(K) u_{\nu_0}(k, K, \Lambda_0) \\ & \times \iint dk'_1 dK'_1 k'_1 K'_1 P_{\bar{n}'_{12}0}(k'_1) P_{\bar{n}'_0}(K'_1) u_{\nu_0}(k', K', \Lambda_0), \end{aligned} \quad (127)$$

where HO-wave function in the momentum space is written as

$$P_{nl}(k) = \left(\frac{2}{\pi}\right)^{\frac{1}{2}} k \int dr r j_l(kr) R_{nl}(r, b_0) = (-)^n R_{nl}\left(k, \frac{1}{b_0}\right). \quad (128)$$

Here j_l is the spherical Bessel function and we explicitly put the argument b_0 in R_{nl} defined by Eq. (87). The momentum integration in Eq. (127) needs to be carried out numerically.

A.3.4 One-pion exchange plus contact term

The Jacobi-HO matrix element $\langle \bar{\kappa}'; \mathcal{IT} | W_{3N}^{(1\pi)} | \bar{\kappa}; \mathcal{IT} \rangle$ of the 1PE term is slightly complicated:

$$\begin{aligned}
& \langle \bar{\kappa}'; \mathcal{IT} | W_{3N}^{(1\pi)} | \bar{\kappa}; \mathcal{IT} \rangle \\
&= \frac{\sqrt{3}}{4\pi^4} \frac{g_{ACD}}{f_\pi^4 \Lambda_\chi} \delta_{\bar{l}_{12}0} \delta_{\bar{l}'_{12}0} \delta_{\bar{s}_{12}\bar{l}_{12}} \delta_{\bar{s}'_{12}\bar{l}'_{12}} i^{\bar{l}+\bar{l}'} (-)^{\bar{l}+\bar{l}'+\mathcal{I}+T+\frac{1}{2}} \hat{S}_{12} \hat{S}'_{12} \hat{I} \hat{I}' \hat{T}_{12} \hat{T}'_{12} \\
&\times \begin{Bmatrix} \bar{T}_{12} & \bar{T}'_{12} & 1 \\ \frac{1}{2} & \frac{1}{2} & \frac{1}{2} \end{Bmatrix} \begin{Bmatrix} \bar{T}_{12} & \bar{T}'_{12} & 1 \\ \frac{1}{2} & \frac{1}{2} & T \end{Bmatrix} \begin{Bmatrix} \bar{S}_{12} & \bar{S}'_{12} & 1 \\ \frac{1}{2} & \frac{1}{2} & \frac{1}{2} \end{Bmatrix} \begin{Bmatrix} \bar{S}_{12} & \bar{S}'_{12} & 1 \\ \bar{I}' & \bar{I} & \mathcal{I} \end{Bmatrix} \\
&\times \sum_{\lambda_0 \lambda_1 \lambda_2} \hat{\lambda}_0 \widehat{\lambda_0 - \lambda_1} \begin{pmatrix} 2\lambda_0 + 1 \\ 2\lambda_1 \end{pmatrix}^{\frac{1}{2}} (1010|\lambda_0 0) (\lambda_0 - \lambda_1, 0\lambda_2 0|\bar{l}0) (\lambda_1 0\lambda_2 0|\bar{l}'0) \\
&\times \begin{Bmatrix} \lambda_0 - \lambda_1 & \lambda_1 & \lambda_0 \\ \bar{l}' & \bar{l} & \lambda_2 \end{Bmatrix} \begin{Bmatrix} \frac{1}{2} & \bar{l}' & \bar{I}' \\ \frac{1}{2} & \bar{l} & \bar{I} \\ 1 & \lambda_0 & 1 \end{Bmatrix} \\
&\times \iiint\!\!\!\int dk dk' dK dK' k k' K^{\lambda_0 - \lambda_1 + 1} K'^{\lambda_1 + 1} f_{\lambda_2}^{(\lambda_0)}(K, K') \\
&\times P_{\bar{n}_{12}0}(k) P_{\bar{n}'_{12}0}(k') P_{\bar{n}\bar{l}}(K) P_{\bar{n}'\bar{l}'}(K') u_{\nu_0}(k, K, \Lambda_0) u_{\nu_0}(k', K', \Lambda_0), \tag{129}
\end{aligned}$$

with the binomial coefficient $\binom{n_1}{n_2} = n_1! / [(n_1 - n_2)! n_2!]$. The function $f_{\lambda_2}^{(\lambda_0)}$ originating from the multipole expansion of the propagator, together with the factor $(2/3)^{\lambda_0/2} q_c^{2-\lambda_0}$ coming from $(\boldsymbol{\sigma}_c \cdot \mathbf{q}_c) (\boldsymbol{\sigma}_b \cdot \mathbf{q}_c)$ is given by

$$f_{\lambda_2}^{(\lambda_0)}(K, K') = \frac{\hat{\lambda}_2^2}{2} \int_{-1}^1 dw P_{\lambda_2}(w) \frac{\left(\frac{2}{3}\right)^{\frac{\lambda_0}{2}} q_c^{2-\lambda_0}}{q_c^2 + m_\pi^2}, \tag{130}$$

where P_{λ_2} is the Legendre polynomial as a function of $w = \cos \theta$ with the angle θ between \mathbf{K} and \mathbf{K}' .

A.3.5 Two-pion exchange term

The 2PE potentials given by Eqs. (115) to (117) depend on two momenta, \mathbf{q}_b and \mathbf{q}_c , which make the matrix elements cumbersome. After some manipulations, one can derive the Jacobi-HO matrix elements

$$\begin{aligned}
& \langle \bar{\kappa}' ; \mathcal{I}T \mid W_{3N}^{(2\pi; c_1)} \mid \bar{\kappa} ; \mathcal{I}T \rangle \\
&= 3c_1 m_\pi^2 S_{\bar{\kappa}\bar{\kappa}'}^{\mathcal{I}T} \begin{Bmatrix} \bar{S}_{12} & \bar{S}'_{12} & 1 \\ \frac{1}{2} & \frac{1}{2} & \frac{1}{2} \end{Bmatrix} \begin{Bmatrix} \bar{T}_{12} & \bar{T}'_{12} & 1 \\ \frac{1}{2} & \frac{1}{2} & \frac{1}{2} \end{Bmatrix} \\
&\times \sum_{\substack{\lambda_b \lambda_c \\ \lambda'_b \lambda'_c}} (-)^{\lambda_b+1} \sum_{\substack{\lambda_1 \lambda_2 \lambda_3 \\ \lambda'_1 \lambda'_2 \lambda'_3}} I_{\bar{n}_{12} \bar{l}_{12} \bar{n}'_{12} \bar{l}'_{12} \bar{n}'_{12} \bar{l}'_{12}}{}^{\nu_0 \lambda_b \lambda_c \lambda'_b \lambda'_c \lambda_1 \lambda_2 \lambda_3 \lambda'_1 \lambda'_2 \lambda'_3} (\Lambda_0) \\
&\times \sum_{l_1} (-)^{l_1} \hat{l}_1^2 X_{\bar{\kappa}\bar{\kappa}' \mathcal{I}, L_0=1, L'_b=1, L'_c=1, l_0=\lambda_b, l_1}{}^{\lambda_b \lambda_c \lambda'_b \lambda'_c \lambda_1 \lambda_2 \lambda_3 \lambda'_1 \lambda'_2 \lambda'_3}
\end{aligned} \tag{131}$$

$$\begin{aligned}
& \langle \bar{\kappa}' ; \mathcal{I}T \mid W_{3N}^{(2\pi; c_3)} \mid \bar{\kappa} ; \mathcal{I}T \rangle \\
&= \frac{\sqrt{3}}{2} c_3 S_{\bar{\kappa}\bar{\kappa}'}^{\mathcal{I}T} \begin{Bmatrix} \bar{S}_{12} & \bar{S}'_{12} & 1 \\ \frac{1}{2} & \frac{1}{2} & \frac{1}{2} \end{Bmatrix} \begin{Bmatrix} \bar{T}_{12} & \bar{T}'_{12} & 1 \\ \frac{1}{2} & \frac{1}{2} & \frac{1}{2} \end{Bmatrix} \\
&\times \sum_{L_b L_c} \hat{L}_b \hat{L}_c (1010|L_b 0) (1010|L_c 0) \sum_{\substack{\lambda_b \lambda_c \\ \lambda'_b \lambda'_c}} \sum_{\substack{\lambda_1 \lambda_2 \lambda_3 \\ \lambda'_1 \lambda'_2 \lambda'_3}} I_{\bar{n}_{12} \bar{l}_{12} \bar{n}'_{12} \bar{l}'_{12} \bar{n}'_{12} \bar{l}'_{12}}{}^{\nu_0 \lambda_b \lambda_c \lambda'_b \lambda'_c \lambda_1 \lambda_2 \lambda_3 \lambda'_1 \lambda'_2 \lambda'_3} (\Lambda_0) \\
&\times \sum_{l_0 l_1} \hat{l}_0^2 \hat{l}_1^2 \begin{Bmatrix} L_b - \lambda_b & \lambda_b & L_b \\ 1 & 1 & l_0 \end{Bmatrix} \begin{Bmatrix} l_0 & l_1 & 1 \\ L_c & 1 & \lambda_b \end{Bmatrix} X_{\bar{\kappa}\bar{\kappa}' \mathcal{I}, L_0=1, L'_b=L_b, L'_c=L_c, l_0 l_1}{}^{\lambda_b \lambda_c \lambda'_b \lambda'_c \lambda_1 \lambda_2 \lambda_3 \lambda'_1 \lambda'_2 \lambda'_3},
\end{aligned} \tag{132}$$

$$\begin{aligned}
& \langle \bar{\kappa}' ; \mathcal{I}T \mid W_{3N}^{(2\pi; c_4)} \mid \bar{\kappa} ; \mathcal{I}T \rangle \\
&= 9\sqrt{3} c_4 (-)^{\bar{l}_{12}+1} S_{\bar{\kappa}\bar{\kappa}'}^{\mathcal{I}T} \begin{Bmatrix} \frac{1}{2} & \frac{1}{2} & \bar{T}'_{12} \\ \frac{1}{2} & \frac{1}{2} & \bar{T}_{12} \\ 1 & 1 & 1 \end{Bmatrix} \\
&\times \sum_{L_0 L_b L_c} \hat{L}_0 \hat{L}_b \hat{L}_c (1010|L_b 0) (1010|L_c 0) \begin{Bmatrix} L_0 & L_b & 1 \\ 1 & 1 & 1 \end{Bmatrix} \begin{Bmatrix} \frac{1}{2} & \frac{1}{2} & \bar{S}'_{12} \\ \frac{1}{2} & \frac{1}{2} & \bar{S}_{12} \\ 1 & 1 & L_0 \end{Bmatrix} \\
&\times \sum_{\substack{\lambda_b \lambda_c \\ \lambda'_b \lambda'_c}} \sum_{\substack{\lambda_1 \lambda_2 \lambda_3 \\ \lambda'_1 \lambda'_2 \lambda'_3}} I_{\bar{n}_{12} \bar{l}_{12} \bar{n}'_{12} \bar{l}'_{12} \bar{n}'_{12} \bar{l}'_{12}}{}^{\nu_0 \lambda_b \lambda_c \lambda'_b \lambda'_c \lambda_1 \lambda_2 \lambda_3 \lambda'_1 \lambda'_2 \lambda'_3} (\Lambda_0) \\
&\times \sum_{l_0 l_1} \hat{l}_0^2 \hat{l}_1^2 \begin{Bmatrix} L_b - \lambda_b & \lambda_b & L_b \\ 1 & L_0 & l_0 \end{Bmatrix} \begin{Bmatrix} l_0 & l_1 & 1 \\ L_c & 1 & \lambda_b \end{Bmatrix} X_{\bar{\kappa}\bar{\kappa}' \mathcal{I}, L_0 L'_b=L_b, L'_c=L_c, l_0 l_1}{}^{\lambda_b \lambda_c \lambda'_b \lambda'_c \lambda_1 \lambda_2 \lambda_3 \lambda'_1 \lambda'_2 \lambda'_3}.
\end{aligned} \tag{133}$$

The coefficients involved in Eqs. (131) to (133) are defined by

$$S_{\bar{\kappa}\bar{\kappa}'}^{\mathcal{I}T} = \left[\frac{g_A}{(\pi f_\pi)^2} \right]^2 i^{\bar{l}_{12}+\bar{l}'_{12}+\bar{l}+\bar{l}'} (-)^{\bar{S}_{12}+\bar{l}'_{12}-\bar{l}+\mathcal{I}+\bar{T}_{12}+\bar{T}'_{12}+T+\frac{1}{2}} \hat{S}_{12} \hat{S}'_{12} \hat{I}_{12} \hat{I}'_{12} \hat{I} \hat{I}' \hat{T}_{12} \hat{T}'_{12} \begin{Bmatrix} \bar{T}_{12} & \bar{T}'_{12} & 1 \\ \frac{1}{2} & \frac{1}{2} & T \end{Bmatrix}, \tag{134}$$

$$\begin{aligned}
& I^{\nu_0 \lambda_b \lambda_c \lambda'_b \lambda''_b \lambda_1 \lambda_2 \lambda_3 \lambda'_3 \lambda''_3}(\Lambda_0) \\
&= 3^{-\frac{\lambda_b}{2}} (-)^{\lambda_b + \lambda_c + \lambda'_b + \lambda''_b + \lambda_1 + \lambda_2 + \lambda_3 + \lambda'_3 + \lambda''_3} \widehat{L'_b - \lambda_b L'_c - \lambda_c L'_b - \lambda_b - \lambda'_b \lambda_b - \lambda''_b \lambda_3 - \lambda'_3 \lambda_3 - \lambda''_3} \\
&\times \left[\binom{2L'_b + 1}{2\lambda_b} \binom{2L'_c + 1}{2\lambda_c} \binom{2(L'_b - \lambda_b) + 1}{2\lambda'_b} \binom{2\lambda_b + 1}{2\lambda''_b} \binom{2\lambda_3 + 1}{2\lambda'_3} \binom{2\lambda_3 + 1}{2\lambda''_3} \right]^{\frac{1}{2}} \\
&\times \iiint\!\!\!\int dk dK dk' dK' k^{L'_b - \lambda_b - \lambda'_b + \lambda_3 - \lambda'_3 + 1} K^{L'_c - \lambda_c + \lambda_b - \lambda'_b + \lambda_3 - \lambda'_3 + 1} k'^{\lambda'_b + \lambda'_3 + 1} K'^{\lambda_c + \lambda'_b + \lambda'_3 + 1} \\
&\times f_{\lambda_1 \lambda_2 \lambda_3}^{(L_b L_c)}(k, k', K, K') P_{\bar{n}_{12} \bar{l}_{12}}(k) P_{\bar{n} \bar{l}}(K) P_{\bar{n}'_{12} \bar{l}'_{12}}(k') P_{\bar{n}' \bar{l}'}(K') u_{\nu_0}(k, K, \Lambda_0) u_{\nu_0}(k', K', \Lambda_0), \quad (135)
\end{aligned}$$

$$\begin{aligned}
& X_{\bar{\kappa} \bar{\kappa}' \mathcal{L} L_0 L'_b L'_c l_0 l_1}^{\lambda_b \lambda_c \lambda'_b \lambda''_b \lambda_1 \lambda_2 \lambda_3 \lambda'_3 \lambda''_3} \\
&= \sum_{l_2 l_3} \hat{l}_2 \hat{l}_3 (L'_c - \lambda_c, 0, \lambda_b - \lambda'_b, 0 | l_2 0) (\lambda_c 0 \lambda''_b 0 | l_3 0) \begin{Bmatrix} \lambda_b - \lambda'_b & \lambda''_b & \lambda_b \\ L'_c - \lambda_c & \lambda_c & L'_c \\ l_2 & l_3 & l_1 \end{Bmatrix} \\
&\times \sum_{\frac{\lambda \lambda'}{\Lambda \Lambda'}} \hat{\lambda} \hat{\lambda}' \hat{\Lambda} \hat{\Lambda}' (L'_b - \lambda_b - \lambda'_b, 0 \lambda 0 | \bar{l}_{12} 0) (\lambda'_b 0 \lambda' 0 | \bar{l}'_{12} 0) (l_2 0 \Lambda 0 | \bar{l} 0) (l_3 0 \Lambda' 0 | \bar{l}' 0) \\
&\times (\lambda_2 0, \lambda_3 - \lambda'_3, 0 | \lambda 0) (\lambda_2 0 \lambda'_3 0 | \lambda' 0) (\lambda_1 0, \lambda_3 - \lambda''_3, 0 | \Lambda 0) (\lambda_1 0 \lambda''_3 0 | \Lambda' 0) \\
&\times \begin{Bmatrix} \lambda_3 - \lambda'_3 & \lambda'_3 & \lambda_3 \\ \lambda' & \lambda & \lambda_2 \end{Bmatrix} \begin{Bmatrix} \lambda_3 - \lambda''_3 & \lambda''_3 & \lambda_3 \\ \Lambda' & \Lambda & \lambda_1 \end{Bmatrix} \\
&\times \sum_{L_1 L_2 L_3} (-)^{L_1 + L_2 + L_3} \hat{L}_1^2 \hat{L}_2^2 \hat{L}_3^2 \begin{Bmatrix} \bar{I}_{12} & \bar{I}'_{12} & L_1 \\ \bar{I}' & \bar{I} & \mathcal{I} \end{Bmatrix} \begin{Bmatrix} L_0 & L'_b - \lambda_b & l_0 \\ \lambda_3 & L_1 & L_2 \end{Bmatrix} \begin{Bmatrix} 1 & l_1 & l_0 \\ \lambda_3 & L_1 & L_3 \end{Bmatrix} \\
&\times \begin{Bmatrix} \bar{S}'_{12} & \bar{l}_{12} & \bar{I}'_{12} \\ \bar{S}_{12} & \bar{l}_{12} & \bar{I}_{12} \\ L_0 & L_2 & L_1 \end{Bmatrix} \begin{Bmatrix} \frac{1}{2} & \bar{l}' & \bar{I}' \\ \frac{1}{2} & \bar{l} & \bar{I} \\ 1 & L_3 & L_1 \end{Bmatrix} \begin{Bmatrix} L'_b - \lambda_b - \lambda'_b & \lambda'_b & L'_b - \lambda_b \\ \lambda & \lambda' & \lambda_3 \\ \bar{l}_{12} & \bar{l}'_{12} & L_2 \end{Bmatrix} \begin{Bmatrix} l_2 & l_3 & l_1 \\ \Lambda & \Lambda' & \lambda_3 \\ \bar{l} & \bar{l}' & L_3 \end{Bmatrix}, \quad (136)
\end{aligned}$$

as well as

$$\begin{aligned}
f_{\lambda_1 \lambda_2 \lambda_3}^{(L_b L_c)}(k, k', K, K') &= \frac{\hat{\lambda}_1^2 \hat{\lambda}_2^2 \hat{\lambda}_3^2}{8} \int_{-1}^1 \int_{-1}^1 \int_{-1}^1 dw_1 dw_2 dw_3 P_{\lambda_1}(w_1) P_{\lambda_2}(w_2) P_{\lambda_3}(w_3) \\
&\times (|\mathbf{k} - \mathbf{k}'| |\mathbf{K} - \mathbf{K}'|)^{-\lambda_3} \frac{2^{-\frac{L_b}{2}} \left(\frac{2}{3}\right)^{\frac{L_c}{2}} q_b^{2-L_b} q_c^{2-L_c}}{(q_b^2 + m_\pi^2) (q_c^2 + m_\pi^2)}, \quad (137)
\end{aligned}$$

which originates from the triple-fold multipole expansion with respect to $w_1 = \cos \theta_1$, $w_2 = \cos \theta_2$, and $w_3 = \cos \theta_3$ respectively defined by the angles θ_1 , θ_2 , and θ_3 between \mathbf{K} and \mathbf{K}' , \mathbf{k} and \mathbf{k}' , and $\mathbf{K} - \mathbf{K}'$ and $\mathbf{k} - \mathbf{k}'$.

References

- [1] H. Primakoff, T. Holstein, Phys. Rev. 55 (1939) 1218.
- [2] J. L. Friar, B. F. Gibson, G. L. Payne, Annu. Rev. Nucl. Part. Sci. 34 (1984) 403.
- [3] R. Machleidt, Adv. Nucl. Phys. 19 (1989) 189.
- [4] R. B. Wiringa, V. G. J. Stoks, R. Schiavilla, Phys. Rev. C 51 (1995) 38.

- [5] R. Machleidt, Phys. Rev. C 63 (2001) 024001.
- [6] B. R. Barrett, P. Navrátil, J. P. Vary, Prog. Part. Nucl. Phys. 69 (2013) 131.
- [7] J. Carlson, S. Gandolfi, F. Pederiva, S. C. Pieper, R. Schiavilla, K. E. Schmidt, R. B. Wiringa, Rev. Mod. Phys. 87 (2015) 1067.
- [8] B. S. Pudliner, V. R. Pandharipande, J. Carlson, S. C. Pieper, R. B. Wiringa, Phys. Rev. C 56 (1997) 1720.
- [9] S. Weinberg, Physica A 96 (1979) 327.
- [10] S. Weinberg, Phys. Lett. B 251 (1990) 288.
- [11] S. Weinberg, Nucl. Phys. B 363 (1991) 3.
- [12] I. Tews, Z. Davoudi, A. Ekström, J. D. Holt, J. E. Lynn, Journal of Physics G: Nuclear and Particle Physics 47 (2020) 103001.
- [13] C. Drischler, W. Haxton, K. McElvain, E. Mereghetti, A. Nicholson, P. Vranas, A. Walker-Loud, Prog. Part. Nucl. Phys. 121 (2021) 103888.
- [14] S. Weinberg, Phys. Lett. B 295 (1992) 114.
- [15] U. van Kolck, Phys. Rev. C 49 (1994) 2932.
- [16] R. Machleidt, D. R. Entem, Phys. Rep. 503 (2011) 1.
- [17] E. Epelbaum, H. Krebs, P. Reinert, Frontiers in Physics 8 (2020) 98.
- [18] P. Navrátil, Few-Body Syst. 41 (2007) 117.
- [19] S. Quaglioni, P. Navrátil, Phys. Lett. B 652 (2007) 370.
- [20] G. Hupin, J. Langhammer, P. Navrátil, S. Quaglioni, A. Calci, R. Roth, Phys. Rev. C 88 (2013) 054622.
- [21] G. Hagen, T. Papenbrock, D. J. Dean, A. Schwenk, A. Nogga, M. Włoch, P. Piecuch, Phys. Rev. C 76 (2007) 034302.
- [22] G. C. Wick, Phys. Rev. 80 (1950) 268.
- [23] K. Hebeler, Phys. Rep. 890 (2021) 1.
- [24] R. Roth, S. Binder, K. Vobig, A. Calci, J. Langhammer, P. Navrátil, Phys. Rev. Lett. 109 (2012) 052501.
- [25] J. D. Holt, J. Menéndez, J. Simonis, A. Schwenk, Phys. Rev. C 90 (2014) 024312.
- [26] E. Gebrerufael, A. Calci, R. Roth, Phys. Rev. C 93 (2016) 031301.
- [27] G. Hagen, D. J. Dean, M. Hjorth-Jensen, T. Papenbrock, A. Schwenk, Phys. Rev. C 76 (2007) 044305.
- [28] A. Carbone, A. Cipollone, C. Barbieri, A. Rios, A. Polls, Phys. Rev. C 88 (2013) 054326.
- [29] A. Cipollone, C. Barbieri, P. Navrátil, Phys. Rev. Lett. 111 (2013) 062501.

- [30] H. Hergert, S. K. Bogner, S. Binder, A. Calci, J. Langhammer, R. Roth, A. Schwenk, *Phys. Rev. C* 87 (2013) 034307.
- [31] V. Somà, A. Cipollone, C. Barbieri, P. Navrátil, T. Duguet, *Phys. Rev. C* 89 (2014) 061301.
- [32] A. Ekström, G. R. Jansen, K. A. Wendt, G. Hagen, T. Papenbrock, B. D. Carlsson, C. Forssén, M. Hjorth-Jensen, P. Navrátil, W. Nazarewicz, *Phys. Rev. C* 91 (2015) 051301.
- [33] V. Somà, P. Navrátil, F. Raimondi, C. Barbieri, T. Duguet, *Phys. Rev. C* 101 (2020) 014318.
- [34] K. Suzuki, S. Y. Lee, *Prog. Theor. Phys.* 64 (1980) 2091.
- [35] T. T. S. Kuo, F. Krmpotić, K. Suzuki, R. Okamoto, *Nucl. Phys. A* 582 (1995) 205.
- [36] M. Hjorth-Jensen, T. T. S. Kuo, E. Osnes, *Phys. Rep.* 261 (1995) 125.
- [37] S. R. Stroberg, H. Hergert, S. K. Bogner, J. D. Holt, *Annu. Rev. Nucl. Part. Sci.* 69 (2019) 307.
- [38] L. Coraggio, N. Itaco, *Frontiers in Physics* 8 (2020) 345.
- [39] S. Cohen, D. Kurath, *Nucl. Phys.* 73 (1965) 1.
- [40] B. A. Brown, B. H. Wildenthal, *Annu. Rev. Nucl. Part. Sci.* 38 (1988) 29.
- [41] E. Caurier, G. Martínez-Pinedo, F. Nowacki, A. Poves, A. P. Zuker, *Rev. Mod. Phys.* 77 (2005) 427.
- [42] T. T. S. Kuo, G. E. Brown, *Nucl. Phys.* 85 (1966) 40.
- [43] T. T. S. Kuo, G. E. Brown, *Nucl. Phys. A* 114 (1968) 241.
- [44] E. Caurier, A. P. Zuker, A. Poves, G. Martínez-Pinedo, *Phys. Rev. C* 50 (1994) 225.
- [45] J. Duffo, A. P. Zuker, *Phys. Rev. C* 59 (1999) R2347.
- [46] A. P. Zuker, *Phys. Scr. T88* (2000) 157.
- [47] A. P. Zuker, *Phys. Rev. Lett.* 90 (2003) 042502.
- [48] P. Navrátil, W. E. Ormand, *Phys. Rev. Lett.* 88 (2002) 152502.
- [49] M. G. Mayer, *Phys. Rev.* 75 (1949) 1969.
- [50] O. Haxel, J. H. D. Jensen, H. E. Suess, *Phys. Rev.* 75 (1949) 1766.
- [51] M. G. Mayer, J. H. D. Jensen, *Elementary Theory of Nuclear Shell Structure*, John Wiley, New York, 1955.
- [52] T. Otsuka, T. Suzuki, J. D. Holt, A. Schwenk, Y. Akaishi, *Phys. Rev. Lett.* 105 (2010) 032501.
- [53] R. V. F. Janssens, *Nature* 459 (2009) 1069.
- [54] R. Kanungo, C. Nociforo, A. Prochazka, T. Aumann, D. Boutin, D. Cortina-Gil, B. Davids, M. Diakaki, F. Farinon, H. Geissel, R. Gernhäuser, J. Gerl, R. Janik, B. Jonson, B. Kindler, R. Knöbel, R. Krücken, M. Lantz, H. Lenske, Y. Litvinov, B. Lommel, K. Mahata, P. Maierbeck, A. Musumarra, T. Nilsson, T. Otsuka, C. Perro, C. Scheidenberger, B. Sitar, P. Strmen, B. Sun, I. Szarka, I. Tanihata, Y. Utsuno, H. Weick, M. Winkler, *Phys. Rev. Lett.* 102 (2009) 152501.

- [55] D. R. Entem, R. Machleidt, *Phys. Rev. C* 66 (2002) 014002.
- [56] S. Bogner, T. T. S. Kuo, L. Coraggio, A. Covello, N. Itaco, *Phys. Rev. C* 65 (2002) 051301.
- [57] J. Fujita, H. Miyazawa, *Prog. Theor. Phys.* 17 (1957) 360.
- [58] J. D. Holt, J. Menéndez, A. Schwenk, *Eur. Phys. J. A* 49 (2013) 39.
- [59] K. Hebeler, J. D. Holt, J. Menéndez, A. Schwenk, *Annu. Rev. Nucl. Part. Sci.* 65 (2015) 457.
- [60] J. Simonis, K. Hebeler, J. D. Holt, J. Menéndez, A. Schwenk, *Phys. Rev. C* 93 (2016) 011302.
- [61] J. Simonis, S. R. Stroberg, K. Hebeler, J. D. Holt, A. Schwenk, *Phys. Rev. C* 96 (2017) 014303.
- [62] N. Tsunoda, T. Otsuka, K. Takayanagi, N. Shimizu, T. Suzuki, Y. Utsuno, S. Yoshida, H. Ueno, *Nature* 587 (2020) 66.
- [63] J. D. Holt, T. Otsuka, A. Schwenk, T. Suzuki, *J. Phys. G* 39 (2012) 085111.
- [64] S. K. Bogner, R. J. Furnstahl, R. J. Perry, *Phys. Rev. C* 75 (2007) 061001.
- [65] S. K. Bogner, R. J. Furnstahl, A. Schwenk, *Prog. Part. Nucl. Phys.* 65 (2010) 94.
- [66] G. R. Jansen, J. Engel, G. Hagen, P. Navratil, A. Signoracci, *Phys. Rev. Lett.* 113 (2014) 142502.
- [67] Z. H. Sun, T. D. Morris, G. Hagen, G. R. Jansen, T. Papenbrock, *Phys. Rev. C* 98 (2018) 054320.
- [68] Z. H. Sun, G. Hagen, G. R. Jansen, T. Papenbrock, *Phys. Rev. C* 104 (2021) 064310.
- [69] S. R. Stroberg, A. Calci, H. Hergert, J. D. Holt, S. K. Bogner, R. Roth, A. Schwenk, *Phys. Rev. Lett.* 118 (2017) 032502.
- [70] T. D. Morris, J. Simonis, S. R. Stroberg, C. Stumpf, G. Hagen, J. D. Holt, G. R. Jansen, T. Papenbrock, R. Roth, A. Schwenk, *Phys. Rev. Lett.* 120 (2018) 152503.
- [71] M. Brodeur, A. A. Kwiatkowski, O. M. Drozdowski, C. Andreoiu, D. Burdette, A. Chaudhuri, U. Chowdhury, A. T. Gallant, A. Grossheim, G. Gwinner, H. Heggen, J. D. Holt, R. Klawitter, J. Lassen, K. G. Leach, A. Lennarz, C. Nicoloff, S. Raeder, B. E. Schultz, S. R. Stroberg, A. Teigelhöfer, R. Thompson, M. Wieser, J. Dilling, *Phys. Rev. C* 96 (2017) 034316.
- [72] A. B. Garnsworthy, M. Bowry, B. Olaizola, J. D. Holt, S. R. Stroberg, S. Cruz, S. Georges, G. Hackman, A. D. MacLean, J. Measures, H. P. Patel, C. J. Pearson, C. E. Svensson, *Phys. Rev. C* 96 (2017) 044329.
- [73] M. P. Reiter, K. G. Leach, O. M. Drozdowski, S. R. Stroberg, J. D. Holt, C. Andreoiu, C. Babcock, B. Barquest, M. Brodeur, A. Finlay, M. Foster, A. T. Gallant, G. Gwinner, R. Klawitter, B. Kootte, A. A. Kwiatkowski, Y. Lan, D. Lascar, E. Leistenschneider, A. Lennarz, S. Paul, R. Steinbrügge, R. I. Thompson, M. Wieser, J. Dilling, *Phys. Rev. C* 96 (2017) 052501.
- [74] D. Steppenbeck, S. Takeuchi, N. Aoi, P. Doornenbal, M. Matsushita, H. Wang, H. Baba, S. Go, J. D. Holt, J. Lee, K. Matsui, S. Michimasa, T. Motobayashi, D. Nishimura, T. Otsuka, H. Sakurai, Y. Shiga, P.-A. Söderström, S. R. Stroberg, T. Sumikama, R. Taniuchi, J. A. Tostevin, Y. Utsuno, J. J. Valiente-Dobón, K. Yoneda, *Phys. Rev. C* 96 (2017) 064310.

- [75] J. Henderson, G. Hackman, P. Ruotsalainen, S. Stroberg, K. Launey, J. Holt, F. Ali, N. Bernier, M. Bentley, M. Bowry, R. Caballero-Folch, L. Evitts, R. Frederick, A. Garnsworthy, P. Garrett, B. Jigmeddorj, A. Kilic, J. Lassen, J. Measures, D. Muecher, B. Olaizola, E. O'Sullivan, O. Paetkau, J. Park, J. Smallcombe, C. Svensson, R. Wadsworth, C. Wu, *Phys. Lett. B* 782 (2018) 468.
- [76] C. Izzo, G. Bollen, M. Brodeur, M. Eibach, K. Gulyuz, J. D. Holt, J. M. Kelly, M. Redshaw, R. Ringle, R. Sandler, S. Schwarz, S. R. Stroberg, C. S. Sumithrarachchi, A. A. Valverde, A. C. C. Villari, *Phys. Rev. C* 97 (2018) 014309.
- [77] E. Leistenschneider, M. P. Reiter, S. Ayet San Andrés, B. Kootte, J. D. Holt, P. Navrátil, C. Babcock, C. Barbieri, B. R. Barquest, J. Bergmann, J. Bollig, T. Brunner, E. Dunling, A. Finlay, H. Geissel, L. Graham, F. Greiner, H. Hergert, C. Hornung, C. Jesch, R. Klawitter, Y. Lan, D. Lascar, K. G. Leach, W. Lippert, J. E. McKay, S. F. Paul, A. Schwenk, D. Short, J. Simonis, V. Somà, R. Steinbrügge, S. R. Stroberg, R. Thompson, M. E. Wieser, C. Will, M. Yavor, C. Andreoiu, T. Dickel, I. Dillmann, G. Gwinner, W. R. Plass, C. Scheidenberger, A. A. Kwiatkowski, J. Dilling, *Phys. Rev. Lett.* 120 (2018) 062503.
- [78] S. Michimasa, M. Kobayashi, Y. Kiyokawa, S. Ota, D. S. Ahn, H. Baba, G. P. A. Berg, M. Dozono, N. Fukuda, T. Furuno, E. Ideguchi, N. Inabe, T. Kawabata, S. Kawase, K. Kisamori, K. Kobayashi, T. Kubo, Y. Kubota, C. S. Lee, M. Matsushita, H. Miya, A. Mizukami, H. Nagakura, D. Nishimura, H. Oikawa, H. Sakai, Y. Shimizu, A. Stolz, H. Suzuki, M. Takaki, H. Takeda, S. Takeuchi, H. Tokieda, T. Uesaka, K. Yako, Y. Yamaguchi, Y. Yanagisawa, R. Yokoyama, K. Yoshida, S. Shimoura, *Phys. Rev. Lett.* 121 (2018) 022506.
- [79] M. Mougeot, D. Atanasov, K. Blaum, K. Chrysalidis, T. D. Goodacre, D. Fedorov, V. Fedosseev, S. George, F. Herfurth, J. D. Holt, D. Lunney, V. Manea, B. Marsh, D. Neidherr, M. Rosenbusch, S. Rothe, L. Schweikhard, A. Schwenk, C. Seiffert, J. Simonis, S. R. Stroberg, A. Welker, F. Wienholtz, R. N. Wolf, K. Zuber, *Phys. Rev. Lett.* 120 (2018) 232501.
- [80] J. S. Randhawa, R. Kanungo, M. Holl, J. D. Holt, P. Navrátil, S. R. Stroberg, G. Hagen, G. R. Jansen, M. Alcorta, C. Andreoiu, C. Barnes, C. Burbadge, D. Burke, A. A. Chen, A. Chester, G. Christian, S. Cruz, B. Davids, J. Even, G. Hackman, J. Henderson, S. Ishimoto, P. Jassal, S. Kaur, M. Keefe, D. Kisliuk, R. Krücken, J. Liang, J. Lighthall, E. McGee, J. Measures, M. Moukaddam, E. Padilla-Rodal, A. Shotter, I. J. Thompson, J. Turko, M. Williams, O. Workman, *Phys. Rev. C* 99 (2019) 021301.
- [81] H. N. Liu, A. Obertelli, P. Doornenbal, C. A. Bertulani, G. Hagen, J. D. Holt, G. R. Jansen, T. D. Morris, A. Schwenk, R. Stroberg, N. Achouri, H. Baba, F. Browne, D. Calvet, F. Château, S. Chen, N. Chiga, A. Corsi, M. L. Cortés, A. Delbart, J.-M. Gheller, A. Giganon, A. Gillibert, C. Hilaire, T. Isobe, T. Kobayashi, Y. Kubota, V. Lapoux, T. Motobayashi, I. Murray, H. Otsu, V. Panin, N. Paul, W. Rodriguez, H. Sakurai, M. Sasano, D. Steppenbeck, L. Stuhl, Y. L. Sun, Y. Togano, T. Uesaka, K. Wimmer, K. Yoneda, O. Aktas, T. Aumann, L. X. Chung, F. Flavigny, S. Franchoo, I. Gašparić, R.-B. Gerst, J. Gibelin, K. I. Hahn, D. Kim, T. Koiwai, Y. Kondo, P. Koseoglou, J. Lee, C. Lehr, B. D. Linh, T. Lokotko, M. MacCormick, K. Moschner, T. Nakamura, S. Y. Park, D. Rossi, E. Sahin, D. Sohler, P.-A. Söderström, S. Takeuchi, H. Törnqvist, V. Vaquero, V. Wagner, S. Wang, V. Werner, X. Xu, H. Yamada, D. Yan, Z. Yang, M. Yasuda, L. Zanetti, *Phys. Rev. Lett.* 122 (2019) 072502.
- [82] N. Michel, W. Nazarewicz, M. Płoszajczak, K. Bennaceur, *Phys. Rev. Lett.* 89 (2002) 042502.

- [83] N. Michel, W. Nazarewicz, M. Płoszajczak, T. Vertse, *J. Phys. G: Nucl. Part. Phys.* 36 (2009) 013101.
- [84] J. Li, Y. Ma, N. Michel, B. Hu, Z. Sun, W. Zuo, F. Xu, *Physics* 3 (2021) 977.
- [85] U. van Kolck, *Prog. Part. Nucl. Phys.* 43 (1999) 337.
- [86] T. Fukui, L. De Angelis, Y. Z. Ma, L. Coraggio, A. Gargano, N. Itaco, F. R. Xu, *Phys. Rev. C* 98 (2018) 044305.
- [87] P. Navrátil, V. G. Gueorguiev, J. P. Vary, W. E. Ormand, A. Nogga, *Phys. Rev. Lett.* 99 (2007) 042501.
- [88] P. Maris, J. P. Vary, P. Navrátil, *Phys. Rev. C* 87 (2013) 014327.
- [89] Y. Z. Ma, L. Coraggio, L. De Angelis, T. Fukui, A. Gargano, N. Itaco, F. R. Xu, *Phys. Rev. C* 100 (2019) 034324.
- [90] L. Coraggio, G. De Gregorio, A. Gargano, N. Itaco, T. Fukui, Y. Z. Ma, F. R. Xu, *Phys. Rev. C* 102 (2020) 054326.
- [91] L. Coraggio, G. De Gregorio, A. Gargano, N. Itaco, T. Fukui, Y. Z. Ma, F. R. Xu, *Phys. Rev. C* 104 (2021) 054304.
- [92] Y. Ma, F. Xu, L. Coraggio, B. Hu, J. Li, T. Fukui, L. D. Angelis, N. Itaco, A. Gargano, *Phys. Lett. B* 802 (2020) 135257.
- [93] Y. Ma, F. Xu, N. Michel, S. Zhang, J. Li, B. Hu, L. Coraggio, N. Itaco, A. Gargano, *Phys. Lett. B* 808 (2020) 135673.
- [94] S. Zhang, Y. Ma, J. Li, B. Hu, Q. Yuan, Z. Cheng, F. Xu, *Phys. Lett. B* 827 (2022) 136958.
- [95] A. Camsonne, A. T. Katramatou, M. Olson, A. Acha, K. Allada, B. D. Anderson, J. Arrington, A. Baldwin, J.-P. Chen, S. Choi, E. Chudakov, E. Cisbani, B. Craver, P. Decowski, C. Dutta, E. Folts, S. Frullani, F. Garibaldi, R. Gilman, J. Gomez, B. Hahn, J.-O. Hansen, D. W. Higinbotham, T. Holmstrom, J. Huang, M. Iodice, X. Jiang, A. Kelleher, E. Khrosinkova, A. Kievsky, E. Kuchina, G. Kumbartzki, B. Lee, J. J. LeRose, R. A. Lindgren, G. Lott, H. Lu, L. E. Marcucci, D. J. Margaziotis, P. Markowitz, S. Marrone, D. Meekins, Z.-E. Meziani, R. Michaels, B. Moffit, B. Norum, G. G. Petratos, A. Puckett, X. Qian, O. Rondon, A. Saha, B. Sawatzky, J. Segal, M. Shabestari, A. Shahinyan, P. Solvignon, N. Sparveris, R. R. Subedi, R. Suleiman, V. Sulkosky, G. M. Urciuoli, M. Viviani, Y. Wang, B. B. Wojtsekhowski, X. Yan, H. Yao, W.-M. Zhang, X. Zheng, L. Zhu, *Phys. Rev. Lett.* 119 (2017) 162501.
- [96] J. M. Lina, B. Goulard, *Phys. Rev. C* 34 (1986) 714.
- [97] B. Frois, C. N. Papanicolas, *Annu. Rev. Nucl. Part. Sci.* 37 (1987) 133.
- [98] J. Carlson, R. Schiavilla, *Rev. Mod. Phys.* 70 (1998) 743.
- [99] S. A. Coon, W. Glöckle, *Phys. Rev. C* 23 (1981) 1790–1802.
- [100] R. Ellis, S. Coon, B. McKellar, *Nucl. Phys. A* 438 (1985) 631.
- [101] S. A. Coon, M. T. Peña, *Phys. Rev. C* 48 (1993) 2559.

- [102] W. H. Dickhoff, A. Faessler, H. Mütter, Nucl. Phys. A 389 (1982) 492.
- [103] H. Mütter, Prog. Part. Nucl. Phys. 14 (1985) 123.
- [104] F. Sammarruca, B. Chen, L. Coraggio, N. Itaco, R. Machleidt, Phys. Rev. C 86 (2012) 054317.
- [105] E. Epelbaum, W. Glöckle, U.-G. Meissner, Nucl. Phys. A 747 (2005) 362.
- [106] E. Epelbaum, H.-W. Hammer, U.-G. Meissner, Rev. Mod. Phys. 81 (2009) 1773.
- [107] A. Gårdestig, D. R. Phillips, Phys. Rev. Lett. 96 (2006) 232301.
- [108] D. Gazit, Phys. Lett. B 666 (2008) 472.
- [109] L. Coraggio, J. W. Holt, N. Itaco, R. Machleidt, L. E. Marcucci, F. Sammarruca, Phys. Rev. C 89 (2014) 044321.
- [110] L. E. Marcucci, A. Kievsky, S. Rosati, R. Schiavilla, M. Viviani, Phys. Rev. Lett. 108 (2012) 052502.
- [111] S. Ishikawa, M. R. Robilotta, Phys. Rev. C 76 (2007) 014006.
- [112] L. Girlanda, E. Filandri, A. Kievsky, L. E. Marcucci, M. Viviani, arXiv:2302.03468 [nucl-th].
- [113] L. Girlanda, A. Kievsky, M. Viviani, L. E. Marcucci, Phys. Rev. C 99 (2019) 054003.
- [114] H. Witała, J. Golak, R. Skibiński, Phys. Rev. C 105 (2022) 054004.
- [115] I. Talmi, Adv. Nucl. Phys. 27 (2003) 1.
- [116] B. A. Brown, W. Rae, E. McDonald, M. Horoi, Nushellx@msu.
- [117] C. W. Johnson, W. E. Ormand, P. G. Krastev, Computer Physics Communications 184 (2013) 2761.
- [118] N. Shimizu, T. Mizusaki, Y. Utsuno, Y. Tsunoda, Computer Physics Communications 244 (2019) 372.
- [119] M. Shao, H. Aktulga, C. Yang, E. G. Ng, P. Maris, J. P. Vary, Computer Physics Communications 222 (2018) 1–13.
- [120] N. Shimizu, Physics 4 (3) (2022) 1081–1093.
- [121] T. Otsuka, A. Gade, O. Sorlin, T. Suzuki, Y. Utsuno, Rev. Mod. Phys. 92 (2020) 015002.
- [122] K. A. Brueckner, C. A. Levinson, H. M. Mahmoud, Phys. Rev. 95 (1954) 217.
- [123] I. Talmi, Rev. Mod. Phys. 34 (1963) 704.
- [124] B. A. Brown, Prog. Part. Nucl. Phys. 47 (2001) 517.
- [125] B. Alex Brown, The nuclear configuration interactions method, in: J.-E. García-Ramos, M. V. Andrés, J. A. L. Valera, A. M. Moro, F. Pérez-Bernal (Eds.), Basic Concepts in Nuclear Physics: Theory, Experiments and Applications, Springer International Publishing, 2019, pp. 3–31.
- [126] G. E. Brown, J. Holt, Hans bethe: The nuclear many body problem, in: G. E. Brown, C.-H. Lee (Eds.), Hans Bethe and His Physics, World Scientific, Singapore, 2006.

- [127] M. Honma, T. Otsuka, B. A. Brown, T. Mizusaki, *Phys. Rev. C* 69 (2004) 034335.
- [128] M. Honma, T. Otsuka, T. Mizusaki, M. Hjorth-Jensen, *Phys. Rev. C* 80 (2009) 064323.
- [129] A. Poves, A. Zuker, *Phys. Rep.* 70 (1981) 235.
- [130] F. Nowacki, A. Poves, *Phys. Rev. C* 79 (2009) 014310.
- [131] S. M. Lenzi, F. Nowacki, A. Poves, K. Sieja, *Phys. Rev. C* 82 (2010) 054301.
- [132] T. D. Morris, N. M. Parzuchowski, S. K. Bogner, *Phys. Rev. C* 92 (2015) 034331.
- [133] A. F. Lisetskiy, B. R. Barrett, M. K. G. Kruse, P. Navratil, I. Stetcu, J. P. Vary, *Phys. Rev. C* 78 (2008) 044302.
- [134] A. F. Lisetskiy, M. K. G. Kruse, B. R. Barrett, P. Navratil, I. Stetcu, J. P. Vary, *Phys. Rev. C* 80 (2009) 024315.
- [135] E. Dikmen, A. F. Lisetskiy, B. R. Barrett, P. Maris, A. M. Shirokov, J. P. Vary, *Phys. Rev. C* 91 (2015) 064301.
- [136] N. A. Smirnova, B. R. Barrett, Y. Kim, I. J. Shin, A. M. Shirokov, E. Dikmen, P. Maris, J. P. Vary, *Phys. Rev. C* 100 (2019) 054329.
- [137] S. Y. Lee, K. Suzuki, *Phys. Lett. B* 91 (1980) 173.
- [138] K. Takayanagi, *Nucl. Phys. A* 852 (2011) 61.
- [139] K. Suzuki, R. Okamoto, H. Kumagai, S. Fujii, *Phys. Rev. C* 83 (2011) 024304.
- [140] E. M. Krencigłowa, T. T. S. Kuo, *Nucl. Phys. A* 235 (1974) 171.
- [141] B. H. Brandow, *Rev. Mod. Phys.* 39 (1967) 771.
- [142] T. T. S. Kuo, S. Y. Lee, K. F. Ratcliff, *Nucl. Phys. A* 176 (1971) 65.
- [143] J. Shurpin, T. T. S. Kuo, D. Strottman, *Nucl. Phys. A* 408 (1983) 310.
- [144] T. T. S. Kuo, J. Shurpin, K. C. Tam, E. Osnes, P. J. Ellis, *Ann. Phys. (NY)* 132 (1981) 237.
- [145] L. Coraggio, A. Covello, A. Gargano, N. Itaco, T. T. S. Kuo, *Ann. Phys. (NY)* 327 (2012) 2125.
- [146] M. Hjorth-Jensen, M. P. Lombardo, U. van Kolck (Eds.), *Lecture Notes in Physics*, Vol. 936, Springer, Berlin, 2017.
- [147] A. Polls, H. Müther, A. Faessler, T. T. S. Kuo, E. Osnes, *Nucl. Phys. A* 401 (1983) 124.
- [148] P. J. Ellis, E. Osnes, *Rev. Mod. Phys.* 49 (1977) 777.
- [149] H. A. Mavromatis, L. Zamick, G. E. Brown, *Nucl. Phys. A* 80 (1966) 545.
- [150] H. A. Mavromatis, L. Zamick, *Nucl. Phys. A* 104 (1967) 17.
- [151] P. Federman, L. Zamick, *Phys. Rev.* 177 (1969) 1534.
- [152] I. S. Towner, K. F. C. Khanna, *Nucl. Phys. A* 399 (1983) 334.

- [153] I. S. Towner, Phys. Rep. 155 (1987) 263.
- [154] K. Suzuki, R. Okamoto, Prog. Theor. Phys. 93 (1995) 905.
- [155] L. Coraggio, L. De Angelis, T. Fukui, A. Gargano, N. Itaco, J. Phys. Conf. Ser. 1056 (2018) 012012.
- [156] L. Coraggio, L. De Angelis, T. Fukui, A. Gargano, N. Itaco, F. Nowacki, Phys. Rev. C 100 (2019) 014316.
- [157] L. Coraggio, A. Gargano, N. Itaco, R. Mancino, F. Nowacki, Phys. Rev. C 101 (2020) 044315.
- [158] K. Bennaceur, F. Nowacki, J. Okołowicz, M. Płoszajczak, Nucl. Phys. A 651 (1999) 289.
- [159] J. Okołowicz, M. Płoszajczak, I. Rotter, Phys. Rep. 374 (2003) 271.
- [160] J. Rotureau, J. Okołowicz, M. Płoszajczak, Phys. Rev. Lett. 95 (2005) 042503.
- [161] A. Volya, V. Zelevinsky, Phys. Rev. Lett. 94 (2005) 052501.
- [162] K. Tsukiyama, T. Otsuka, R. Fujimoto, Prog. Theor. Exp. Phys. 2015 (2015) 093D01.
- [163] T. Berggren, Nucl. Phys. A 109 (1968) 265.
- [164] R. Id Betan, R. J. Liotta, N. Sandulescu, T. Vertse, Phys. Rev. Lett. 89 (2002) 042501.
- [165] N. Michel, W. Nazarewicz, M. Płoszajczak, J. Okołowicz, Phys. Rev. C 67 (2003) 054311.
- [166] N. Michel, J. G. Li, F. R. Xu, W. Zuo, Phys. Rev. C 100 (2019) 064303.
- [167] G. Papadimitriou, A. T. Kruppa, N. Michel, W. Nazarewicz, M. Płoszajczak, J. Rotureau, Phys. Rev. C 84 (2011) 051304.
- [168] N. Michel, J. G. Li, F. R. Xu, W. Zuo, Phys. Rev. C 101 (2020) 031301.
- [169] J. G. Li, N. Michel, W. Zuo, F. R. Xu, Phys. Rev. C 103 (2021) 034305.
- [170] G. Hagen, M. Hjorth-Jensen, N. Michel, Phys. Rev. C 73 (2006) 064307.
- [171] K. Tsukiyama, M. Hjorth-Jensen, G. Hagen, Phys. Rev. C 80 (2009) 051301(R).
- [172] G. Papadimitriou, J. Rotureau, N. Michel, M. Płoszajczak, B. R. Barrett, Phys. Rev. C 88 (2013) 044318.
- [173] Z. H. Sun, Q. Wu, Z. H. Zhao, B. S. Hu, S. J. Dai, F. R. Xu, Phys. Lett. B 769 (2017) 227.
- [174] B. Hu, Q. Wu, J. Li, Y. Ma, Z. Sun, N. Michel, F. Xu, Phys. Lett. B 802 (2020) 135206.
- [175] J. G. Li, N. Michel, W. Zuo, F. R. Xu, Phys. Rev. C 104 (2021) 024319.
- [176] G. Hagen, D. J. Dean, M. Hjorth-Jensen, T. Papenbrock, Phys. Lett. B 656 (2007) 169.
- [177] G. Hagen, T. Papenbrock, M. Hjorth-Jensen, Phys. Rev. Lett. 104 (2010) 182501.
- [178] G. Hagen, M. Hjorth-Jensen, G. R. Jansen, R. Machleidt, T. Papenbrock, Phys. Rev. Lett. 108 (2012) 242501.

- [179] B. S. Hu, Q. Wu, Z. H. Sun, F. R. Xu, *Phys. Rev. C* 99 (2019) 061302(R).
- [180] J. G. Li, B. S. Hu, Q. Wu, Y. Gao, S. J. Dai, F. R. Xu, *Phys. Rev. C* 102 (2020) 034302.
- [181] K. Takayanagi, *Nucl. Phys. A* 852 (2011) 61.
- [182] N. Michel, H. Aktulga, Y. Jaganathen, *Computer Physics Communications* 247 (2020) 106978.
- [183] D. H. Gloeckner, R. D. Lawson, *Phys. Lett. B* 53 (1974) 313.
- [184] G. Hagen, T. Papenbrock, D. J. Dean, *Phys. Rev. Lett.* 103 (2009) 062503.
- [185] H. Hergert, S. K. Bogner, T. D. Morris, A. Schwenk, K. Tsukiyama, *Phys. Rep.* 621 (2016) 165.
- [186] P. Navrátil, E. Caurier, *Phys. Rev. C* 69 (2004) 014311.
- [187] J. Blomqvist, A. Molinari, *Nucl. Phys. A* 106 (1968) 545.
- [188] D. R. Entem, R. Machleidt, *Phys. Rev. C* 68 (2003) 041001.
- [189] L. Coraggio, A. Covello, A. Gargano, N. Itaco, T. T. S. Kuo, D. R. Entem, R. Machleidt, *Phys. Rev. C* 75 (2007) 024311.
- [190] B. R. Barrett, M. W. Kirson, *Nucl. Phys. A* 148 (1970) 145.
- [191] G. A. Baker, J. L. Gammel, *The Padé Approximant in Theoretical Physics*, Vol. 71 of *Mathematics in Science and Engineering*, Academic Press, New York, 1970.
- [192] N. Ayoub, H. A. Mavromatis, *Nucl. Phys. A* 323 (1979) 125.
- [193] Data extracted using the NNDC On-line Data Service from the ENSDF database, file revised as of February 22, 2023., [link].
- [194] G. Audi, M. Wang, A. H. Wapstra, F. G. Kondev, M. MacCormick, X. Xu, B. Pfeiffer, *Chin. Phys. C* 36 (2012) 1287.
- [195] P. Thirolf, B. Pritychenko, B. Brown, P. Cottle, M. Chromik, T. Glasmacher, G. Hackman, R. Ibbotson, K. Kemper, T. Otsuka, L. Riley, H. Scheit, *Phys. Lett. B* 485 (2000) 16.
- [196] C. R. Hoffman, T. Baumann, D. Bazin, J. Brown, G. Christian, P. A. DeYoung, J. E. Finck, N. Frank, J. Hinnefeld, R. Howes, P. Mears, E. Mosby, S. Mosby, J. Reith, B. Rizzo, W. F. Rogers, G. Peaslee, W. A. Peters, A. Schiller, M. J. Scott, S. L. Tabor, M. Thoennessen, P. J. Voss, T. Williams, *Phys. Rev. Lett.* 100 (2008) 152502.
- [197] C. Hoffman, T. Baumann, D. Bazin, J. Brown, G. Christian, D. Denby, P. DeYoung, J. Finck, N. Frank, J. Hinnefeld, S. Mosby, W. Peters, W. Rogers, A. Schiller, A. Spyrou, M. Scott, S. Tabor, M. Thoennessen, P. Voss, *Phys. Lett. B* 672 (2009) 17.
- [198] M. Thoennessen, *Rep. Prog. Phys.* 67 (2004) 1187.
- [199] C. Caesar, J. Simonis, T. Adachi, Y. Aksyutina, J. Alcantara, S. Altstadt, H. Alvarez-Pol, N. Ashwood, T. Aumann, V. Avdeichikov, M. Barr, S. Beceiro, D. Bemmerer, J. Benlliure, C. A. Bertulani, K. Boretzky, M. J. G. Borge, G. Burgunder, M. Caamano, E. Casarejos, W. Catford, J. Cederkäll, S. Chakraborty, M. Chartier, L. Chulkov, D. Cortina-Gil, U. Datta Pramanik, P. Diaz Fernandez, I. Dillmann, Z. Elekes, J. Enders, O. Ershova, A. Estrade, F. Farinon, L. M.

- Fraille, M. Freer, M. Freudenberger, H. O. U. Fynbo, D. Galaviz, H. Geissel, R. Gernhäuser, P. Golubev, D. Gonzalez Diaz, J. Hagdahl, T. Heftrich, M. Heil, M. Heine, A. Heinz, A. Henriques, M. Holl, J. D. Holt, G. Ickert, A. Ignatov, B. Jakobsson, H. T. Johansson, B. Jonsson, N. Kalantar-Nayestanaki, R. Kanungo, A. Kelic-Heil, R. Knöbel, T. Kröll, R. Krücken, J. Kurcewicz, M. Labiche, C. Langer, T. Le Bleis, R. Lemmon, O. Lepyoshkina, S. Lindberg, J. Machado, J. Marganec, V. Maroussov, J. Menéndez, M. Mostazo, A. Movsesyan, A. Najafi, T. Nilsson, C. Nociforo, V. Panin, A. Perea, S. Pietri, R. Plag, A. Prochazka, A. Rahaman, G. Rastrepina, R. Reifarh, G. Ribeiro, M. V. Ricciardi, C. Rigollet, K. Riisager, M. Röder, D. Rossi, J. Sanchez del Rio, D. Savran, H. Scheit, A. Schwenk, H. Simon, O. Sorlin, V. Stoica, B. Streicher, J. Taylor, O. Tengblad, S. Terashima, R. Thies, Y. Togano, E. Uberseder, J. Van de Walle, P. Velho, V. Volkov, A. Wagner, F. Wamers, H. Weick, M. Weigand, C. Wheldon, G. Wilson, C. Wimmer, J. S. Winfield, P. Woods, D. Yakorev, M. V. Zhukov, A. Zilges, M. Zoric, K. Zuber, *Phys. Rev. C* 88 (2013) 034313.
- [200] E. Lunderberg, P. A. DeYoung, Z. Kohley, H. Attanayake, T. Baumann, D. Bazin, G. Christian, D. Divaratne, S. M. Grimes, A. Haagsma, J. E. Finck, N. Frank, B. Luther, S. Mosby, T. Nagi, G. F. Peaslee, A. Schiller, J. Snyder, A. Spyrou, M. J. Strongman, M. Thoennessen, *Phys. Rev. Lett.* 108 (2012) 142503.
- [201] Y. Utsuno, T. Otsuka, T. Mizusaki, M. Honma, *Phys. Rev. C* 60 (1999) 054315.
- [202] T. Otsuka, R. Fujimoto, Y. Utsuno, B. A. Brown, M. Honma, T. Mizusaki, *Phys. Rev. Lett.* 87 (2001) 082502.
- [203] B. A. Brown, W. A. Richter, *Phys. Rev. C* 72 (2005) 057301.
- [204] Y. Utsuno, T. Otsuka, T. Glasmacher, T. Mizusaki, M. Honma, *Phys. Rev. C* 70 (2004) 044307.
- [205] B. A. Brown, W. A. Richter, *Phys. Rev. C* 74 (2006) 034315.
- [206] Y. Kondo, T. Nakamura, R. Tanaka, R. Minakata, S. Ogoshi, N. A. Orr, N. L. Achouri, T. Aumann, H. Baba, F. Delaunay, P. Doornenbal, N. Fukuda, J. Gibelin, J. W. Hwang, N. Inabe, T. Isobe, D. Kameda, D. Kanno, S. Kim, N. Kobayashi, T. Kobayashi, T. Kubo, S. Leblond, J. Lee, F. M. Marqués, T. Motobayashi, D. Murai, T. Murakami, K. Muto, T. Nakashima, N. Nakatsuka, A. Navin, S. Nishi, H. Otsu, H. Sato, Y. Satou, Y. Shimizu, H. Suzuki, K. Takahashi, H. Takeda, S. Takeuchi, Y. Togano, A. G. Tuff, M. Vandebrouck, K. Yoneda, *Phys. Rev. Lett.* 116 (2016) 102503.
- [207] M. D. Jones, K. Fosse, T. Baumann, P. A. DeYoung, J. E. Finck, N. Frank, A. N. Kuchera, N. Michel, W. Nazarewicz, J. Rotureau, J. K. Smith, S. L. Stephenson, K. Stiefel, M. Thoennessen, R. G. T. Zegers, *Phys. Rev. C* 96 (2017) 054322.
- [208] H. Hergert, S. Binder, A. Calci, J. Langhammer, R. Roth, *Phys. Rev. Lett.* 110 (2013) 242501.
- [209] S. K. Bogner, H. Hergert, J. D. Holt, A. Schwenk, S. Binder, A. Calci, J. Langhammer, R. Roth, *Phys. Rev. Lett.* 113 (2014) 142501.
- [210] J. Dudek, Z. Szymański, T. Werner, *Phys. Rev. C* 23 (1981) 920–925.
- [211] K. Tanaka, M. Fukuda, M. Mihara, M. Takechi, D. Nishimura, T. Chinda, T. Sumikama, S. Kudo, K. Matsuta, T. Minamisono, T. Suzuki, T. Ohtsubo, T. Izumikawa, S. Momota, T. Yamaguchi, T. Onishi, A. Ozawa, I. Tanihata, T. Zheng, *Phys. Rev. C* 82 (2010) 044309.

- [212] P. G. Sharov, A. S. Fomichev, A. A. Bezbakh, V. Chudoba, I. A. Egorova, M. S. Golovkov, T. A. Golubkova, A. V. Gorshkov, L. V. Grigorenko, G. Kaminski, A. G. Knyazev, S. A. Krupko, M. Mentel, E. Y. Nikolskii, Y. L. Parfenova, P. Pluchinski, S. A. Rymzhanova, S. I. Sidorchuk, R. S. Slepnev, S. V. Stepantsov, G. M. Ter-Akopian, R. Wolski, *Phys. Rev. C* 96 (2017) 025807.
- [213] R. J. Charity, K. W. Brown, J. Okołowicz, M. Płoszajczak, J. M. Elson, W. Reviol, L. G. Sobotka, W. W. Buhro, Z. Chajecki, W. G. Lynch, J. Manfredi, R. Shane, R. H. Showalter, M. B. Tsang, D. Weisshaar, J. R. Winkelbauer, S. Bedoor, A. H. Wuosmaa, *Phys. Rev. C* 97 (2018) 054318.
- [214] E. Garrido, D. Fedorov, A. Jensen, *Nucl. Phys. A* 733 (2004) 85.
- [215] J. Casal, E. Garrido, R. de Diego, J. M. Arias, M. Rodríguez-Gallardo, *Phys. Rev. C* 94 (2016) 054622.
- [216] Y. L. Parfenova, L. V. Grigorenko, I. A. Egorova, N. B. Shulgina, J. S. Vaagen, M. V. Zhukov, *Phys. Rev. C* 98 (2018) 034608.
- [217] A. Huck, G. Klotz, A. Knipper, C. Miehé, C. Richard-Serre, G. Walter, A. Poves, H. L. Ravn, G. Marguier, *Phys. Rev. C* 31 (1985) 2226.
- [218] A. Gade, R. V. F. Janssens, D. Bazin, R. Broda, B. A. Brown, C. M. Campbell, M. P. Carpenter, J. M. Cook, A. N. D. D. C. Dinca, B. F. S. J. Freeman, T. Glasmacher, P. G. Hansen, B. P. Kay, P. F. Mantica, W. F. Mueller, J. R. Terry, J. A. Tostevin, S. Zhu, *Phys. Rev. C* 74 (2006) 021302(R).
- [219] F. Wienholtz, D. Beck, K. Blaum, C. Borgmann, M. Breitenfeldt, R. B. Cakirli, S. George, F. Herfurth, J. Holt, M. Kowalska, S. Kreim, D. Lunney, V. Manea, J. Menendez, D. Neidherr, M. Rosenbusch, L. Schweikhard, A. Schwenk, J. Simonis, J. Stanja, R. N. Wolf, K. Zuber, *Nature* 498 (2013) 346.
- [220] D. Steppenbeck, S. Takeuchi, N. Aoi, P. Doornenbal, M. Matsushita, H. Wang, H. Baba, N. Fukuda, S. Go, M. Honma, J. Lee, K. Matsui, S. Michimasa, T. Motobayashi, D. Nishimura, T. Otsuka, H. Sakurai, Y. Shiga, P.-A. Söderström, T. Sumikama, H. Suzuki, R. Taniuchi, Y. Utsuno, J. J. Valiente-Dobon, K. Yoneda, *Nature* 502 (2013) 207.
- [221] O. B. Tarasov, D. S. Ahn, D. Bazin, N. Fukuda, A. Gade, M. Hausmann, N. Inabe, S. Ishikawa, N. Iwasa, K. Kawata, T. Komatsubara, T. Kubo, K. Kusaka, D. J. Morrissey, M. Ohtake, H. Otsu, M. Portillo, T. Sakakibara, H. Sakurai, H. Sato, B. M. Sherrill, Y. Shimizu, A. Stolz, T. Sumikama, H. Suzuki, H. Takeda, M. Thoennessen, H. Ueno, Y. Yanagisawa, K. Yoshida, *Phys. Rev. Lett.* 121 (2018) 022501.
- [222] J. Meng, H. Toki, J. Y. Zeng, S. Q. Zhang, S.-G. Zhou, *Phys. Rev. C* 65 (2002) 041302.
- [223] G. Hagen, M. Hjorth-Jensen, G. R. Jansen, R. Machleidt, T. Papenbrock, *Phys. Rev. Lett.* 109 (2012) 032502.
- [224] H. Hergert, S. K. Bogner, T. D. Morris, S. Binder, A. Calci, J. Langhammer, R. Roth, *Phys. Rev. C* 90 (2014) 041302.
- [225] S. Fayans, S. Tolokonnikov, D. Zawischa, *Phys. Lett. B* 491 (2000) 245.
- [226] M. Bhattacharya, G. Gangopadhyay, *Phys. Rev. C* 72 (2005) 044318.
- [227] W.-C. Chen, J. Piekarewicz, *Phys. Lett. B* 748 (2015) 284.

- [228] L. Neufcourt, Y. Cao, W. Nazarewicz, E. Olsen, F. Viens, *Phys. Rev. Lett.* 122 (2019) 062502.
- [229] X.-N. Cao, Q. Liu, Z.-M. Niu, J.-Y. Guo, *Phys. Rev. C* 99 (2019) 024314.
- [230] J. G. Li, B. S. Hu, Q. Wu, Y. Gao, S. J. Dai, F. R. Xu, *Phys. Rev. C* 102 (2020) 034302.
- [231] P. Klüpfel, P.-G. Reinhard, T. J. Bürvenich, J. A. Maruhn, *Phys. Rev. C* 79 (2009) 034310.
- [232] A. Poves, J. Sánchez-Solano, E. Caurier, F. Nowacki, *Nucl. Phys. A* 694 (2001) 157.
- [233] W. J. Huang, M. Wang, F. Kondev, G. Audi, S. Naimi, *Chinese Physics C* 45 (2021) 030002.
- [234] O. Sorlin, M.-G. Porquet, *Progr. Part. Nucl. Phys.* 61 (2008) 602.
- [235] T. Motobayashi, Y. Ikeda, K. Ieki, M. Inoue, N. Iwasa, T. Kikuchi, M. Kurokawa, S. Moriya, S. Ogawa, H. Murakami, S. Shimoura, Y. Yanagisawa, T. Nakamura, Y. Watanabe, M. Ishihara, T. Teranishi, H. Okuno, R. Casten, *Phys. Lett. B* 346 (1995) 9.
- [236] A. Navin, D. W. Anthony, T. Aumann, T. Baumann, D. Bazin, Y. Blumenfeld, B. A. Brown, T. Glasmacher, P. G. Hansen, R. W. Ibbotson, P. A. Lofy, V. Maddalena, K. Miller, T. Nakamura, B. V. Pritychenko, B. M. Sherrill, E. Spears, M. Steiner, J. A. Tostevin, J. Yurkon, A. Wagner, *Phys. Rev. Lett.* 85 (2000) 266.
- [237] H. Iwasaki, T. Motobayashi, H. Akiyoshi, Y. Ando, N. Fukuda, H. Fujiwara, Z. F⁹¹l??p, K. Hahn, Y. Higurashi, M. Hirai, I. Hisanaga, N. Iwasa, T. Kijima, T. Minemura, T. Nakamura, M. Notani, S. Ozawa, H. Sakurai, S. Shimoura, S. Takeuchi, T. Teranishi, Y. Yanagisawa, M. Ishihara, *Phys. Lett. B* 481 (2000) 7.
- [238] S. Shimoura, A. Saito, T. Minemura, Y. U. Matsuyama, H. Baba, A. H, N. Aoi, T. Gomi, Y. Higurashi, K. Ieki, N. Imai, N. Iwasa, H. Iwasaki, S. Kanno, S. Kubono, M. Kunibu, S. Michimasa, T. Motobayashi, T. Nakamura, H. Sakurai, M. Serata, R. Takeshita, S. Takeuchi, T. Teranishi, K. Ue, K. Yamada, Y. Yanagisawa, M. Ishihara, Itagaki, *Phys. Lett. B* 560 (2003) 31.
- [239] B. Bastin, S. Grévy, D. Sohler, O. Sorlin, Z. Dombrádi, N. L. Achouri, J. C. Angélique, F. Azaiez, D. Baiborodin, R. Borcea, C. Bourgeois, A. Buta, A. Bürger, R. Chapman, J. C. Dalouzy, Z. Dlouhy, A. Drouard, Z. Elekes, S. Franchoo, S. Iacob, B. Laurent, M. Lazar, X. Liang, E. Liénard, J. Mrazek, L. Nalpas, F. Negoita, N. A. Orr, Y. Penionzhkevich, Z. Podolyák, F. Pougheon, P. Roussel-Chomaz, M. G. Saint-Laurent, M. Stanoiu, I. Stefan, F. Nowacki, A. Poves, *Phys. Rev. Lett.* 99 (2007) 022503.
- [240] S. Takeuchi, M. Matsushita, N. Aoi, P. Doornenbal, K. Li, T. Motobayashi, H. Scheit, D. Steppenbeck, H. Wang, H. Baba, D. Bazin, L. Cãceres, H. Crawford, P. Fallon, R. Gernhäuser, J. Gibelin, S. Go, S. Grévy, C. Hinke, C. R. Hoffman, R. Hughes, E. Ideguchi, D. Jenkins, N. Kobayashi, Y. Kondo, R. Krücken, T. Le Bleis, J. Lee, G. Lee, A. Matta, S. Michimasa, T. Nakamura, S. Ota, M. Petri, T. Sako, H. Sakurai, S. Shimoura, K. Steiger, K. Takahashi, M. Takechi, Y. Togano, R. Winkler, K. Yoneda, *Phys. Rev. Lett.* 109 (2012) 182501.
- [241] R. V. F. Janssens, B. Fornal, P. F. Mantica, B. A. Brown, R. Broda, P. Bhattacharyya, M. P. Carpenter, M. Cinausero, P. J. Daly, A. D. Davies, T. Glasmacher, Z. W. Grabowski, D. E. Groh, M. Honma, F. G. Kondev, W. Królas, T. Lauritsen, S. N. Liddick, S. Lunardi, N. Marginean, T. Mizusaki, D. J. Morrissey, A. C. Morton, W. F. Mueller, T. Otsuka, T. Pawlat, D. Seweryniak, H. Schatz, A. Stolz, S. L. Tabor, C. A. Ur, G. Viesti, I. Wiedenhöver, J. Wrzesiński, *Phys. Lett. B* 546 (2002) 55.

- [242] D.-C. Dinca, R. V. F. Janssens, A. Gade, D. Bazin, R. Broda, B. A. Brown, C. M. Campbell, M. P. Carpenter, P. Chowdhury, J. M. Cook, A. N. Deacon, B. Fornal, S. J. Freeman, T. Glasmacher, M. Honma, F. G. Kondev, J.-L. Lecouey, S. N. Liddick, P. F. Mantica, W. F. Mueller, H. Olliver, T. Otsuka, J. R. Terry, B. A. Tomlin, K. Yoneda, *Phys. Rev. C* 71 (2005) 041302.
- [243] A. Bürger, T. R. Saito, H. Grawe, H. Höbel, P. Reiter, G. J. M. Góska, H. J. Wollersheim, A. Al-Khatib, A. Banu, T. Beck, F. Becker, P. Bednarczyk, G. Benzoni, A. Bracco, S. Brambilla, P. Bringel, F. Camera, E. Clément, P. Doornenbal, H. Geissel, A. Görge, J. Grębosz, G. Hammond, M. Hellström, M. Honma, Kavatsyuk, O. Kavatsyuk, M. Kmiecik, I. Kojouharov, W. Korten, N. Kurz, M. R. Lozeva, A. Maj, S. Mandal, B. Million, S. Muralithar, A. Neußer, F. Nowacki, T. Otsuka, Z. Podolyák, N. Saito, A. K. Singh, H. Weick, C. Wheldon, O. Wieland, M. Winkler, R. Collaboration, *Phys. Lett. B* 622 (2005) 29.
- [244] E. Caurier, F. Nowacki, A. Poves, J. Retamosa, *Phys. Rev. C* 58 (1998) 2033.
- [245] E. Osnes, D. Strottman, *Phys. Rev. C* 45 (1992) 662.
- [246] T. Otsuka, T. Suzuki, R. Fujimoto, H. Grawe, Y. Akaishi, *Phys. Rev. Lett.* 95 (2005) 232502.
- [247] N. A. Smirnova, K. Heyde, B. Bally, F. Nowacki, K. Sieja, *Phys. Rev. C* 86 (2012) 034314.
- [248] S. R. Stroberg, H. Hergert, J. D. Holt, S. K. Bogner, A. Schwenk, *Phys. Rev. C* 93 (2016) 051301.
- [249] N. Tsunoda, T. Otsuka, N. Shimizu, M. Hjorth-Jensen, K. Takayanagi, T. Suzuki, *Phys. Rev. C* 95 (2017) 021304.
- [250] T. Otsuka, M. Honma, T. Mizusaki, N. Shimizu, Y. Utsuno, *Prog. Part. Nucl. Phys.* 47 (2001) 319.
- [251] N. Smirnova, B. Bally, K. Heyde, F. Nowacki, K. Sieja, *Phys. Lett. B* 686 (2010) 109.
- [252] I. Talmi, *Helv. Phys. Acta* 25 (1952) 185.
- [253] T. A. Brody, M. Moshinsky, *Tables of Transformation Brackets*, Monografias del Instituto de Fisica, Mexico, 1960.
- [254] M. Moshinsky, T. A. Brody, *Rev. Mex. Fís.* 9 (1960) 181.
- [255] L. Trlifaj, *Phys. Rev. C* 5 (1972) 1534.
- [256] B. Buck, A. C. Merchant, *Nucl. Phys. A* 600 (1996) 387.
- [257] G. P. Kamuntavičius, R. K. Kalinauskas, B. R. Barrett, S. Mickevičius, D. Germanas, *Nucl. Phys. A* 695 (1) (2001) 191.
- [258] P. Navrátil, B. R. Barrett, W. Glöckle, *Phys. Rev. C* 59 (1999) 611.
- [259] P. Navrátil, G. P. Kamuntavičius, B. R. Barrett, *Phys. Rev. C* 61 (2000) 044001.
- [260] A. Nogga, P. Navrátil, B. R. Barrett, J. P. Vary, *Phys. Rev. C* 73 (2006) 064002.
- [261] R. Roth, A. Calci, J. Langhammer, S. Binder, *Phys. Rev. C* 90 (2014) 024325.
- [262] T. Miyagi, S. R. Stroberg, P. Navrátil, K. Hebeler, J. D. Holt, *Phys. Rev. C* 105 (2022) 014302.
- [263] E. Epelbaum, *Prog. Part. Nucl. Phys.* 57 (2006) 654.

- [264] J. E. Lynn, I. Tews, J. Carlson, S. Gandolfi, A. Gezerlis, K. E. Schmidt, A. Schwenk, Phys. Rev. Lett. 116 (2016) 062501.
- [265] L. Huth, I. Tews, J. E. Lynn, A. Schwenk, Phys. Rev. C 96 (2017) 054003.
- [266] M. Piarulli, I. Tews, Frontiers in Physics 7 (2020) 245.